A SLIDING CORRELATOR CHANNEL SOUNDER FOR ULTRA-WIDEBAND MEASUREMENTS

A Thesis
Presented to
The Academic Faculty

by

Ryan J. Pirkl

In Partial Fulfillment
of the Requirements for the Degree
Master of Science in the
School of Electrical and Computer Engineering

Georgia Institute of Technology
August 2007

A SLIDING CORRELATOR CHANNEL SOUNDER FOR ULTRA-WIDEBAND MEASUREMENTS

Approved by:

Professor Gregory Durgin, Advisor
School of Electrical and Computer Engineering
Georgia Institute of Technology

Professor Mary Ann Ingram
School of Electrical and Computer Engineering
Georgia Institute of Technology

Professor Whit Smith
School of Electrical and Computer Engineering
Georgia Institute of Technology

Date Approved: 26 June 2007

To my family,

friends and relatives alike,

for their continued love and support.

It would have been a dreary journey without you.

PREFACE

The course of communication systems throughout the ages might be described as a quest for the elimination of space and time. Communications systems serve to unite people from far-reaching lands, bringing together ideas and perspectives to facilitate the flow of information and feed humanity's innate desire for connectedness. Toward this end, generations past have devised schemes for local, national, and global communication that ranged from hand-written letters to e-mail, from the telephone to the mobile phone, from the electric telegraph to the Internet. With each innovation, the advancement of faster communication across longer distances has steadily chipped away at the barriers of space and time that divided the world and its inhabitants.

Smoke Signals and Semaphores

It would take an especially devoted historian to point to a specific date along the course of mankind and declare it the beginning of long distance communication. Dismissing the more barbaric hooting, hollering, and general racket that our ancestors may have used to announce their location or communicate the presence of a threatening foe, we might safely conclude that the first "sophisticated" form of long-distance communication was smoke signals. Sentinels within the ancient civilizations of China, Egypt, and Greece are known to have used this signaling techniuqe to alert their camps of the enemy's approach [50].

As a more advanced means of communication, cunning inventors of the era proposed optical telegraph systems consisting of a network of semaphores stretching across the countryside [49]. Designs for the apparatus varied drastically, but the general blueprint involved a signaling device mounted atop a tower so that the semaphore could be viewed from great distances. The position and orientation of the semaphore were manipulated so as to convey a letter, word, or phrase to the vigilant watchman in the next tower [49]. With one eye glued to a telescope, the watchman would inform his coworker of the observed signal, and this gentleman would work the controls to set his station's semaphore to the appropriate position and orientation. In this manner, the information would trickle along from one tower to the next until it reached its destination.

All things considered, the semaphore network was capable of propagating complex messages with accuracy and celerity, making it an invaluable tool for connecting farreaching empires. One particular design that enjoyed great success was the optical telegraph of Claude Chappe, who is largely credited with inventing the semaphore system [50]. Using an arrangement of wooden arms on a rotating bar along with a corresponding code book, Chappe's telegraph as shown in Figure 1 was capable of sending an astounding 8,464 unique codes. First demonstrated in 1793, the capability for such fast long-distance communication was revolutionary and received strong support from the French government. Napoleon Bonaparte took particular interest in the telegraph system and called for an expansion of the network in 1804, extending the line all the way to Milan, Italy to facilate communication within the growing French Empire [49].

Electrifying Communication

Concurrent with the explosion of the semaphore, scientists were eagerly investigating the new field of electromagnetism, the discovery of which is credited to the Danish physicist Hans Christian Øersted in 1820. While preparing for a lecture, Øersted noticed that disconnecting and reconnecting a length of wire to a battery caused the deflection of a nearby compass needle. News of this simple observation spread quickly, and only weeks later French physicist André-Marie Ampere performed his own set of experiments that gave mathematical rigor to the new field of electromagnetism.

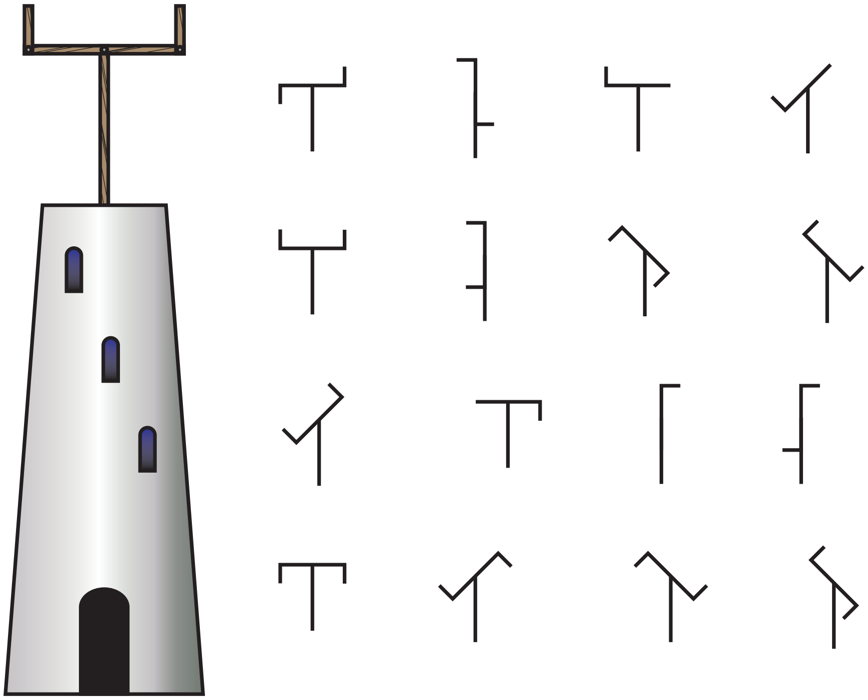

Figure 1: Claude Chappe's optical telegraph system consisted of a pivoting cross-beam with a pair of rotating arms mounted atop a tower. The arrangement of the beam and arms served to "transmit" information from one tower to the next. The delineations at right show but a handful of possible conformations for Chappe's semaphore.

Ampere's work was followed by that of English physicist Michael Faraday, who built what is considered the world's first transformer in 1831 and thereby discovered electromagnetic induction.

Increasing knowledge of electromagnetism paved the way for the next breakthrough in communication: the electric telegraph. While inventors had been tinkering with an electric telegraph for several years, it was not until 1837 that the device became practical. Depending on from which side of the pond you hail, credit for the first commercially viable electric telegraph goes to either the English team of William Cooke and Charles Wheatstone or the American artist-turned-inventor Samuel Morse [50]. All three men deserve recognition for their achievements, as they transformed the remainder of the 19th century into the age of the telegraph.

Electric telegraph lines sprung up quickly throughout the United States and Europe, and it was not long before attempts were made to span the Atlantic with a submarine cable. Initial efforts failed due to a combination of poor cable design and inssufficient knowledege of transmission lines. However, through the dogged determination of American businessman Cyrus Field and the technical expertise of Willoughby Smith and William Thomson (later Lord Kelvin), a functioning cable was finally laid beneath the ocean on July 27, 1886, connecting the Old World to the New and shrinking space and time [49].

Amidst this communications revolution, another breakthrough was to occur in the field of electromagnetism courtesy of the Scottish physicist James Clerk Maxwell. In 1864, Maxwell presented a set of twenty equations to Edinburgh's Royal Society that not only unified the field of electromagnetism but also predicted the existence of electromagnetic waves capable of propagating at the speed of light. Experimental proof, however, would have to wait two decades.

Going Wireless

While Maxwell's equations provided straightforward mathematical evidence that electromagnetic energy could propagate at the speed of light, experimental validation of such claims was a rather daunting task, as the fundamental components necessary for transmitting and receiving electromagnetic radiation simply did not exist. Heinrich Hertz, a German physicist working at Karlsruhe Polytechnic in Berlin, devoted himself to the challenge [50]. Over the course of three years, Hertz designed and constructed the first transmitter, receiver, and antennas, which are depicted in Figure 2. The transmitter was little more than a resonant circuit consisting of a Ruhmkorff coil for an inductor and a capacitively-loaded dipole antenna with a spark gap at its center [4]. Disharge of a battery into this circuit produced damped oscillations that caused the a spark gap to arc, thereby radiating electromagnetic energy. This device, appropriately called a *spark gap transmitter*, received great popularity during the early days of wireless. As both receiver and receive antenna, Hertz used a ring-shaped length of wire with a similar spark gap breaking the loop [4]. When electromagnetic waves of the appropriate polarity and wavelength were incident on the loop antenna, the spark-gap would produce a barely perceptible arc. In 1888, Hertz used his creations to determine the nodes and antinodes of a standing wave produced by the reflection of an electromagnetic wave off a large sheet of metal. Using this information and an estimation of his transmitter's oscillation frequency, Hertz calculated the propagation velocity of his electromagnetic waves, which, as expected, yielded a very close approximation to the speed of light.

Hertz's experiments provided irrefutable evidence of Maxwell's electromagnetic waves. Although Hertz himself foresaw little application for these waves, more prescient individuals like Guglielmo Marconi and William Crooke envisaged the future of communications. The telegraph and its complicated web of interconnected wires would become a thing of the past. No longer would information be bound to costly

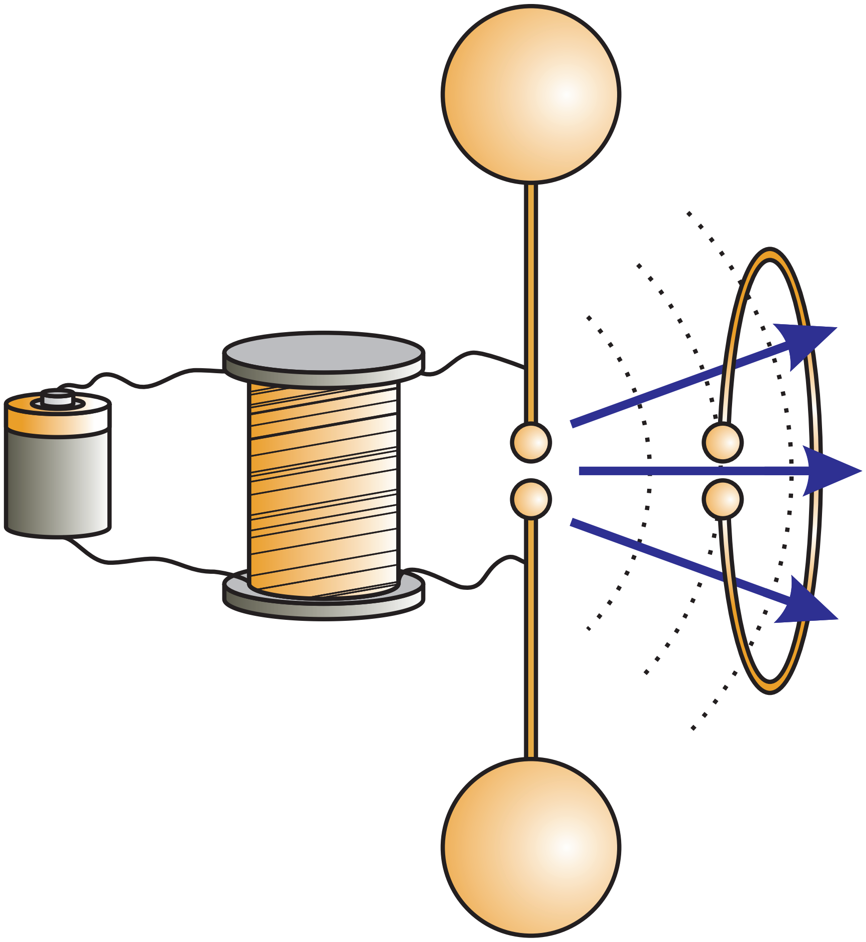

Figure 2: Hertz used a spark gap transmitter consisting of a battery, transformer, and capacitively-loaded dipole antenna to produce electromagnetic waves. The receiver was a loop of wire with a similar spark gap that would arc when electromagnetic waves propagated through it.

cables with definitive and finite paths. No longer would a stock report from New York have to be routed through telegraph stations in Nova Scotia and Ireland in order to reach London. Instead, data could be encoded onto propagating waves of electromagnetic energy, allowing direct communication between any two points on Earth. The wireless revolution had begun.

ACKNOWLEDGEMENTS

This work was sponsored in part by the National Science Foundation through a Graduate Research Fellowship. Thanks for the many boxes of cereal and pizza that your funds have afforded.

This research would have been impossible without the guidance and wisdom of my advisor, Dr. Gregory Durgin, who has kindly tolerated my innumerable questions, confusions, and general eccentricities over the years. My sincere thanks for all of the so-called "pep rallies".

A round of thanks also goes out to my committee members, Dr. Mary Ann Ingram and Dr. Whit Smith, for their patience in reading what has become a rather long-winded Master's Thesis. I bet you can't wait for the disertation!

A shout out to my homies in the Propagation Group for the many days of off-beat RF humor, stimulating conversation, and general coolness. A special note of gratitude to: Josh Griffin, who of has helped me tweak my mental model of the wireless channel and thereby born the brunt of my confusion; Albert Lu, for being the wise, helpful, and ever-inventive RF sage; Jet Zhu, for giving me his awesome desk by the window; and Chris Durkin, who over the past four years, has effectively served as my lab mentor by teaching me DSP (yeah, yeah, windows are good), the joys of test points (loopies!), LaTeX, C-to-Matlab wrappers, and anything else I could ever think to inquire of.

Special thanks to Brian Nakamura, who instructed me on the dos and don'ts of math notation.

Finally, a most humble word of thanks to my mother and father, Shirley and Dennis Pirkl, to whom I owe much if not everything that I have achieved.

TABLE OF CONTENTS

LIST OF TABLES

LIST OF FIGURES

SUMMARY

This body of work forms a detailed and comprehensive guide for those interested in performing broadband wireless channel measurements. Discussion addresses the theoretical and practical aspects of designing and implementing a sliding correlator channel sounder, as well as how such a system may be used to measure and model the ultra-wideband wireless channel. The specific contributions of this work are as follows:

- Developed a systematic methodology for designing optimal sliding correlator-based channel sounders.
- Constructed a UWB channel sounder based upon a 17-bit LFSR that attained 1.66 ns of temporal resolution and 34 dB of dynamic range.
- Performed an exemplary measurement campaign of the UWB channel from which UWB angular spreads and RMS delay spreads are reported.

The design procedure developed in Chapter 3 will allow researchers to build optimal channel sounders for investigating next-generation wireless channels. Chapter 4's discussion addresses the real-world challenges of constructing a high performance sliding correlator channel sounder. Finally, the measurement campaign discussed in Chapter 5 outlines a procedure for investigating the spatio-temporal characteristics of the wireless channel and provides some of the first examples of UWB angular spread measurements.

CHAPTER I

INTRODUCTION

- A gentleman navigating the urban jungle of New York City is baffled by the erratic behavior of his GPS receiver, which cannot seem to settle on his position.
- A business excutive aboard Japan's high-speed Shinkansen bullet train finds it impossible to place a call with her mobile phone.
- A sleep-deprived college student refueling at a local café with free wi-fi cannot get his laptop to find the network, even though neighboring patrons seem to be having no trouble.

Experiences like these might cause users to curse their wireless devices and yearn for the communication infrastructure of yesteryear when phones had wires and mail lacked any association with escargot. From mobile phones to wireless LANs, frustrations abound in this wireless world, leading to irritation and unfair expletive-filled accusations concerning the quality of a given manufacturer's product line. Unfortunately, the entity most liable for these fiery outburts rarely receives even a glower of disapproval. But what else would you expect for a culprit that is altogether imperceptible? Whereas the wireless device provides a conspicuous and tangible target for our animosity, the stealthy *wireless channel* is but ether to the senses.

1.1 Investigating the Wireless Channel

This body of work is, in many aspects, a guide for measurement-based investigations and characterization of the wireless channel. Thereby, this document instructs the reader on how to:

1. Design a wireless channel measurement system.
2. Construct the proposed instrument and measure the wireless channel.
3. Characterize the wireless channel with the measurement data.

The "guide" concept permeates this work, wherein discussion is intended to educate the reader on a process rather than merely report on recent progress in channel measurement techniques. With a bend toward education, a reocurring theme of this work will be "knowing what one is measuring". Whether implementing the measurement system or actually performing the measurements, it is crucial that one have a clear understanding of what one plans to measure. Hitting the highway without knowing where you're going can be fun and adventurous, but it can also get you stranded on a back road with neither gas nor directions. So, before we leap out of our seats and hit the road at full throttle, let us first prepare ourselves for the trip by learning what the wireless channel is all about.

1.2 The Amorphous and Intangible Wireless Channel

First and foremost, it should be made clear that the wireless channel isn't really out to get you. Just like snakes, spiders, and sharks, the wireless channel is not so much malevolent as it is misunderstood. Given the opportunity, the channel would undoubtedly oblige your every wireless whim. The unfortunate truth of the matter, however, is that, with its behavior bound by the laws of electromagnetism, the channel has very little say in how it propagates your wireless transmission. Therefore, it is the duty of the wireless engineer to work around the idiosyncracies of the channel or, better yet, to utilize these idiosyncracies to realize a more robust communication system boasting improved performance and reliabilty. This makes knowledge of the wireless channel an integral component of optimal system design and warrants a more in-depth discussion. However, rather than diving headfirst into the nature of this shapeless 5-dimensional construct, let us ease ourselves into the pool via an analogy to the more tangible field of acoustics.

Imagine yourself attending a service at Notre Dame de Paris, the breathtaking 13th century Gothic cathedral located in the heart of Paris. The cavernous nave, with its towering walls and arched ceilings, provides an excellent reverberation chamber for the massive pipe organ located at the West end of the cathedral. While ideal for resounding the organ's note and filling the church with its spiritual melodies, the cathedral's acoustics provide a poor venue for articulating a solemn sermon to the congregation. The innumerable echoes tend to blur words together and muddy the intelligibility of the sermon. An experienced pastor might compensate for the cathedral's poor acoustics by slowing his speech and deliberately enunciating each word. If this pastor were particularly gifted in his craft, he might even pause after an important point and allow the echoes to suspend his words, bouncing and fluttering about within the cathedral's hallowed walls.

The wireless channel is much like the acoustics of the cathedral, in that they are both by-products of the physics and geometry of the environment. The acoustics of a room do not directly describe how sound waves will bounce around, but they do indicate how long it will take for the echoes to fade away. Similarly, the wireless channel does not directly describe how a signal travels from transmitter to receiver, but it does provide an indication of how long it takes for its "echoes" to fade away. These electromagnetic "echoes" are the focus of much of the analysis into wireless channels.

1.3 Multipath

The phenomemenon of electromagnetic "echoes" is known as *multipath*, wherein each individual "echo" is a *multipath component*. Much like how acoustic echoes result from a sound wave bouncing off a surface, multipath arises due to electromagnetic

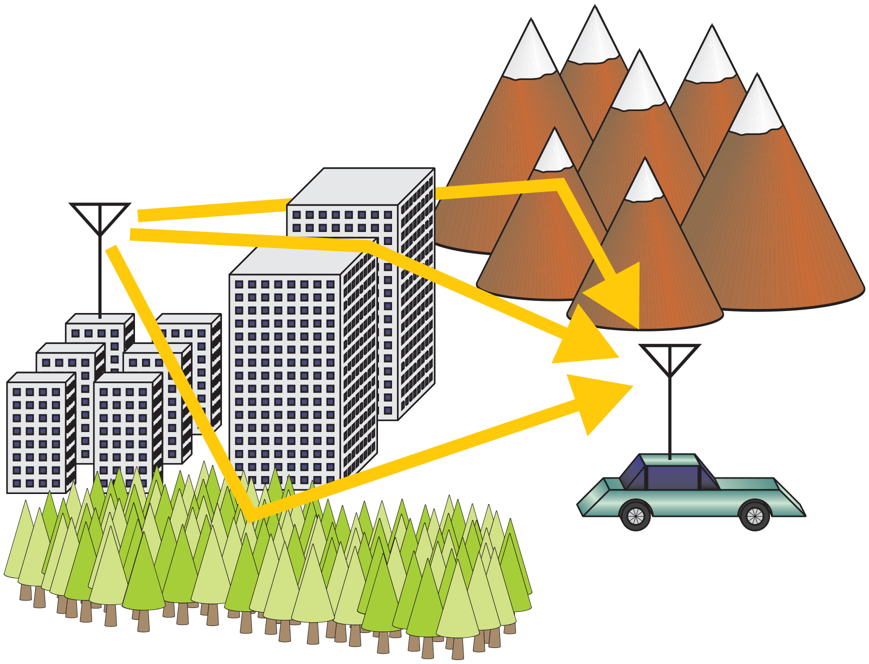

Figure 3: A scatterer may be a building edge, a mountainside, or a grove of trees. The presence of scatterers in an environments causes multipath, which defines the behavior of a wireless channel.

waves bouncing off *scatterers*. A scatterer is something that will redirect (or scatter) a portion of the power in an electromagnetic wave. Thus, a scatterer might be a large metal sheet, which would reflect an electromagnetic wave, or it might be a building edge, which would cause an electromagnetic wave to diffract. Figure 3 depicts how scatterers in an environment lead to multipath.

The existence of multipath due to scatterers within the environment is what turns a well-behaved wireless channel into a most unruly and seemingly unpredictable mess. Constructive and destructive interference of multipath components lead to signal peaks and nulls at various locations in space. This phenomenon, known as *small-scale fading*, can easily disrupt a perfectly functioning wireless communication system should an unwary user wander into a signal null. Further, the different delays in the time-of-arrival of multipath components cause a temporal "smearing" of the received signal, leading to intersymbol interference, symbol errors, and slower data rates. This is analagous to how the acoustics of the cathedral might blur words together, forcing the speaker to talk slower lest his speech be unintelligible.

Again, it is important to point out that the multipath-prone wireless channel is not inherently bad, just misunderstood. If one were to sit down with the wireless channel, examine it, have a proper tête-à-tête so to speak, one might realize that the supposedly troublesome multipath is really a life-saver for system engineers. Without those multipath components bouncing off walls and bending around corners, many wireless communication systems would fail as soon as the line-of-sight path between transmitter and receiver was obstructed. A thorough understanding of the wireless channel also provides information essential to the realization of equalizers and multiple antenna systemes, both of which yield improvements in signal-to-noise ratios (SNR) and thereby improvements in performance and reliability.

Unfortunately, despite its instrumental role and potential benefits, the wireless channel is easily the most overlooked and undercharacterized component of a wireless communication system. Whereas the transmitter and receiver may be designed, measured, and characterized for all possible operating conditions, the same cannot be said for the wireless channel. A by-product of the physics of the environment, the wireless channel cannot be tweaked or redesigned if it is “operating” poorly. Furthermore, the wireless channel embodies a 3-dimensional volume of space that may include everything from walls and furniture to pedestrians and motor vehicles. The environment may be static, as for a point-to-point microwave link, or it may be time-varying as for a busy office or factory. To further complicate matters, the transmitter and receiver might be in constant motion, soaring overhead aboard a commuter jet or zipping along the countryside on a high-speed bullet train. The variability of the wireless channel makes its characterization a most challenging endeavor.

1.4 Channel Modeling

Channel modeling (in concert with channel sounding) is the field concerned with characterizing the wireless channel so as to discern the severity of temporal "smearing" and spatial fading due to multipath. Channel modeling comes in two distinct flavors that, as their names suggest, employ strongly contrasting philosophies in their quest to describe the channel's behavior. *Deterministic channel modeling* is a theoretical approach that examines how electromagnetic energy propagates from transmitter to receiver within a specific environment. *Stochastic channel modeling*, on the other hand, is an experimental approach that attempts to produce a generalized description of the wireless channel for several environment archetypes.

1.4.1 Deterministic Channel Modeling

Deterministic channel modeling describes the wireless channel using the rules of electromagnetism and optics. This method requires a 2-D or 3-D model of the physical environment including knowledge of major scatterers and their material composition. After determining the location of the transmitter and receiver, techniques such as ray-tracing or finite-difference time-domain (FDTD) are used to analyze the exact pathways by which electromagnetic energy propagates from the transmitter to the receiver. Although computationally intensive, these techniques are capable of producing very accurate results, making deterministic channel modeling well-suited for investigating the underlying physics of radiopropagation.

1.4.2 Stochastic Channel Modeling

Stochastic channel modeling describes the wireless channel as a random process of space, time, and frequency. This method requires a large collection of measurement data to characterize the behavior of the random process using probability density functions and power spectral densities. Stochastic channel models do not produce an exact description of the wireless channel at a given location. Instead, they provide an *expectation* of the channel's behavior in a given environment. Thus, stochastic channel models are oftentimes employed to predict the reliability of a wireless communication system, making them invaluable tools from an industry standpoint.

1.5 Channel Sounding

Channel sounding is the experimental means of measuring a wireless channel, making it the inseparable spouse of channel modeling. Channel sounding measurements may be used to validate a deterministic channel model describing the physics of a site's radiopropagation, or they may be used to develop a stochastic channel model that describes the typical behavior of an environment's wireless channel. The duality of the frequency domain and time domain allows channel sounding to be performed in either. In the former, one measures the frequency response of the channel; in the latter, the impulse response.

1.5.1 Frequency Domain Channel Sounding

A wireless channel's frequency response is most commonly measured using a vector network analyzer (VNA). The VNA steps through a range of frequencies within the bandwidth of interest and, at each frequency, measures the channel's magnitude and phase response. Invoking our acoustic analogy, this would be like playing individual keys on the pipe organ and measuring how loud the note sounds at another point within the cathedral. While straightforward, there are several practical issues with frequency domain channel sounding. First, VNAs (like pipe organs) are quite expensive, ranging from tens to hundreds of thousands of dollars depending on their feature set and capabilities. Second, by measuring the channel at discrete frequencies using narrowband tones, VNAs are susceptible to measurement errors due to in-band interferents. Third, because modern VNAs are single-box solutions, the transmitter and receiver are co-located, which can be quite limiting if one wishes to measure indoor-to-outdoor or mobile-to-mobile wireless channels.

1.5.2 Time Domain Channel Sounding

A time domain channel measurement involves the transmission of a short impulse-like burst of electromagnetic energy. The brevity of the pulse allows one to measure the different arrival times of individual multipath components to determine the impulse response of the wireless channel. Once again invoking our acoustic analogy, this would be like measuring the delays between echoes caused by a single loud clap. This, too, is straighforward in concept, but a practical implementation is not so simple. The two most commonly cited concerns are in-band interference and the poor dynamic range of the measurements [35].

As opposed to transmitting a single impulse, it is possible to transmit a carefully crafted train of impulses in the form of a direct sequence spread spectrum (DSSS) signal. With appropriate processing of this impulse train at the receiver, one may determine the impulse response of the channel. Further, the unique characteristics of DSSS signals provide rejection of in-band interferents as well as improvements in dynamic range.

Spread spectrum channel sounding is ideal for narrowband channels, where the cost of capable analog-to-digital converters (ADC) are low. However, as bandwidth increases, so too must the sampling rate of the ADC. With performance and cost going hand-in-hand, this means that sounding an especially wideband channel puts an equally wide hole in one's pocket. And with the trend toward faster data rates and wider bandwidths as evidenced by the emergence of ultra-wideband communication, the cost of channel sounding is unlikely to fall off any time soon. The solution to this bandwidth inflation is *swept time-delay channel sounding*, which which pairs the DSSS signals of spread spectrum channel sounding with a sliding correlator receiver to compress the large bandwidth of the measured impulse reponse [35].

1.5.3 Swept Time-Delay Channel Sounding

The bandwidth compression of swept-time delay channel sounding results from the temporal dilation of the channel impulse response and allows for more economical means of recording and processing channel measurements. Temporal dilation is typically realized via a sliding correlator receiver, which approximates a true correlator receiver by multiplying the received signal with a "slow" copy of the transmitted signal and then filtering the product. The *sliding correlator channel sounder* is the most popular implementation of swept time-delay channel sounding and has been used extensively for wideband channel measurements [6, 36, 33]. The sliding correlator channel sounder is also a natural solution for sounding the massive spectrum occupied by ultra-wideband (UWB) communication systems [51, 11].

1.6 Ultra-Wideband Communication

While many might consider UWB communication to be a modern innovation, its origins stretch back to the dawn of wireless with the spark gap transmitter of Heinrich Hertz. As defined by the Federal Communications Commission (FCC) in 2002, the term "UWB" applies to wireless communication with a minimum bandwidth of 500 MHz or a bandwidth-to-carrier ratio of 1/5 [48]. The latter would have easily been achieved by Hertz's spark gap transmitter, which came to be viewed as a notoriously dirty radiator whose impulses consumed enormous chunks of bandwidth. The spectral inefficiency of the spark gap transmitter led to its banishment as narrowband communication became vogue. A century later, however, the tides turned, and wireless engineers begin to realize the benefits of communication schemes that employed bandwidths much greater than their information rates [48]. While spark gap transmitters remain outlawed, other more controlled means of UWB communication are acceptable provided that their transmission spectrum meets the FCC's UWB emmissions mask shown in Figure 4.

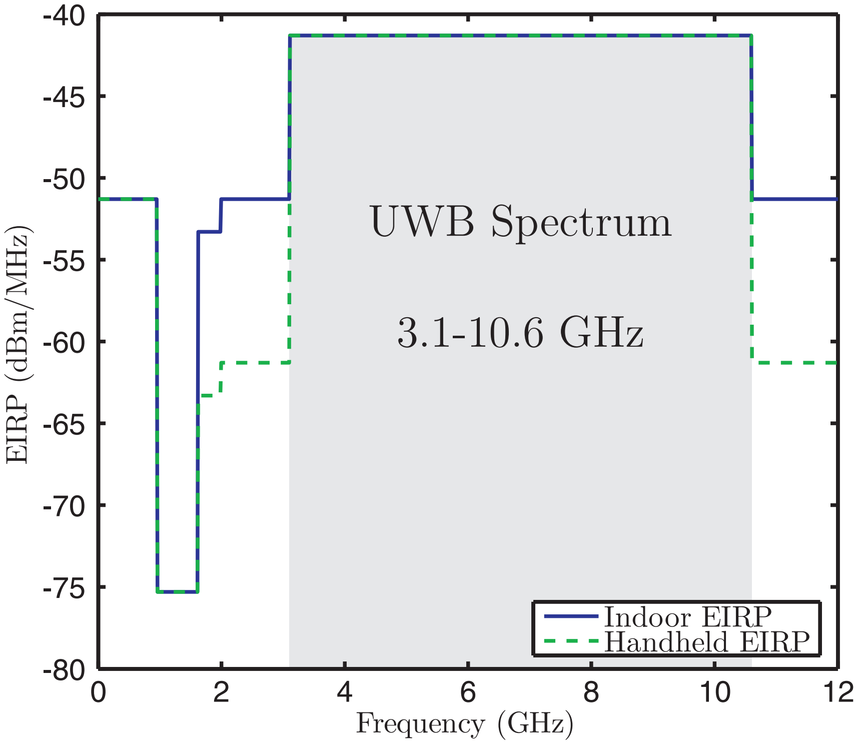

Figure 4: The FCC's emissions mask for indoor and handheld UWB communication. Maximum emission levels are specified in terms of their effective isotropically radiated power (EIRP) with units of dBm per MHz.

1.6.1 Background

The FCC regulations for UWB define two distinct operating bands: the upper band ranging from 3.1 to 10.6 GHz and the lower band for transmissions below 960 MHz. Each band has its own set of rules and regulations that vary based on both application and environment. For the purposes of this work, discussion shall be limited to indoor communication in the upper UWB band. Examining Figure 4, it may be seen that the FCC specifies a maximum power density for UWB transmissions in terms of *effective isotropically radiated power* (EIRP) per MHz. EIRP is the power at the input of the antenna plus the maximum gain of the antenna relative to an isotropic radiator. For the upper UWB band, the maximum EIRP for indoor communication is -41.3 dBm/MHz. Therefore, if a transmission were to utilize the entire 7,500 MHz of available bandwidth, the maximum total EIRP would be -2.55 dBm

The incredibly large bandwidth and low power levels of UWB make it a unique and compelling technology. By spreading the energy across several Gigahertz of bandwidth, UWB signals have an extremely low probability-of-intercept (POI), appearing as added noise to even the most wideband of continuous-wave-based receivers. This low POI allows UWB systems to freely utilize portions of the spectrum that are typically restricted to paying customers. UWB's ability to operate amidst existing wireless systems opens up a plethora of applications where short-range high-speed wireless communication is key.

1.6.2 Applications

UWB is particularly well-suited for fast data rates in small local areas. Thus, the most commonly touted applications are piconets and body-area networks. Advocates envision a truly wireless workstation where computer peripherals, monitors, personal data assistants, and mobile phones all communicate via UWB. In hospitals, where patients normally find themselves tethered to medical equipment, doctors and nurses might use UWB technology to monitor critical life signs with wireless probes. Sensor networks offer yet another interesting application of UWB [48]. Sensor nodes must be extremely compact and power efficient. Thus, the low hardware complexity of impulse-based UWB makes it a very compelling option. Furthermore, the UWB waveform itself may be used for sensing applications [48]. Other interesting applications of UWB include ranging, position location, asset tracking, and both ground-penetrating and through-wall radar [37].

1.6.3 Issues

Amidst the hype surrounding UWB, plenty of problems remain. The dissolution of the IEEE's UWB task group (802.15.31) was a particularly poignant blow to the technology, but UWB development has continued undaunted. Industry leaders united beneath non-profit umbrella organizations such as the WiMedia Alliance and the UWB Forum with the goal of forging technology standards to ensure that UWB becomes a reality. With its many compelling applications and the support of major players in the wireless and electronics industry, the future of UWB appears secure.

Even with the industry's financial backing, UWB has a ways to go before it escapes the corporate R&D labs and finally reaches the homes and offices of consumers. For decades, designers have known how to produce inexpensive UWB transmitters, but the quest for an equally cheap yet capable receiver continues. While UWB contributes very little interference to nearby narrowband systems, the converse is far from true. The high power density of narrowband signals can easily saturate the wideband low-noise amplifier (LNA) at the UWB receiver. Notch filters may be used to attenuate particularly powerful signals with little degradation to the UWB signal, but an assortment of high-Q notch filters at the receiver will only add to its cost [48].

The short duration of UWB signals, while a boon for its enormous bandwidth, also makes for a timing nightmare. Syncing of the transmitter and receiver is crucial for matched filtering and sampling of the received signal [37]. For pulse-position modulation (PPM) schemes, timing is all the more critical as information is encoded in the relative delay of the transmitted pulse.

Another major issue is the antenna, which must have a constant radiation pattern and phase center across the entire bandwidth of the signal [37]. If either requirement is not met, the transmitted or received pulse will vary as a function of angle-of-departure or angle-of-arrival, complicating any efforts toward implementing a matched filter. One proposed work-around uses the equivalent of differential phase shift keying (DPSK) to self-correlate the first received reference pulse with the subsequent data pulse [48].

The self-correlating receiver also resolves concerns over the variability of the wireless channel. With narrowband wireless links, it is common practice to assume the diffraction and attenuation of scatterers within the wireless channel are constant as a function of frequency. Although an acceptable approximation for small bandwidths, it is unclear if the same is true for the large bandwidths of UWB [32]. If material properties change significantly with bandwidth, then each UWB multipath component will be distorted uniquely. Such uncertainty over the fundamental physics of UWB radiopropagation only emphasizes the need for more UWB channel measurements.

1.7 A UWB Channel Sounder

The remainder of the work herein addresses the design and implementation of a sliding correlator channel sounder capable of measuring the large bandwidths of UWB channels. We shall be primarily concerned with how the channel sounder might be used for stochastic channel modeling, which shall be addressed in detail in Chapter 2, but this in no way implies a limitation on the system's possible applications. Chapter 3 will examine the theoretical operation of a sliding correlator channel sounder followed by an overview of the realized system in Chapter 4. Discussion shall address the design process, component selection, construction, and capabilities of the UWB channel sounder. Chapter 5 describes an exemplary measurement campaign of the UWB channel using the constructed channel sounder. Measurements are provided as are calculations of various channel parameters discussed in Chapter 2. Concluding remarks and possible directions for future work are contained within Chapter 6.

CHAPTER II

STOCHASTIC CHANNEL MODELING

Measurements carry little meaning if one lacks an understanding of the phenomenon being measured. Thus, the motivation behind this chapter is the formation of a solid foundation of knowledge concerning the stochastic wireless channel. Depth of analysis, as opposed to breadth of topics, was selected as the mode of presentation for the underlying theory and principles. Thereby, it is hoped that the unfamiliar reader might come away with an understanding of the material herein, as opposed to a more superficial acquaintance with the topics at hand. Finally, it is duly noted that content in this chapter draws mainly from [14].

2.1 Wireless Channel Representation

Following circuit theory for a linear, time-invariant (LTI) filter, an input signal $x(t)$ passes through a filter with an impulse response $H(\tau)$, resulting in the output signal $y(t)$ as depicted in Figure 5. Accordingly, the output signal $y(t)$ can be expressed as the convolution of the input signal $x(t)$ with $H(\tau)$ as given by

$$y(t) = x(t) \otimes H(\tau)|_{\tau=t} \tag{1}$$

where $\otimes$ represents the convolution operator as defined by (2).

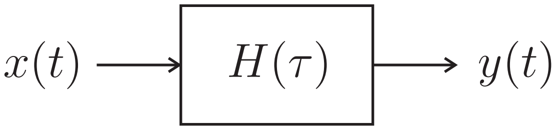

Figure 5: Diagram of a linear time-invariant filter.

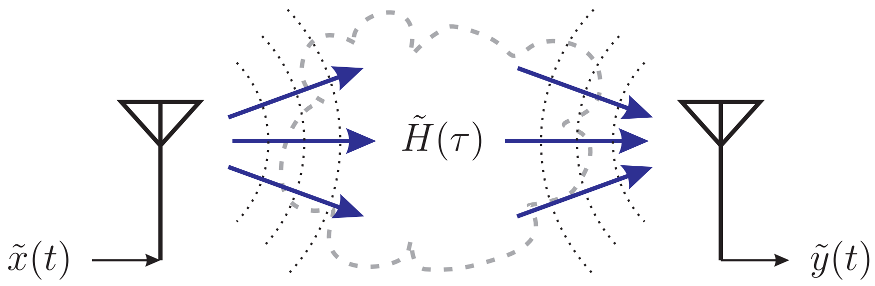

Figure 6: Diagram of a fixed linear time-invariant wireless channel.

$$a(t) \otimes b(t) = \int_{-\infty}^{\infty} a(\zeta)b(t-\zeta)d\zeta \tag{2}$$

Analogously, one may consider the situation in Figure 6 in which the complex baseband signal $\tilde{x}(t)$ is transmitted through a fixed LTI wireless channel with an impulse response $\tilde{H}(\tau)$, resulting in the received signal $\tilde{y}(t)$ as given by

$$\tilde{y}(t) = \frac{1}{2}\tilde{x}(t) \otimes \tilde{H}(\tau)\Big|_{\tau=t} \tag{3}$$

Note that the transmitted signal $\tilde{x}(t)$, received signal $\tilde{y}(t)$, and channel impulse response $\tilde{H}(\tau)$ are complex baseband representations of the wireless link. The factor of 1/2 arises due to the convolution of these complex equivalent signals.

Generalizing this expression, one may consider a space- and time-varying wireless channel impulse response $\tilde{H}(\tau;\vec{r},t)$, where $\vec{r}$ is the position of the receiver assuming a fixed transmitter, and t indicates the time-varying nature of the channel due to moving scatterers. For this case, the received signal $\tilde{y}(\vec{r},t)$ is expressed as

$$\tilde{y}(\vec{r},t) = \int_{-\infty}^{\infty} \tilde{x}(t-\tau)\tilde{H}(\tau;\vec{r},t)d\tau \tag{4}$$

This representation indicates the spatial and temporal dependence of the received signal resulting from the space, time, and frequency dependence of the wireless channel.

2.2 Wireless Channel Transfer Function

In the circuit example, the LTI filter was described by its impulse response, $H(\tau)$, which is the Fourier transform of the filter's complex frequency response $\tilde{h}(f)$ as given by

$$H(\tau) = \int_{-\infty}^{\infty} \tilde{h}(f) e^{-j2\pi f \tau} df \tag{5}$$

Similarly, the generalized channel impulse response (CIR) for a mobile and time-varying wireless channel is the Fourier transform of the wireless channel with respect to frequency.

$$\tilde{H}(\tau; \vec{r}, t) = \int_{-\infty}^{\infty} \tilde{h}(f, \vec{r}, t) e^{-j2\pi f \tau} df \tag{6}$$

Therefore, the complex baseband wireless channel is given by $\tilde{h}(f, \vec{r}, t)$, indicating the frequency (f), space ($\vec{r}$), and time (t) dependence of the wireless channel. From these dependencies come the following Fourier transform pairs:

- frequency (f) $\Longleftrightarrow$ delay (τ)
- space ($\vec{r}$) $\Longleftrightarrow$ wavevector ($\vec{k}$)
- time (t) $\Longleftrightarrow$ Doppler (ω)

Thereby, the complete transfer function of the wireless channel $\tilde{h}(f, \vec{r}, t)$ is given by $\tilde{H}(\tau, \vec{k}, \omega)$.

2.3 Stochastic Wireless Channel

The impulse response of the basic filter described in Section 2.1 is constant at any point in space and time. Therefore, as seen in (1), when and where one might use the filter has no impact on how it affects $x(t)$. In contrast, the wireless channel in (4) is space and time dependent, requiring complete space-time knowledge of the channel to accurately model how it will affect a transmitted signal. This perspective embodies the deterministic approach to channel modeling, in which an exact description of the wireless channel is calculated from a physical description of the enviroment. As was discussed in Section 1.4.1, while it is possible to estimate a deterministic channel model using ray tracing or FDTD, the task is time-consuming and computationally intensive. Therefore, a stochastic model is oftentimes employed whereby the wireless channel is represented by a space, time, and frequency dependent stochastic process. This approach is more concerned with characterizing the channel's overall behavior in an area than determining the exact CIR at a specific point in space and time.

2.3.1 Stochastic Processes

To understand stochastic channel modeling, one must first have a basic understanding of stochastic processes. Thus, the following sections provide a brief overview of their fundamental properties.

2.3.2 Probability Density Function

A *probability density function*, $f_X(x,t)$, describes the likelihood of a random variable, x, taking on a value or range of values at time t. As the name implies, $f_X(x,t)$ is a density, whereby obtaining an actual probability of an outcome requires integration of the probability density function (PDF). Figure 7 shows an example of the Rayliegh PDF, which is oftentimes used to describe the envelope of a received signal in a multipath-rich wireless channel.

2.3.3 Mean

For a complex time-dependent stochastic process, $\tilde{x}(t)$, with a corresponding amplitude PDF, $f_X(x,t)$, the mean, $\overline{\tilde{x}(t)}$, is the expected value of the process at a given time t. The mean is defined as the first moment of $\tilde{x}(t)$ as given by

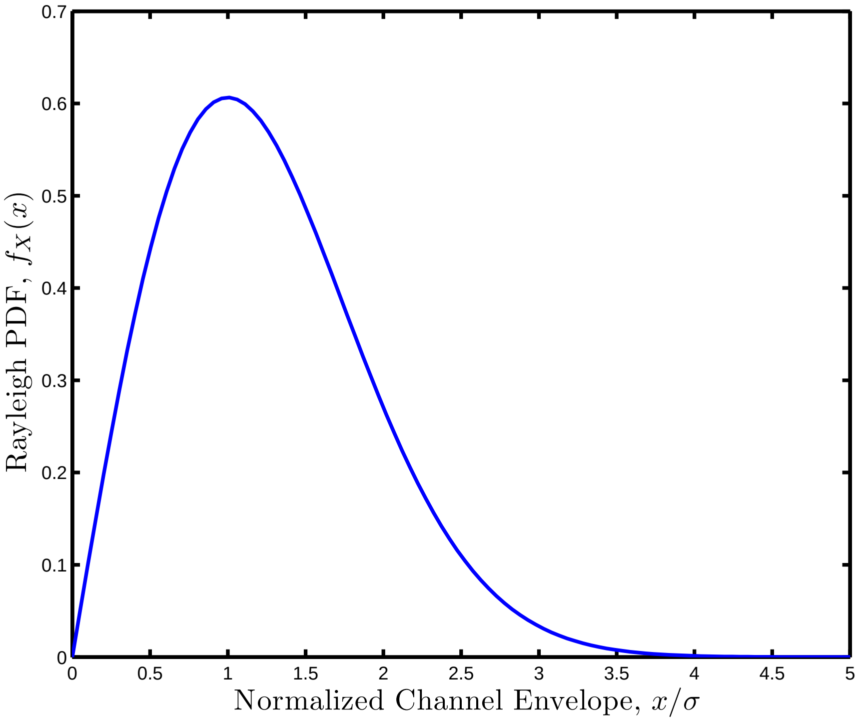

Figure 7: The envelope of wireless channel may oftentimes be described by a Rayleigh probability density function.

$$\overline{\tilde{x}(t)} = \mathrm{E}\left[\tilde{x}(t)\right] \tag{7}$$

where $\mathrm{E}\left[(\cdot)\right]$ donotes the expectation operator as defined in (8).

$$\mathrm{E}\left[(\cdot)\right] = \int_{-\infty}^{\infty} (\cdot) f_X(x,t)dx \tag{8}$$

2.3.4 Autocorrelation

The autocorrelation function, $C_{\tilde{x}}(t_1, t_2)$, is a measure of the correlation of a single realization of the random process $\tilde{x}(t)$ at times t_1 and t_2. That is, it compares how similar the random process $\tilde{x}(t)$ behaves for two time delays. The autocorrelation function is given by

$$C_{\tilde{x}}(t_1, t_2) = \mathrm{E}\left[\tilde{x}(t_1)\tilde{x}(t_2)^*\right] \tag{9}$$

where $(\cdot)^*$ denotes the complex conjugate of $(\cdot)$.

2.3.5 Ergodicity

Given a stochastic process, $\tilde{x}(t)$, that is a function of time, one may determine the temporal average of the process, denoted as $\langle \tilde{x}(t) \rangle_t$.

$$\langle \tilde{x}(t) \rangle_t = \lim_{T \to \infty} \frac{1}{T} \int_{-T/2}^{T/2} \tilde{x}(t) dt \tag{10}$$

Let us now assume that $\tilde{x}(t)$ is *ergodic* with respect to time. This means that the expectation of the process, $\mathrm{E}\left[\tilde{x}(t)\right]$, is equal to its time-averaged value, $\langle \tilde{x}(t) \rangle_t$.

$$\text{Time Ergodic: } \mathrm{E}\left[\tilde{x}(t)\right] = \langle \tilde{x}(t) \rangle_t \tag{11}$$

Thus, the expectation of the random process may be found by averaging a realization of that process for a period T. Note that ergodicity is not solely a time domain property; a process may also be ergodic with respect to frequency or space. For a process that is ergodic with respect to frequency, we have

$$\text{Frequency Ergodic: } \mathrm{E}\left[\tilde{x}(f)\right] = \langle \tilde{x}(f) \rangle_f \tag{12}$$

where $\langle \tilde{x}(f) \rangle_f$ is the frequency average of $\tilde{x}(f)$ given by

$$\langle \tilde{x}(f) \rangle_f = \lim_{B \to \infty} \frac{1}{B} \int_{-B/2}^{B/2} \tilde{x}(f) df \tag{13}$$

and B is the bandwidth over which the process is averaged. Similarly, for a process that is ergodic with respect to space, we have

$$\text{Space Ergodic: } \mathrm{E}\left[\tilde{x}(\vec{r})\right] = \langle \tilde{x}(\vec{r}) \rangle_{\vec{r}} \tag{14}$$

where $\langle \tilde{x}(\vec{r}) \rangle_{\vec{r}}$ is the spatial average of $\tilde{x}(\vec{r})$ given by

$$\langle \tilde{x}(\vec{r}) \rangle_{\vec{r}} = \lim_{L\to\infty} \frac{1}{L^3} \int\limits_{-L/2}^{L/2} \tilde{x}(\vec{r}) d\vec{r} \tag{15}$$

and L is the length of one side of a cubic volume over which the process is averaged.

2.3.6 Wide-Sense Stationarity

The analysis of a given stochastic process is simplified if it exhibits wide-sense stationarity. Wide-sense stationary processes are a subset of strict-sense stationary random processes. For a random process $\tilde{x}(t)$ to be strict-sense stationary with respect to time, all statistics of the random process must be independent of absolute time. Strict-sense stationarity is difficult to prove for a real process. The alternative of wide-sense stationarity is much easier to prove, as it requires only the first- and second-order statistics to be independent of absolute time. Thus, the criteria for a wide-sense stationary (WSS) process with respect to time are:

- $\overline{\tilde{x}(t)} = \overline{\tilde{x}}$
- $C_{\tilde{x}}(t_1, t_2) = C_{\tilde{x}}(\Delta t)$

The first requirement is that the mean of the process be constant regardless of when the process is realized. The second requirement is that the autocorrelation be only a function of the difference betwen the two time instances, $\Delta t = t_1 - t_2$.

2.3.7 Power Spectral Density

For a WSS process, one may invoke the Wiener-Khintchine theorem, which defines the power spectral density (PSD) of a process as the Fourier transform pair of its autocorrelation [21]. The power spectral density, $S_{\tilde{x}}(\omega)$, is thus

$$S_{\tilde{x}}(\omega) = \int\limits_{-\infty}^{\infty} C_{\tilde{x}}(\Delta t) e^{-j2\pi\omega\Delta t} d\Delta t \tag{16}$$

As its name implies, a PSD is a power density with density units following that of the Fourier transform of the dependent variable. That is, for an autocorrelation of the form, $C_{\tilde{x}}(\Delta t)$, where Δt is in seconds, the power spectral density will have units of Watts per radian per second.

2.4 Stochastic Local Area Channels

Having established a foundation for stochastic processes, it is now possible to define and examine the *stochastic local area channel.* A stochastic local area channel (SLAC) is a summation of the voltages arrising from all homogeneous plane waves incident upon the receiver antenna [14]. Thus, the SLAC model describes N homogeneous planes waves, where the i^{th} plane wave has a delay τ_i, wavevector $\vec{k_i}$, induced voltage V_i, and a random phase Φ_i whose PDF is a uniform distribution between 0 and 2π. Additionally, values of $\vec{k_i}$ are restricted to those that give $\vec{k_i} \cdot \vec{k_i} = k_i^2$ where $k_i = \frac{2\pi}{\lambda_i}$ and λ_i is the free space wavelength.

$$\tilde{h}(f, \vec{r}) = \sum_{i=1}^{N} V_i \exp\left(j\left[\Phi_i - \vec{k_i} \cdot \vec{r} - 2\pi f \tau_i\right]\right) \tag{17}$$

It is important to note that in (17), f and $\vec{r}$ have different definitions than those for f and $\vec{r}$ in (6) for the general wireless channel. Here, f is the frequency displacement from the carrier frequency of the transmitted signal. The parameter $\vec{r}$ is the spatial displacement describing the receiver's location relative to a point defined as the center of the *local area.* The size of this so-called local area is bound by a circular region with diameter L_A such that

$$L_A < \frac{c}{B} \tag{18}$$

where B is the bandwidth of the transmitted signal [14]. Additionally, the SLAC model is only valid for regions located far from scatterers where the power contributed by inhomogeneous plane waves is neglible. Figure 8 shows a graphical representation

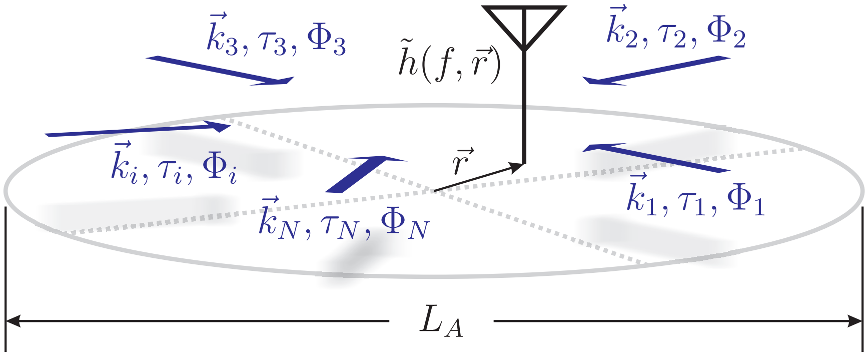

Figure 8: Depiction of the stochastic local area channel, which describes the wireless channel within a local area L_A as a summation of homogeneous plane waves with random phases.

of the SLAC model.

2.4.1 Motivating the SLAC Model

The wireless channel described in Section 2.1 may be thought of as a space- and time-varying filter that describes the CIR between a fixed transmiter and a mobile receiver for *any* point in space and time. The wireless channel therefore acts as a transfer function for calculating the received signal $\tilde{y}(t)$ given an arbitrary transmitted signal $\tilde{x}(t)$. In contrast, the SLAC model describes the voltage arrising from plane waves incident upon the receiver antenna within a bounded region defined as the local area. Therefore, the SLAC model implies the presence of a specific transmitted signal that gives rise to N propagating homogeneous plane waves in the local area and thereby a physical voltage at the receiver antenna. Whereas the wireless channel description is a somewhat amorphous function of frequency, space, and time, the SLAC description provides a structured physical representation of the wireless propagation in a region using a Maxwellian basis.

The value of the SLAC model extends beyond being an intuitively satisfying physical description of the wireless channel in a local area. By reminding ourselves that the enigmatic wireless channel spanning the entire region is but the aggregate of strictly defined electromagnetic propagation mechanisms in smaller local area, we are able to utilize the underlying physics of the problem to prove several powerful theorems that greatly simplify the measurement component of stochastic channel modeling.

As a final point for the sake of clarity, distinctions should be made between the terms *wireless channel*, *local area channel*, and *stochastic local area channel*. The *wireless channel* is an unbounded representation of the stochastic process describing the frequency, space, and time dependence of a wireless transmission. The *local area channel* is a spatially bounded representation of the wireless channel that attributes received power to the summation of voltages contributed by homogeneous plane waves. The local area channel is restricted to regions far from scatterers, but beyond this, the exact size of the local area is somewhat arbitrary. Thus, the *stochastic local area channel* is a modification to the local area channel whereby the size of the local area is strictly defined according to the bandwidth of the transmitted signal.

2.4.2 Wide-Sense Stationary SLAC

For a SLAC, $\tilde{h}(f, \vec{r})$, the process may be wide-sense stationary with respect to frequency f, space $\vec{r}$, or both. Recalling the criteria for a WSS process, a SLAC that is WSS with respect to frequency will have a mean independent of frequency and an autocorrelation that depends only on the difference between frequencies.

- $\overline{\tilde{h}(f)} = \overline{\tilde{h}}$
- $C_{\tilde{h}}(f_1, f_2) = C_{\tilde{h}}(\Delta f)$ where $\Delta f = f_2 - f_1$

Similarly, a SLAC that is WSS with respect to space will have a mean independent of space and an autocorrelation that depends only on the distance between points in space.

- $\overline{\tilde{h}(\vec{r})} = \overline{\tilde{h}}$
- $C_{\tilde{h}}(\vec{r_1}, \vec{r_2}) = C_{\tilde{h}}(\Delta\vec{r})$ where $\Delta\vec{r} = \vec{r}_2 - \vec{r}_2$

It is a challenging matter to analyze a SLAC that is not wide-sense stationary, and furthermore, nearly all SLACs exhibit this property. Therefore, the assumption of wide-sense stationarity is fairly common and will be assumed for the SLAC model.

2.4.3 Uncorrelated Complex Phases

The uniformly distributed phases, Φ_i, of the homogeneous plane wave are the random variables leading to the stochastic nature of the SLAC model. If the complex phases, $e^{j\Phi_i}$, are uncorrelated, then the expectation of the product of any two unique complex phases will be zero.

$$E\left[e^{j(\Phi_l - \Phi_m)}\right] = 0 \tag{19}$$

Justification for uncorrelates complex phases lies in the unique paths of each multipath component. Considering that each multipath component arises from different scatterers and travels different distances, it is a safe assumption that the individual complex phases will be uncorrelated when they arrive at the receiver antenna.

2.4.4 Heterogeneous Scattering

In addition to the random phase, Φ_i, each homogenous plane wave is described by a delay, τ_i, and a wavevector, $\vec{k}_i$. Heterogeneous scattering describes the scenario wherein every delay and wavevector is unique. Therefore:

- $\tau_l \neq \tau_m$
- $\vec{k}_l \neq \vec{k}_m$

Give the richness and physical complexity of a radiopropagation environment, it becomes highly improbable for two waves to arrive at exactly the same time or from exactly the same direction. Thus, the condition of heterogeneous scattering is a common assumption for the SLAC model.

2.4.5 Power Ergodicity

For the case of a WSS SLAC with uncorrelated phases and heterogeneous scattering, it can be shown that the SLAC is power ergodic with respect to both space and frequency [14]. This leads to the following relationship:

$$P_R = \left\langle \left| \tilde{h}(f) \right|^2 \right\rangle_f = \left\langle \left| \tilde{h}(\vec{r}) \right|^2 \right\rangle_{\vec{r}} \tag{20}$$

where P_R is the average power in the local area. In words, (20) means that, for a WSS SLAC with uncorrelated phases and heterogeneous scattering, the average received power in a local area may be found by either frequency-averaging or space-averaging the magnitude-squared channel. This is a powerful and practical relationship, as it allows one to determine the average power via a stationary broadband wireless link or a mobile narrow band wireles link [14].

2.5 Wireless Channel Power Spectral Densities

If the wireless channel is a wide-sense stationary process, then one may define PSDs from the autocorrelations of channel dependencies according to (16). Therefore, we first define the autocorrelations for frequency, time, and space as given by (21), (22), and (23), respectively.

$$C_{\tilde{h}}(\Delta f) = \int_{-\infty}^{\infty} \tilde{h}(f)^* \tilde{h}(f + \Delta f) df \tag{21}$$

$$C_{\tilde{h}}(\Delta t) = \int_{-\infty}^{\infty} \tilde{h}(t)^* \tilde{h}(t + \Delta t) dt \tag{22}$$

$$C_{\tilde{h}}(\Delta r) = \int_{-\infty}^{\infty} \tilde{h}(r)^* \tilde{h}(r + \Delta r) dr \tag{23}$$

We may then define the corresponding PSDs, which for the frequency, time, and space autocorrelations, are the delay, Doppler, and wavenumber spectrums respectively.

2.5.1 Delay Spectrum

The delay spectrum is the power spectral density of the channel as a function of delay. It is defined as the Fourier transform of a channel's autocorrelation with respect to frequency and has the units of Watts/second.

$$S_{\tilde{h}}(\tau) = \int_{-\infty}^{\infty} C_{\tilde{h}}(\Delta f) e^{j2\pi\tau\Delta f} d\Delta f \tag{24}$$

The delay spectrum represents an expectation of the power density at the receiver for a given delay assuming the channel was excited by an impulse. The delay spectrum for wireless channels is commonly described by an exponential function as shown in Figure 9. As one might expect for an impulse excitation, larger delays lead to smaller power densities as multipath components become further attenuated due to added scattering mechanisms and increased path lengths. Also, note that for delays less than zero, the power density is zero. This is the expected result of a causal channel.

The delay spectrum is described by its width and centroid, which can be calculated from the n^{th} moment of the delay spectrum as given by

$$\overline{\tau^n} = \frac{\int_{-\infty}^{\infty} \tau^n S_{\tilde{h}}(\tau) d\tau}{\int_{-\infty}^{\infty} S_{\tilde{h}}(\tau) d\tau} \tag{25}$$

The first moment, $\overline{\tau}$, represents the centroid of the delay spectrum, and thereby, its mean delay. In physical terms, the mean delay indicates the time required for a significant percentage of the multipath components to propagate from the transmitter to the receiver. The width of the delay spectrum is characterized by the root-mean square (RMS) *delay spread* of the PSD and can be calculated according to

$$\sigma_\tau = \sqrt{\overline{\tau^2} - (\overline{\tau})^2} \tag{26}$$

In physical terms, the RMS delay spread indicates the extent to which a transmitted

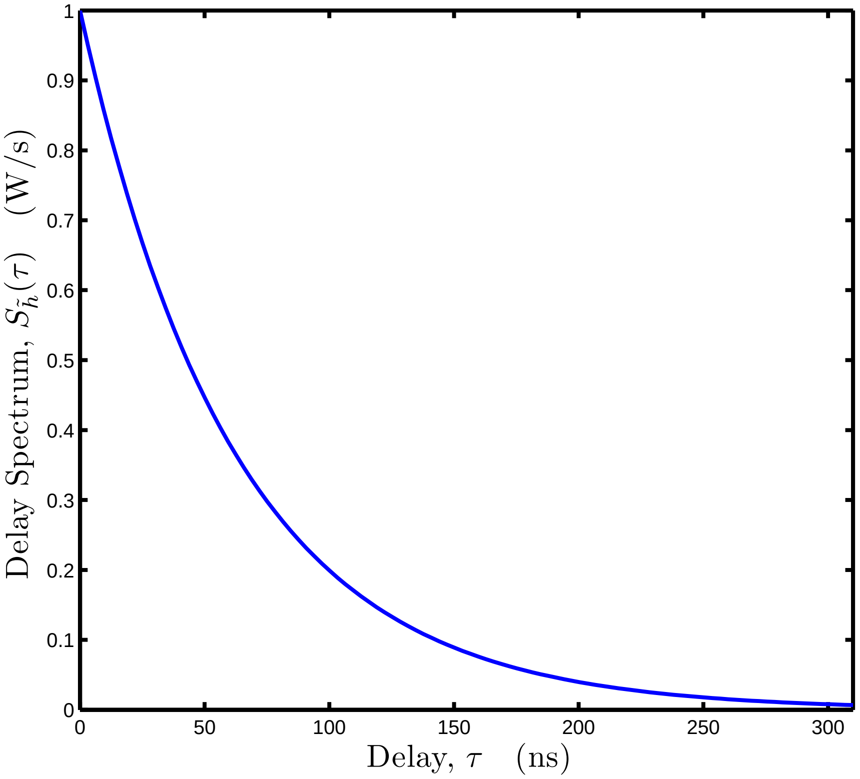

Figure 9: The delay spectrum of many wireless channels can be described by an exponential function.

impulse would be smeared in time at the receiver due to the numerous multipath components. Equivalently, the RMS delay spread can be thought of as a measure of the frequency selectivity of the wireless channel (i.e., the rate of variation in $\tilde{h}(f, \vec{r}, t)$ as a function of frequency). A large RMS delay spread indicates a wide range of delays for multipath components , leading to high frequency selectivity. Conversely, a small RMS delay spread indicates a narrow range of delays, leading to low frequency selectivity.

2.5.2 Doppler Spectrum

The Doppler spectrum is the power spectral density of the channel as a function of radian frequency. It is defined as the Fourier transform of a channel's autocorrelation with respect to time and has the units of Watts/radian.

$$S_{\tilde{h}}(\omega) = \int\limits_{-\infty}^{\infty} C_{\tilde{h}}(\Delta t) e^{-j\omega\Delta t} d\Delta t \tag{27}$$

The Doppler spectrum represents an expectation of the power density at the receiver for a given Doppler shift. The Doppler spectrum for fixed static wireless channels is commonly described by a Gaussian function as shown in Figure 10. The Gaussian Doppler spectrum is centered at zero radians, indicating a fixed channel wherein the transmitter and receiver are both stationary. The width of the spectrum about zero is indicative of motion within the channel due to time-varying scatterers. Following the shape of the Gaussian spectrum, only a small percentage of the received multipath experiences a large Doppler shift; the majority of the multipath components experience little to no Doppler shift because most of the scatterers are either stationary or moving very slowly. This is analogous to the *Big-Slow Rule*, which states that "in most radio channels, bigger objects scatter more power but are less likely to move" [14].

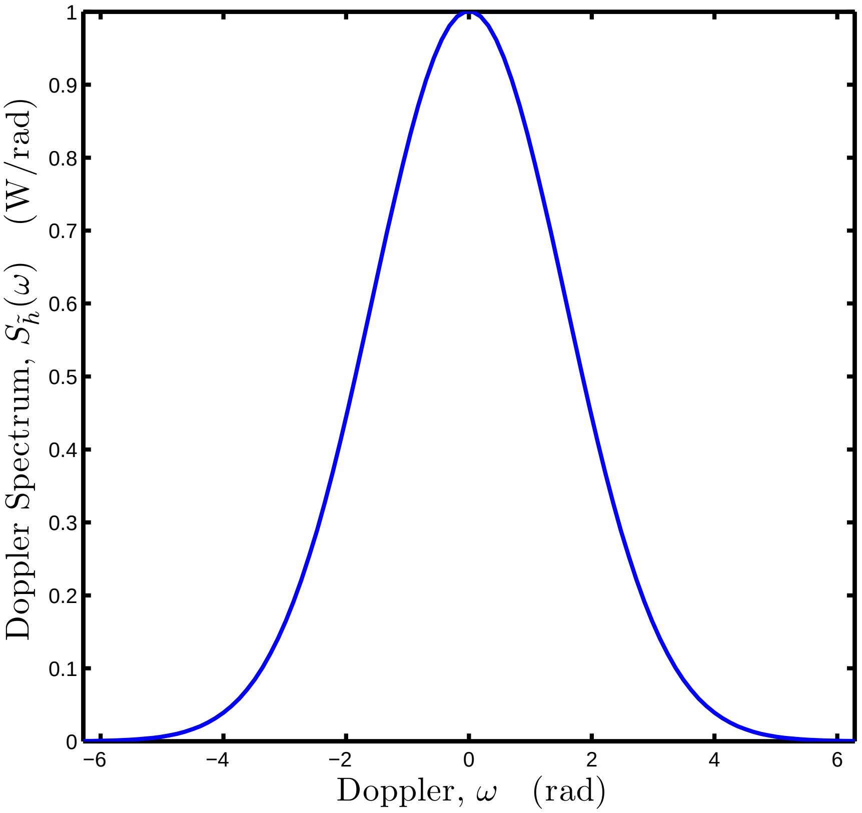

Figure 10: The Doppler spectrum for fixed wireless channels can oftentimes be described by a Gaussian function.

The Doppler spectrum is described by its width and centroid, which can be calculated from the n^{th} moment of the Doppler spectrum as given by

$$\overline{\omega^n} = \frac{\int\limits_{-\infty}^{\infty} \omega^n S_{\tilde{h}}(\omega) d\omega}{\int\limits_{-\infty}^{\infty} S_{\tilde{h}}(\omega) d\omega} \tag{28}$$

The first moment, $\overline{\omega}$, represents the centroid of the Doppler spectrum, and thereby, its mean Doppler shift.

The width of the Doppler spectrum is characterized by the root-mean square (RMS) *Doppler spread* of the PSD and can be calculated from the first and second moments according to

$$\sigma_\omega = \sqrt{\overline{\omega^2} - (\overline{\omega})^2} \tag{29}$$

The RMS Doppler spread may be thought of as a measure of the temporal selectivity of the wireless channel (i.e., the rate of variation in $\tilde{h}(f, \vec{r}, t)$ as a function of time). A large RMS Doppler spread indicates a large percentage of the multipath components experiencing large Doppler shifts, leading to high temporal selectivity. Conversely, a small RMS Doppler spread indicates a large percentage of the multipath components experience little to no Doppler shift, leading to low temporal selectivity.

2.5.3 Wavenumber Spectrum

The wavenumber spectrum is the power spectral density of the channel as a function of wavenumber. It is defined as the Fourier transform of a channel's autocorrelation with respect to space and has the units of Watts/(radian/meter).

$$S_{\tilde{h}}(k) = \int_{-\infty}^{\infty} C_{\tilde{h}}(\Delta r) e^{-jk\Delta r} d\Delta r \tag{30}$$

The wavenumber spectrum represents an expectation of the power density at the receiver for a given spatial radian frequency. More precisely, it represents the distribution of spatial radian frequencies k corresponding to the channel variation along a particular path r. Note that the wavenumber spectrum is a simplification of the more complicated, yet more descriptive wavevector spectrum, which describes the distribution of spatial radian frequencies along any vector in space. This shall be addressed in more detail in Section 2.6.

For a Rayleigh channel, in which homogeneous plane waves are arriving from all directions along the azimuth, the wavenumber spectrum is commonly described by the Clarke omnidirectional spectrum shown in Figure 11. The dominant spatial radian frequency of the channel's autocorrelation along this path will be $k_0 = c/f_0$, where f_0 is the carrier frequency and c is the speed of light.

The wavenumber spectrum is described by its width and centroid, which can be calculated from the n^{th} moment of the wavenumber spectrum as given by

$$\overline{k^n} = \frac{\int\limits_{-\infty}^{\infty} k^n S_{\tilde{h}}(k)dk}{\int\limits_{-\infty}^{\infty} S_{\tilde{h}}(k)dk} \tag{31}$$

The first moment, $\overline{k}$, represents the centroid of the wavenumber spectrum, and thereby, its mean wavenumber.

The width of the wavenumber spectrum is characterized by the root-mean square (RMS) *wavenumber spread* of the PSD and can be calculated from the first and second moments according to

$$\sigma_k = \sqrt{\overline{k^2} - (\overline{k})^2} \tag{32}$$

The RMS wavenumber spread may be thought of as a measure of the spatial selectivity of the wireless channel (i.e., the rate of variation in $\tilde{h}(f, \vec{r}, t)$ as a function of space) along a given path. A large RMS wavenumber spread indicates that movement along

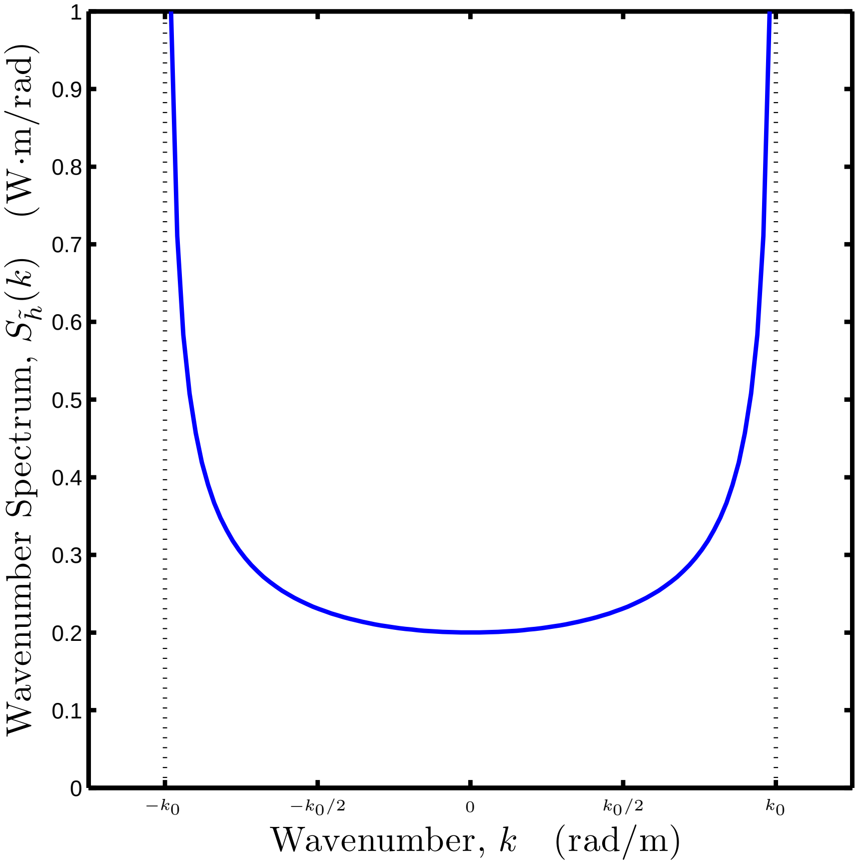

Figure 11: The Clarke wavenumber spectrum describes the spatial characteristics of an omnidirectional channel.

the path will cause rapid variations in the channel, leading to high spatial selectivity. Conversely, a small RMS wavenumber spread indicates that the channel has little to no variation along the path, leading to low spatial selectivity.

2.6 Angle Spectrum

The wavenumber spectrum is a simplification of the more complicated wavevector spectrum, which is defined as the Fourier transform of the wireless channel's vector space autocorrelation, $C_{\tilde{h}}(\Delta\vec{r})$. Thereby, the wavevector spectrum is

$$S_{\tilde{h}}(\vec{k}) = \int_{-\infty}^{\infty} C_{\tilde{h}}(\Delta\vec{r}) e^{-j\vec{k}\cdot\Delta\vec{r}} d\Delta\vec{r} \tag{33}$$

While being a more accurate representation of the wireless channel's spatial information, the wavevector spectrum's vector dependence makes it a most unintuitive tool for channel analysis. However, if we assume the wireless channel within a local area may be modeled as a stochastic local area channel with uncorrelated scattering, then we are able to work with an alternative representation of the wavevector spectrum given by

$$S_{\tilde{h}}(\vec{k}) = \frac{(2\pi)^3 \delta(|\vec{k}| - k_0)}{k_0^2} p(\theta, \psi) \tag{34}$$

where $p(\theta, \psi)$ is the *angle spectrum* as defined according to (35).

$$p(\theta, \psi) = \sum_{i=1}^{N} \frac{P_i \delta(\psi - \psi_i) \delta(\theta - \theta_i)}{\cos \psi_i} \tag{35}$$

In $p(\theta, \psi)$, θ is the azimuth angle and ψ is the elevation angle. The angle pair (θ_i, ψ_i) represents the angle-of-arrival (AoA) of the i^{th} homogeneous plane wave with wavevector $\vec{k_i}$ carrying power P_i. Integration across all values of θ and ψ will yield the average received power in the local area.

$$P_R = \int_{0}^{2\pi} \int_{-\pi/2}^{\pi/2} p(\theta, \psi) \cos(\psi) d\psi d\theta \tag{36}$$

2.6.1 Azimuth Spectrum

If one were to consider the simplified scenario in which multipath components were restricted to from-the-horizon propagation ($\psi_i = 0$), then the angle spectrum would reduce to (37).

$$p(\theta) = \sum_{i=1}^{N} P_i \delta(\theta - \theta_i) \tag{37}$$

This *azimuth spectrum* is a trade-off between a mathematically rigorous description and an intuitive representation. The azimuth spectrum ignores multipath components with a non-zero elevation angle, but by doing so, allows one to depict received power as a function of azimuth angle-of-arrival in polar coordinates. This leads to a graphical representation of the channel's spatial behavior that is much easier to intepret as compared to the wavevector or wavenumber spectrums. Furthermore, from-the-horizon propagation is considered a fairly safe approximation for many wireless channels and is commonly employed to simplify the channel modeling problem.

The width of the azimuth spectrum is characterized by the *angular spread*, Λ, which may be calculated according to

$$\Lambda = \sqrt{1 - \frac{|F_1|^2}{F_0^2}} \tag{38}$$

where F_n is the n^{th} Fourier coefficient of the azimuth spectrum as given by

$$F_n = \int_{0}^{2\pi} p(\theta) e^{jn\theta} d\theta \tag{39}$$

In physical terms, the angular spread is a measure of how multipath concentrates about a single azimuth direction. The angular spread takes on a value in the range

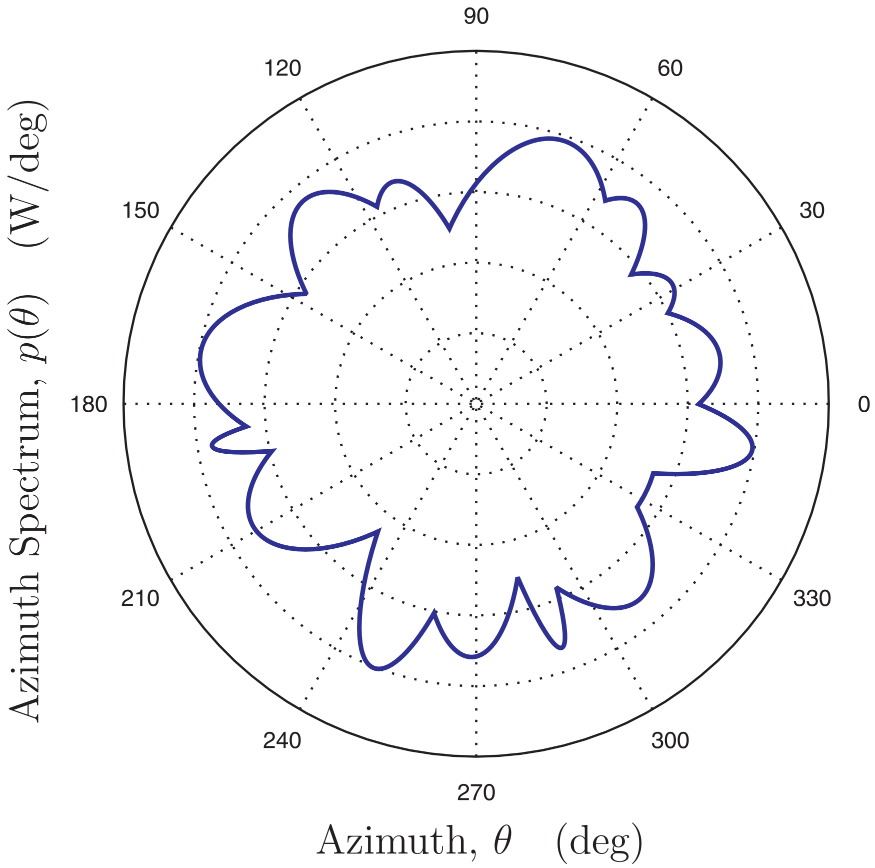

Figure 12: The azimuth spectrum describes received power as a function of azimuth angle of arrival.

$\Lambda \in [0, 1]$, with $\Lambda = 0$ corresponding to a small spread and $\Lambda = 1$ corresponding to a large spread.

2.6.2 Angular Spread from Wavenumber Spread

Calculating the angular spread directly from the azimuth spectrum is not always practical, because deriving the azimuth spectrum requires either the wavevector spectrum or a collection of directional channel measurements. As an alternative approach, the angular spread may be derived from a pair of wavenumber spreads corresponding to two orthogonal tracks within a local area [14]. Given two such wavenumber spreads, $\sigma_{k,x}$ and $\sigma_{k,y}$, the angular spread may be calculated according to

$$\Lambda = \sqrt{\frac{\sigma_{k,x}^2 + \sigma_{k,y}^2}{2\sigma_{k,omni}^2}} \tag{40}$$

where $\sigma_{k,omni}$ is the wavenumber spread for the canonical Rayleigh channel as defined by

$$\sigma_{k,omni} = \frac{k_0}{\sqrt{2}} \tag{41}$$

and k_0 is the wavenumber of the RF carrier.

2.6.3 Angular Spread from Spatial Fading Rate Variance

Finally, for the specific case of a space-ergodic SLAC with independent phases and heterogeneous scattering, one may alternatively calculate the angular spread from nonconherent measurements of *power spatial fading rate variance* along two orthogonal tracks [13]. Power spatial fading rate variance, denoted $\sigma_{\hat{r}}^2$, is a measure of the expected spatial fluctuations of the magnitude-squared channel in the $\hat{r}$ direction.

$$\sigma_{\hat{r}}^2 = \left\langle \left(\frac{\partial}{\partial r} \left| \tilde{h}(\vec{r} \cdot \hat{r}) \right|^2 \right)^2 \right\rangle_r \tag{42}$$

Given two such power spatial fading rate variances, $\sigma_{\hat{x}}^2$ and $\sigma_{\hat{y}}^2$, corresponding to two orthogonal tracks whereby $\hat{x} \cdot \hat{y} = 0$, the angular spread may be calculated according to

$$\Lambda = \frac{1}{k_0 P_R} \sqrt{\frac{\sigma_{\hat{x}}^2 + \sigma_{\hat{y}}^2}{2}} \tag{43}$$

where k_0 is the wavenumber corresponding to the RF carrier.

CHAPTER III

SLIDING CORRELATOR CHANNEL SOUNDER: DESIGN

The sliding correlator channel sounder performs channel measurements in the time domain by transmitting a direct sequence spread spectrum (DSSS) signal, which uses biphase shift keying (BPSK) to modulate an RF carrier with pseudo-random noise. The following sections provide a rigorous mathematical treatment of the operation of a sliding correlator channel sounder.

3.1 Pseudo-Random Noise

The ideal transmit signal for time domain channel sounding would resemble Gaussian white noise, which is characterized by infinite bandwidth, constant power spectral density across this bandwidth, and a random amplitude described by a Gaussian PDF. Unfortunately, the stochastic nature of true Gaussian white noise makes it unsuitable for swept time-delay channel sounding, because the exact transmit signal must be known at the receiver a priori. Therefore, the truly ideal signal would be a deterministic approximation to the non-deterministic Gaussian white noise.

One possible realization of "deterministic noise" is *pseudo-random noise.* The noise-like properties of pseudo-random noise (PN) stem from its corresponding pseudo-random binary sequence. Despite being wholly deterministic, pseudo-random binary sequences actually exhibit statistical randomness, making them excellent building blocks for generating analog waveforms that also exhibit statistical randomness.

3.1.1 Pseudo-Random Binary Sequences

We shall begin this discussion from a purely mathematical perspective as discussed in [19]. Consider a binary sequence, a_i, such that $a_i \in \{0, 1\}$. Let us suppose we wish a_i to represent the i^{th} trial in an experiment whereby $\Pr(a_i = 0) = 0.5$ and $\Pr(a_i = 1) = 0.5$. In this scenario, we would expect the following results:

- The number of '0's would approximately equal the number of '1's.
- Runs of consecutive '1's or '0's would occur such that 1/2 have a length of one, 1/4 have a length of two, 1/8 have a length of three, and so forth.

To make things more manageable, let us assume that we are dealing with a finite repeating sequence. Thereby, a_i has a period L such that $a_{i+L} = a_i$. One method of generating such a sequence is through a feedback mechanism whereby the n^{th} term in the sequence is determined from a linear combination of the previous N terms as described in Equation (44). Henceforth, we shall refer to such a sequence as a *pseudo-random binary sequence.*

$$a_n = \sum_{i=1}^{N} c_i a_{n-i} \tag{44}$$

In (44), $c_i \in \{0, 1\}$ may be thought of as the feedback coefficients that determine which of the previous N terms contribute to the value of the n^{th} term. Note that to determine the zeroth term in the sequence, one requires knowledge of $\{a_{-N}, a_{1-N}, \ldots, a_{-2}, a_{-1}\}$. It is assumed that $c_N = 1$ so that a_{n-N} is required to calculate a_n. Further, it should be noted that the operators described in (44) involve Boolean arithmetic (i.e., the summation uses modulo 2 addition).

Using the feedback coefficients, c_i, one may describe the pseudo-random binary sequence, a_i, by a *characteristic polynomial*, $f(x)$, according to

$$f(x) = 1 - \sum_{i=1}^{N} c_i x^i \tag{45}$$

Let us define a polynomial, $G(x)$, as the reciprocal of $f(x)$.

$$G(x) = \frac{1}{f(x)} \tag{46}$$

It can be shown that the coefficients of the terms of $G(x)$ are themselves the terms from a_i. Therefore, $G(x)$ is commonly referred to as the *generating function* of a_i [19].

$$G(x) = \sum_{i=0}^{\infty} a_i x^i \tag{47}$$

One important caveat of Equation (47) is that it assumes the sequence as derived from Equation (44) was seeded such that $\{a_{-N}, a_{1-N}, \cdots, a_{-2}\} = 0$ and $\{a_{-1}\} = 1$. For any other seeding such that the N initial terms are not all simultaneously zero, the resulting pseudo-random binary sequence will be a phase shifted version of a_i in (47).

Recalling the assumption that our sequence a_i has a length L, it may be shown that L is the smallest integer such that $f(x)$ divides evenly into $1 - x^L$ modulo 2 [19].

$$\frac{1 - x^L}{f(x)} = \sum_{i=0}^{L-1} a_i x^i \tag{48}$$

Note that this ratio of polynomials produces a quotient whose coefficients represent one period of the pseudo-random binary sequence.

3.1.2 Maximal Sequences

An important and extremely useful class of pseudo-random binary sequences are *maximal sequences*, or *m-sequences* for short. M-sequences have the longest possible period L for a sequence produced from the recursive algorithm in (44) that uses the previous N terms [9]. The period of an m-sequence is given by

$$L = 2^N - 1 \tag{49}$$

Therefore, the most "efficient" characteristic polynomials will produce m-sequences, as they lead to the longest non-repeating sequences from the fewest previous terms. Furthermore, m-sequences exhibit several key properties that contribute to their pseudo-randomness [19]. Namely,

1. A period of the sequence contains 2^{N-1} '1's and $2^{N-1} - 1$ '0's. Therefore, the number of '1's is one greater than the number of '0's.
2. A period of the sequence contains every possible N-tuple excepting all '0's.
3. For $b_i = 2a_i - 1$, the autocorrelation of b_i denoted as $C_{b_i}(\tau)$ is such that

$$C_{b_i}(\tau) = \frac{1}{L}\sum_{i=1}^{L} b_i b_{i+\tau} = \begin{cases} 1 & \text{if} \quad \tau = 0 \\ -1/L & \text{if} \quad 0 < \tau < L \end{cases}$$

The first statement says that the number of '1's in the sequence is approximately the same as the number of '0's. This is the expected result for a sequence in which $\Pr(a_i = 0) = \Pr(a_i = 1) = 1/2$. The second statement says that the all zeros case is the only N bit sequence that will never occur within an m-sequence. This N-tuple is in fact forbidden, as it leads to a trapped state whereby (44) will always evaluate to zero. Therefore, the m-sequence length L corresponds to the fact that, of the 2^N possible permutations of an N-tuple, only one state (all zeros) will never occur. Thus, $L = 2^N - 1$. The third statement says that two identically scaled and shifted m-sequences will only exhibit a significant correlation when their phases are aligned. This property becomes especially useful later when we examine the autocorrelation of pseudo-random noise, which is derived directly from pseudo-random binary sequences.

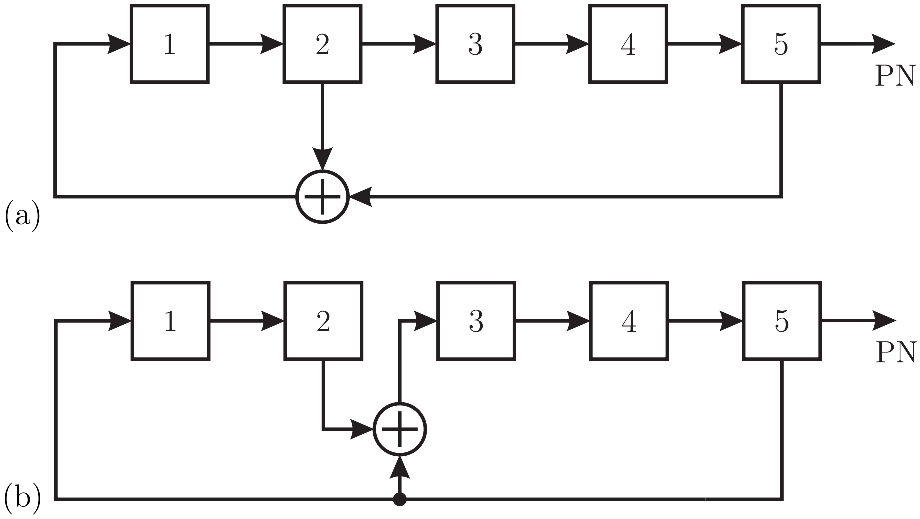

Figure 13: Examples of the two linear feedback shift register architectures: (a) simple shift register generator (SSRG) and (b) modular shift register generator (MSRG). The $\bigoplus$ denotes modulus 2 addition.

3.1.3 Linear Feedback Shift Register

The *linear feedback shift register* is a hardware realization of the recursive algorithm described by Equation (44) and thereby provides a means of generating an m-sequence. An N-bit shift register holds the previous N terms of the m-sequence. To determine a_n, the terms in the i^{th} registers are weighted according to their respective feedback coefficients, c_i, and summed modulus 2 using XOR gates. At each clock cycle, the summation is fed into the input of the shift register and the $(n-N)^{th}$ term is shifted out. This implementation is know as the *simple shift register generator* (SSRG) and is depicted in Figure 13(a) [9].

As opposed to weighting terms using the feedback coefficients themselves, only registers corresponding to $c_i = 1$ are used as part of the feedback configuration. Thereby, the set of feedback registers for the SSRG architecture, denoted F_s, may be determined according to

$$F_s = \{i\} \text{ for all } i > 0 \text{ such that } c_i = 1 \tag{50}$$

The characteristic polynomial $f(x)$ described in (45) may be recognized as an exact description of the feedback configuration of the SSRG. For example, if the characteristic polynomial was $f(x) = 1 - x^2 - x^5$, then when $i = \{2, 5\}$, $c_i = 1$. Therefore, the set of feedback registers is $F_s = \{2, 5\}$.

Figure 13(b) shows an alternative implementation of the linear feedback shift register called the *modular shift register generator* (MSRG) [9]. This architecture may be thought of as the complement of the SSRG. Whereas the SSRG feedback configuration involves multiple register outputs and a single shift register input, the MSRG feedback configuration involves a single register output and multiple register inputs. In the MSRG architecture, the output of the N^{th} register is summed modulus 2 with the output of the $(j-1)^{th}$ register and fed into the j^{th} register. The output of the N^{th} register also feeds the input of the shift register.

Note that for the MSRG, the characteristic polynomial does not directly describe the feedback configuration. The set of feedback registers in the MSRG architecture, denoted F_m, may be determined according to

$$F_m = \{j, N\} \tag{51}$$

where

$$j = N - i \text{ for all } i < N \text{ such that } c_i = 1 \tag{52}$$

For example, if the characteristic polynomial was $f(x) = 1 - x^2 - x^5$, then when $i = \{2, 5\}$, $c_i = 1$. Noting that $N = 5$, we have $j = \{3\}$ and $F_m = \{3, 5\}$.

The SSRG architecture is generally simpler to implement but can suffer from long propagation delays through the cascade of XOR gates. The MSRG architecture provides a very flexible template should one wish to create a reconfigurable pseudorandom binary sequence generator. Also, the parallel arrangement of the XOR gates provides shorter propagation delays along the feedback loop, thereby allowing faster clock rates. However, the tradeoff is the added complexity of the design.

As implemented with digital ICs, the output of a linear feedback shift register is a digital waveform consisting of a sequence of '1's and '0's. However, like all real-world time-varying digital signals, the output is also an analog waveform consisting of a train of rectangular pulses with bit-dependent amplitudes. Therefore, whether the output of a linear feedback shift register is referred to as an m-sequence or pseudo-random noise is a matter of perspective and/or application, but the distinction is helpful when discussing concepts such as sequence length, chip rate, and signal period.

3.1.4 Analog Representation

Consider an N-bit linear feedback shift register configured as a simple shift register generator. The feedback registers, F_s, are selected such that the resulting pseudo-random binary sequence, a_i, is an m-sequence of length $L = 2^N - 1$. The shift register is clocked at a frequency of f_c such that, after every $1/f_c$ seconds, the next term of the m-sequence is generated. We are dealing with digital hardware, so we expect each term to be represented by an ideal rectangular pulse with duration $T_c = 1/f_c$. Let us assume a biphase output with amplitude $\pm V_0$ whereby $a_i = 0$ corresponds to $-V_0$ and $a_i = 1$ corresponds to $+V_0$. This arrangement produces an analog waveform, $x(t)$, that is the pseudo-random noise (PN) derived from the m-sequence a_i. We may represent $x(t)$ as

$$x(t) = \sum_{i \in \mathbb{Z}} V_0(2a_i - 1)\Pi(t/T_c - i - 1/2) \tag{53}$$

where $\mathbb{Z}$ as the set of all real integers, $\Pi(\xi)$ is the rectangular function given by

$$\Pi(\xi) = \mathrm{u}(1/2 - |\xi|) \tag{54}$$

and $\mathrm{u}(\xi)$ is the Heaviside step function. Thus, the PN is an infinite train of rectangular pulses with the value of the i^{th} pulse determined by the i^{th} term of the m-sequence.

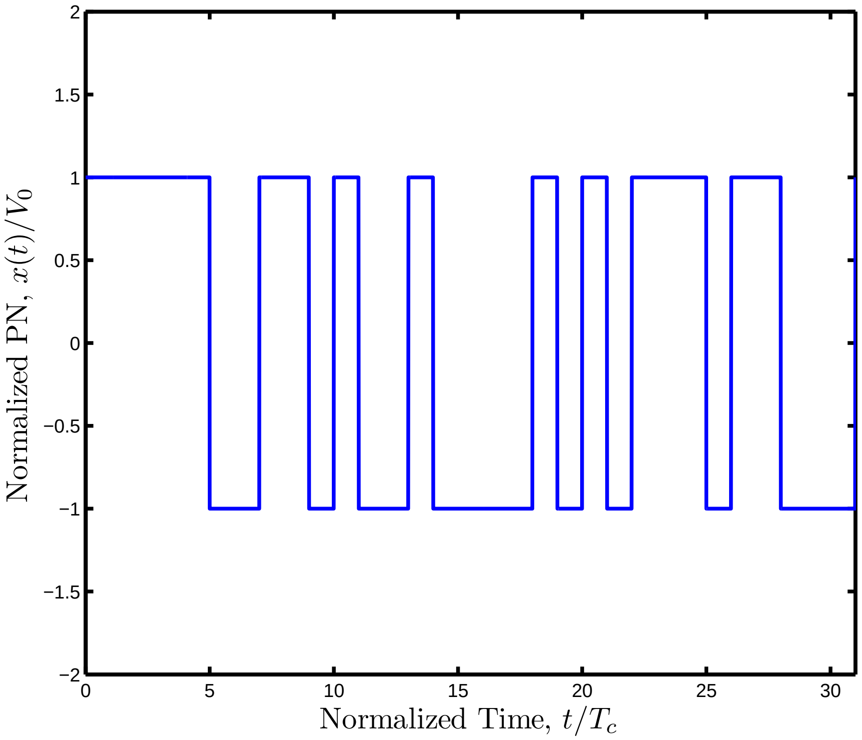

Figure 14: Pseudo-random noise derived from an m-sequence of length 31.

Figure 14 shows a PN derived from an m-sequence of length $L = 31$. The pseudo-randomness of the m-sequence contributes to the apparently random amplitude of each pulse. Note that in the literature, it is common to refer to each pulse as a *chip*. Similarly, the shift register clock rate, f_c, is typically referred to as the *chip rate* [2].

3.1.5 Autocorrelation

The autocorrelation of a periodic time-varying signal $\xi(t)$ is defined as [34]

$$C_\xi(\tau) = \lim_{T\to\infty} \left\{ \frac{1}{2T} \int_{-T}^{T} \xi(t)\xi(t-\tau)dt \right\} \tag{55}$$

Thus, the autocorrelation of the periodic PN $x(t)$ is

$$C_x(\tau) = V_0^2 \left[\sum_{i\in\mathbb{Z}} \left\{ (1+1/L)\, \Lambda\!\left(\frac{\tau - iLT_c}{T_c} \right) \right\} - \frac{1}{L} \right] \tag{56}$$

where $\Lambda(\xi)$ is the triangle function given by

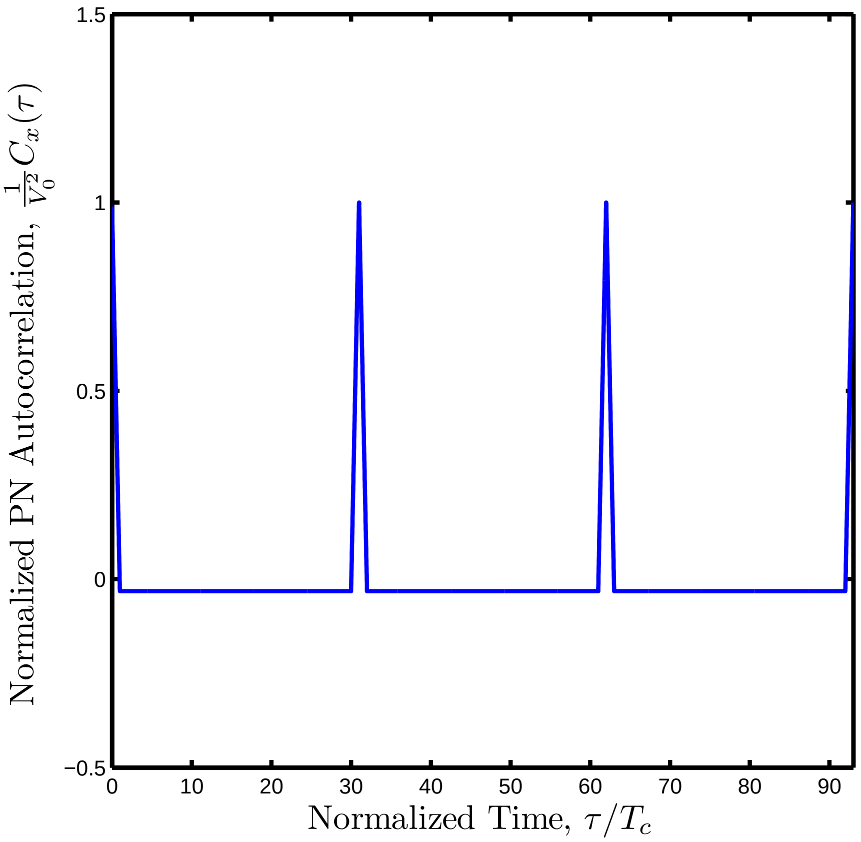

Figure 15: The autocorrelation of a PN is characterized by a train of sharp triangular peaks, each with a base width of $2T_c$.

$$\Lambda(\xi) = (1 - |\xi|)\mathrm{u}(1 - |\xi|) \tag{57}$$

Equation (56) describes a train of triangular pulses with a base width of $2T_c$, a maximum amplitude of V_0^2, a period of LT_c, and a DC offset of $-V_0^2/L$ [3]. Figure 15 shows the autocorrelation of a PN of length $L = 31$.

3.1.6 PN Frequency Spectrum

Any periodic signal $\xi(t)$ may be represented as a Fourier series of the form

$$\xi(t) = \sum_{k\in\mathbb{Z}} \tilde{a}_k e^{j2\pi f_0 kt} \tag{58}$$

where $\tilde{a}_k$ is the Fourier series coefficient corresponding to the exponential of frequency f_0k and f_0 is the fundamental frequency of $\xi(t)$ as given by $1/T_0$ where T_0 is the signal period [21]. The values of $\tilde{a}_k$ may be found from (59), which is referred to as the Fourier analysis equation.

$$\tilde{a}_k = \frac{1}{T_0} \int\limits_{-T_0/2}^{T_0/2} \xi(t) e^{-j2\pi f_0 k t} dt \tag{59}$$

Accordingly, the Fourier series coefficients of the PN, $x(t)$, are found to be

$$\tilde{a}_k = \frac{V_0}{L} \operatorname{sinc}\left(\frac{k}{L}\right) e^{\frac{jk\pi}{L}} \sum_{i=1}^{L} \left[(2a_i - 1)\, e^{\frac{-jk2\pi}{L} i} \right] \tag{60}$$

where $\operatorname{sinc}(x) = \frac{\sin(\pi x)}{\pi x}$. Substituting f_c/L for f_0 in (58), one may express the PN as

$$x(t) = \frac{V_0}{L} \sum_{k\in\mathbb{Z}} \operatorname{sinc}\left(\frac{k}{L}\right) e^{\frac{jk\pi}{L}} \sum_{i=1}^{L} \left[(2a_i - 1)\, e^{-\frac{jk2\pi}{L} i} \right] e^{j2\pi \frac{f_c k}{L} t} \tag{61}$$

The spectrum, $\tilde{\Xi}(f)$, of a signal, $\xi(t)$, is given by its Fourier transform according to

$$\tilde{\Xi}(f) = \int\limits_{-\infty}^{\infty} \xi(t) e^{-j2\pi f t} dt \tag{62}$$

Therefore, the PN's spectrum, $\tilde{X}(f)$, is

$$\tilde{X}(f) = \frac{V_0}{L} \sum_{k\in\mathbb{Z}} \operatorname{sinc}\left(\frac{k}{L}\right) \delta\left(f - \frac{f_c k}{L}\right) e^{\frac{jk\pi}{L}} \sum_{i=1}^{L} \left[(2a_i - 1)\, e^{-\frac{jk2\pi}{L} i} \right] \tag{63}$$

where $\delta(\xi)$ is the Dirac delta function. Thus, the spectrum of a PN is characterized by a train of Dirac delta functions at integer multiples of $\frac{f_c}{L}$. Taking the magnitude of (63) according to Equation (64), it is seen that $|\tilde{X}(f)|$ is bounded by $\operatorname{sinc}\left(\frac{k}{L}\right)$ [19].

$$|\tilde{X}(f)| = \frac{|V_0|\sqrt{L+1}}{L} \sum_{k\in\mathbb{Z}} \operatorname{sinc}\left(\frac{k}{L}\right) \delta\left(f - \frac{f_c k}{L}\right) \tag{64}$$

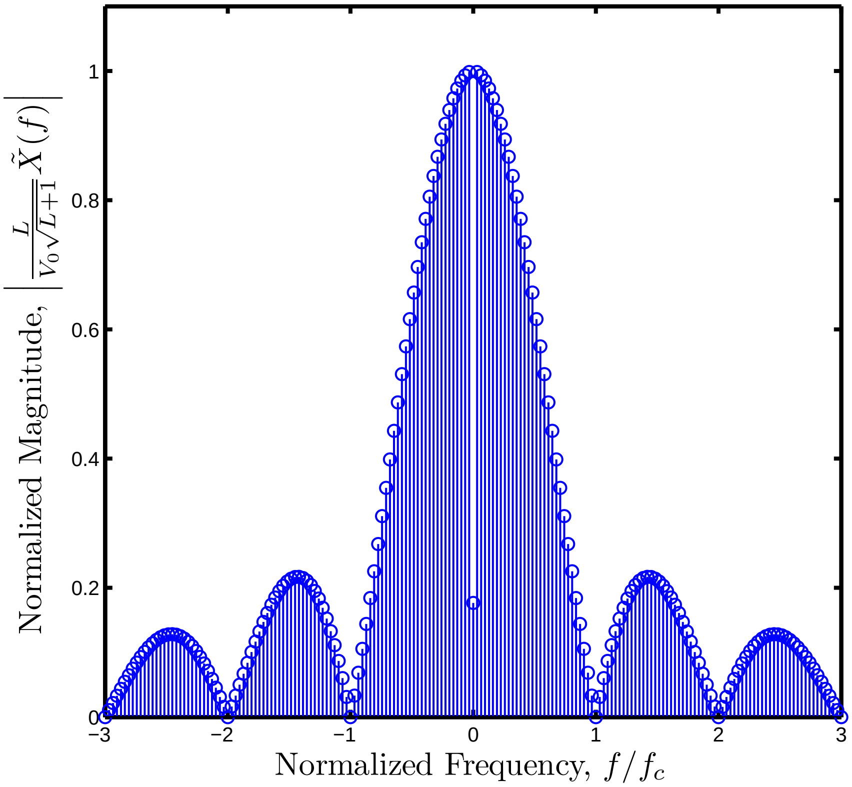

Figure 16: The frequency spectrum of a PN is characterized by a train of Dirac delta functions under a $\operatorname{sinc}\left(\frac{f}{f_c}\right)$ envelope.

Noting that the spectrum is nonzero only when $(f - \frac{f_c k}{L}) = 0$, the spectrum's magnitude bound may be equivalently expressed as $\operatorname{sinc}\left(\frac{f}{f_c}\right)$. Figure 16 shows the magnitude of the spectrum of a PN derived from an m-sequence of length $L = 31$. Note that the majority of the power is concentrated between f_c and $-f_c$. This region is oftentimes described as the "main lobe" of the PN spectrum.

3.2 Spread Spectrum Channel Sounding

The PN is our noise-like signal that we will transmit through the wireless channel. At the receiver, we will make use of the PN's sharp triangular autocorrelation to detect the arrival of our signal. In telecommunications, this is known as a correlation receiver [21]. The correlation receiver is based upon the cross-correlation operation, which is a generalization of the autocorrelation. For two signals $\tilde{\xi}(t)$ and $\tilde{\zeta}(t)$, the

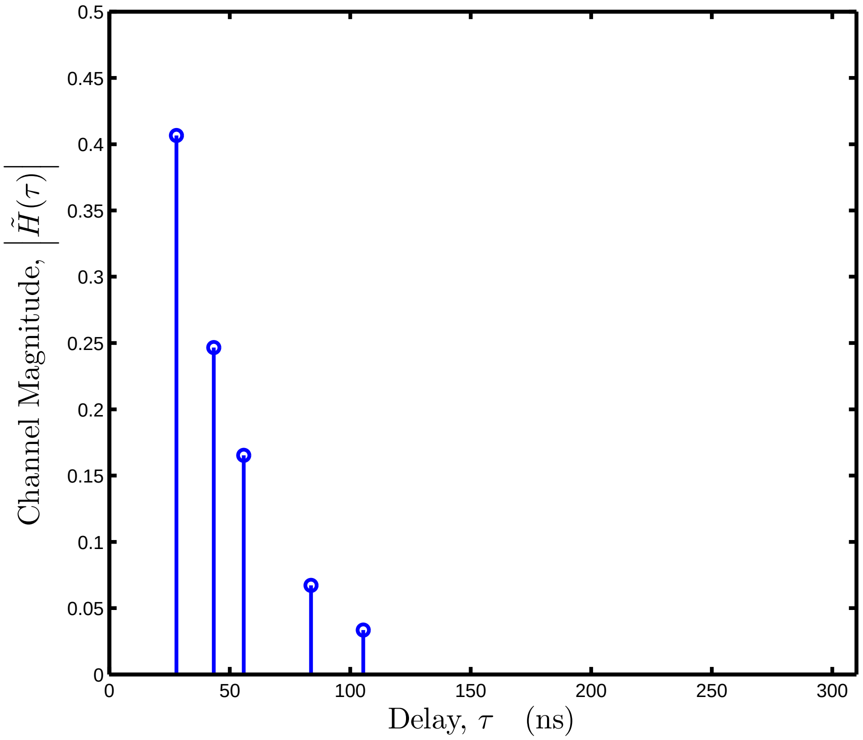

Figure 17: A common model for the CIR of a fixed static wireless channel is the tapped-delay line whereby $\tilde{H}(\tau)$ is the summation of multiple delayed and scaled Dirac delta functions.

cross-correlation $C_{\tilde{\xi}\tilde{\zeta}}(\tau)$ is given by

$$C_{\tilde{\xi}\tilde{\zeta}}(\tau) = \int_{-\infty}^{\infty} \tilde{\xi}(t)^* \tilde{\zeta}(t-\tau)dt \tag{65}$$

To get a better idea of how the correlation receiver may be used for temporal channel sounding, let us consider the tapped-delay line channel model. Assuming a fixed, static wireless channel, one may model the CIR, $\tilde{H}(\tau)$, as a tapped-delay line whereby individual multipath components are delayed and complex-scaled copies of the transmitted signal [52]. Therefore, $\tilde{H}(\tau)$ may be expressed as the summation of N Dirac delta functions, each with a complex amplitude $\tilde{\alpha}_i$ and delay τ_i.

$$\tilde{H}(\tau) = \sum_{i=1}^{N} \tilde{\alpha}_i \delta(\tau - \tau_i) \tag{66}$$

This follows from the formulation of the SLAC model described in Section 2.4. Figure 17 depicts a possible CIR for a tapped-delay line wireless channel.

If the PN $x(t)$ were transmitted through the wireless channel described by $\tilde{H}(\tau)$, the received signal $\tilde{y}(t)$ as determined by Equation (3) will be a train of delayed and scaled copies of $x(t)$.

$$\tilde{y}(t) = \sum_{i=1}^{N} \tilde{\alpha}_i x(t - \tau_i) \tag{67}$$

We find that the cross-correlation of $\tilde{y}(t)$ with the originally transmitted signal $x(t)$ is

$$C_{x\tilde{y}}(\tau) = \sum_{i=1}^{N} \tilde{\alpha}_i C_x(\tau - \tau_i) \tag{68}$$

where $C_x(\tau)$ is the autocorrelation of the PN. Figure 18 shows a possible $C_{x\tilde{y}}(\tau)$ assuming $\tilde{H}(\tau)$ is the same wireless channel as depicted in Figure 17.

Note that (68) is equivalently the tapped-delay line representation of the wireless channel convolved with the autocorrelation of the transmitted signal. Thereby, the delay, τ_i, of a multipath component is indicated by the delay of the autocorrelation. Similarly, the complex amplitude, $\tilde{\alpha}_i$, of a multipath component is indicated by the complex scaling of the autocorrelation. Thus, $C_{x\tilde{y}}(\tau)$ is equivalently a scaled copy of the band-limited CIR, $\tilde{H}_{BL}(\tau)$, as measured using $x(t)$.

$$\tilde{H}_{BL}(\tau) = \frac{1}{V_0^2} C_{x\tilde{y}}(\tau) \tag{69}$$

By transmitting a PN with finite bandwidth, we define the bandwidth of the channel that we are measuring. The measured CIR resulting from the cross-correlation of the transmitted and received signals reflects this band-limited channel. More precisely, the bandwidth of the transmitted signal's autocorrelation defines the bandwidth of the measured CIR. Had we an infinite bandwidth signal at our disposal with a similarly

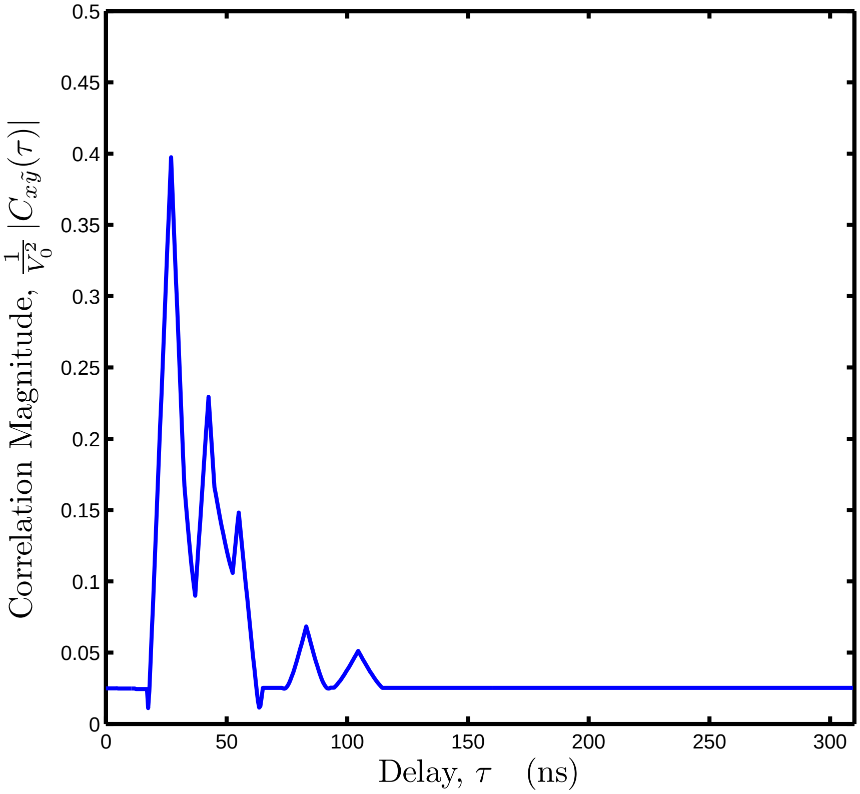

Figure 18: Cross-correlation of the received signal $\tilde{y}(t)$ with the originally transmitted signal $\tilde{x}(t)$ leads to a band-limited representation of the CIR whereby $\delta(\tau - \tau_i)$ is replaced by $C_x(\tau - \tau_i)$. Here, we assume that $x(t)$ is a PN with $L = 31$ such that $C_x(\tau)$ is the PN autocorrelation defined in (56).

infinite bandwidth autocorrelation, then we would be able to determine the CIR for the *infinite bandwidth* CIR described by the tapped-delay line in Equation (66).

3.2.1 Practical Considerations

The cross-correlation described in Equation (68) is typically implemented in software. The received signal $\tilde{y}(t)$ would be sampled by an ADC, and the data would either be processed by an FPGA or stored on a computer for post-processing. To properly digitize the received signal, the ADC's sampling rate must be equal to or greater than twice the baseband bandwidth [47]. For narrow-band measurements, this issue is rather trivial. However, as the measurement bandwidth increases, so too does the cost of the required high-speed ADC. Thus, to ease the hardware requirements for measuring wideband wireless channels, researchers have used the sliding correlator technique described in [6] to time-dilate the channel impulse response.

3.3 Sliding Correlator

The purpose of the sliding correlator is to produce a time-dilated PN autocorrelation, which will lead to a time-dilated cross-correlation according to (68). Whereas the true autocorrelation uses two *identical* signals, the sliding correlator's autocorrelation involves two *similar* signals, whereby one signal is slightly "slower" in time compared to the other. Multiplying these two similar signals together and carefully filtering their product will yield a very close approximation to a time-dilated autocorrelation.

3.3.1 Multiplying the PNs

Consider two PNs, $x(t)$ and $x'(t)$, with chip rates, f_c and f_c', respectively. The PNs are derived from the same m-sequence of length L and have identical amplitudes such that $V_0 = V_0'$. Now, consider the waveform $p(\tau)$, which we shall call the *sliding correlator product* of the two PNs.

$$p(\tau) = x(\tau)x'(\tau) \tag{70}$$

Multiplication in the time domain is equivalently convolution in the frequency domain. Defining $\tilde{P}(f)$, $\tilde{X}(f)$, and $\tilde{X}'(f)$ as the Fourier transform pairs of $p(\tau)$, $x(\tau)$, and $x'(\tau)$, respectively, Equation (70) is equivalently

$$\tilde{P}(f) = \tilde{X}(f) \otimes \tilde{X}'(f) \tag{71}$$

For the PN spectrum described in (63), the convolution of two spectra with chip rates f_c and f_c' is

$$\begin{aligned}
&\tilde{P}(f) = \\
&\quad \left(\frac{V_0}{L}\right)^2 \sum_{k\in\mathbb{Z}} \sum_{k'\in\mathbb{Z}} \left\{ \delta\left(f - \frac{f_c k + f_c' k'}{L}\right) \operatorname{sinc}\left(\frac{k}{L}\right) \operatorname{sinc}\left(\frac{k'}{L}\right) \times \right. \\
&\quad \left. e^{-j\frac{\pi}{L}(k+k')} \sum_{i=1}^{L} \sum_{i'=1}^{L} \left[(2a_i - 1)(2a_{i'} - 1) e^{-j\frac{\pi}{L}(ki + k'i')} \right] \right\}
\end{aligned} \tag{72}$$

Recall that the goal of the sliding correlator is to produce a time-dilated version of the autocorrelation. Therefore, we might expect to find a train of triangle-shaped pulses buried within $p(\tau)$ that is equivalent to a time-dilated PN autocorrelation. Close inspection of (72) reveals that when $k' = -k$, the spectrum $\tilde{P}(f)$ collapses into the spectrum corresponding to a train of triangle-shaped pulses, which we will here denote as $\tilde{Q}_c(f)$.

$$\begin{aligned}
&\tilde{Q}_c(f) = \\
&\quad \left(\frac{V_0}{L}\right)^2 \sum_{k\in\mathbb{Z}} \left\{ \delta\left(f - k\frac{f_c - f_c'}{L}\right) \operatorname{sinc}^2\left(\frac{k}{L}\right) \times \right. \\
&\quad \left. \sum_{i=1}^{L} \sum_{i'=1}^{L} \left[(2a_i - 1)(2a_{i'} - 1) e^{-j\frac{\pi}{L}k(i-i')} \right] \right\}
\end{aligned} \tag{73}$$

Equation (73) is the spectrum of the time-dilated autocorrelation [3]. The remaining terms in the double summation of (72) represent the distortion to the time-dilated autocorrelation produced by the sliding correlation. The frequency domain distortion is here denoted as $\tilde{Q}_d(f)$.

$$\begin{aligned} &\tilde{Q}_d(f) = \\ &\quad \left(\frac{V_0}{L}\right)^2 \sum_{\substack{k,k' \in \mathbb{Z} \\ k' \neq -k}} \left\{ \delta\left(f - \frac{f_c k + f'_c k'}{L}\right) \operatorname{sinc}\left(\frac{k}{L}\right) \operatorname{sinc}\left(\frac{k'}{L}\right) \times \right. \\ &\qquad \left. e^{-j\frac{\pi}{L}(k+k')} \sum_{i=1}^{L} \sum_{i'=1}^{L} \left[(2a_i - 1)(2a_{i'} - 1)\, e^{-j\frac{\pi}{L}(ki + k'i')} \right] \right\} \end{aligned} \tag{74}$$

Let $q_c(\tau)$ and $q_d(\tau)$ represent the inverse Fourier transform for $\tilde{Q}_c(f)$ and $\tilde{Q}_d(f)$ respectively. The sliding correlator product, $p(\tau)$, may then be expressed as the superposition of the autocorrelation signal $q_c(\tau)$ and the distortion signal, $q_d(\tau)$ as discussed in [3].

$$p(\tau) = q_c(\tau) + q_d(\tau) \tag{75}$$

Figure 19(a) compares the spectrum for the time-dilated autocorrelation spectrum $\tilde{Q}_c(f)$ with its accompanying distortion spectrum $\tilde{Q}_d(f)$ for the case of $L = 31$ and $f'_c = 0.99 f_c$. Figure 19(b) compares the corresponding time-domain signals $q_c(\tau)$ and $q_d(\tau)$ for the same scenario. The time-dilated autocorrelation, $q_c(\tau)$, is seen to be buried amidst the distortion, $q_d(\tau)$. Therefore, it is important that one remove this distortion to produce a “clean” time-dilated autocorrelation.

3.3.2 Slide Factor

It is convenient to define the *slide factor*, γ, as the ratio of f_c to the difference between f_c and f'_c [6].

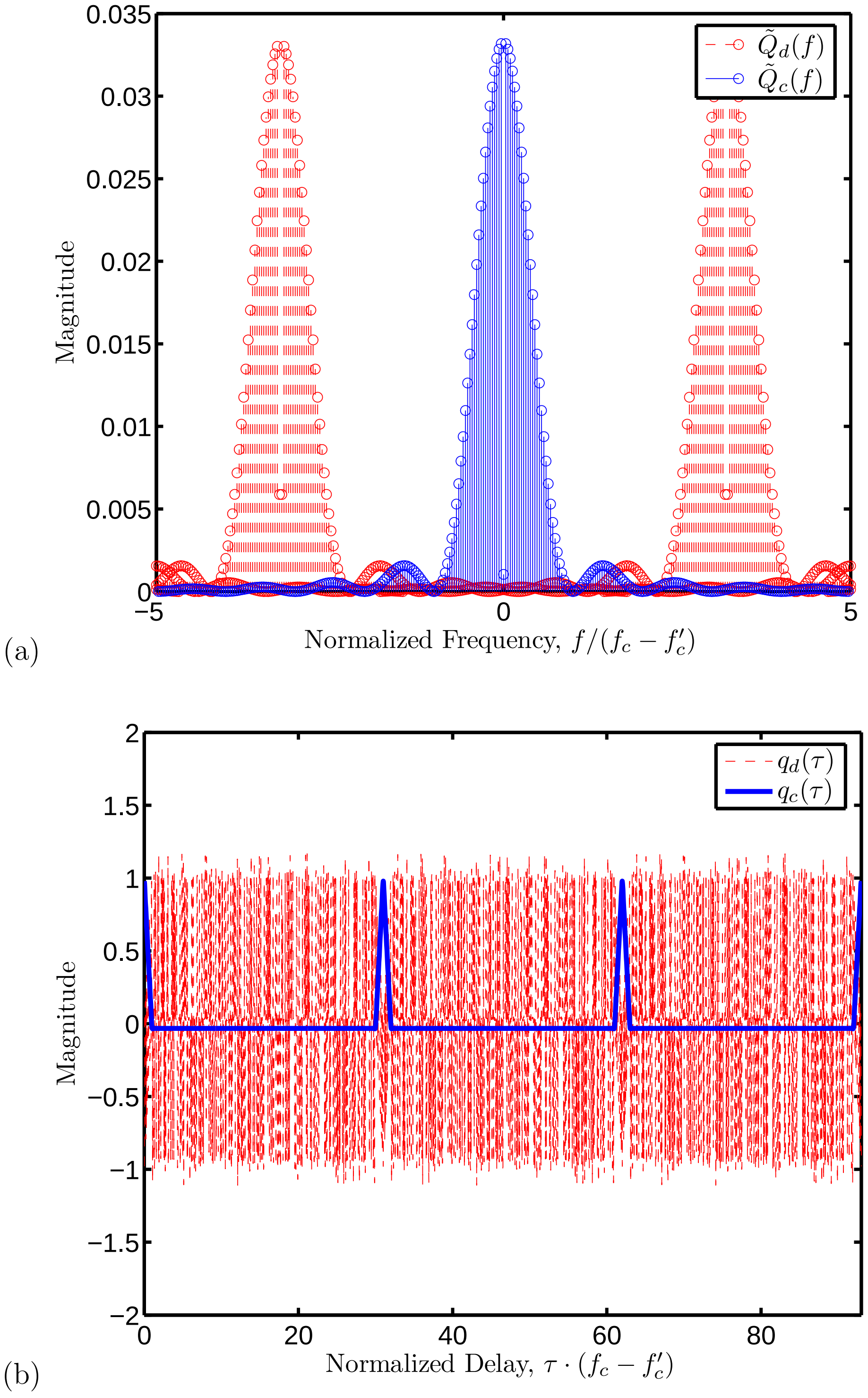

Figure 19: A comparison of the sliding correlator's autocorrelation signal and distortion signal for $L = 31$ and $f'_c = 0.99 f_c$ in the (a) time domain and (b) frequency domain.

$$\gamma = \frac{f_c}{f_c - f_c'} \tag{76}$$

The slide factor may be perceived as the temporal dilation factor for the sliding correlator's time-dilated autocorrelation. Therefore, $q_c(\tau)$ may be equivalently expressed as

$$q_c(\tau) = C_x\left(\frac{\tau}{\gamma}\right) \tag{77}$$

3.3.3 Filtering the Product

The simplest means of removing the unwanted distortion introduced by $q_d(\tau)$ is by low-pass filtering the sliding correlator product, $p(\tau)$. The time-dilated autocorrelation, $q_c(\tau)$, is centered at DC and has a $\mathrm{sinc}^2\left(f\frac{\gamma}{f_c}\right)$ envelope. Thus, the majority of its power resides within the main lobe as bounded by $f \in (-|f_c/\gamma|, |f_c/\gamma|)$. Let us assume an ideal rectangular low-pass filter, $\tilde{h}(f)$ with impulse response, $H(\tau)$, such that

$$\tilde{h}(f) = \mathrm{u}(f + |f_c/\gamma|) - \mathrm{u}(f - |f_c/\gamma|) \tag{78}$$

By filtering $p(\tau)$ with $H(\tau)$, a significant portion of the unwanted distortion will be removed while passing the majority of the time-dilated autocorrelation. However, filtering is only part of the solution for removing $q_d(\tau)$. The optimal approach requires the concerted selection of γ and L so that the majority of the distortion signal's power will be blocked by the low-pass filter.

3.3.4 Optimization

To produce a "clean" time-dilated autocorrelation, we must minimize the amplitude of $q_d(\tau)$. Here it is useful to define the dynamic range, D_R, of a sliding correlator in dB as

$$D_R = 20\log_{10}\left(\frac{\max(|Lq_c(\tau)\otimes H(\tau)|)}{\max(|Lq_d(\tau)\otimes H(\tau) - V_0^2|)}\right) \text{ (dB)} \tag{79}$$

For the ideal case of no distortion, we might remove the low-pass filter by setting $H(\tau)$ to $\delta(\tau)$. The dynamic range would then be $D_{R,ideal}$ as defined in Equation (80).

$$D_{R,ideal} = 20\log_{10}(L) \text{ (dB)} \tag{80}$$

Equation (80) is the typical result for a DSSS system using a true correlation receiver [9]. The distortion signal produced by the sliding correlator leads to a reduction in the dynamic range. Mathematically describing this degradation in dynamic range is difficult due to the nonlinear $\max(\cdot)$ operation on the complicated distortion signal described by (74). However, simulations based on Equation (79) indicate interesting trends for D_R with increasing slide factors. Figure 20 compares the dynamic range of PNs of various lengths for a range of γ/L values. For the simulation, the PN spectra $\tilde{X}(f)$ and $\tilde{X}'(f)$ were restricted to the range $f \in [-3f_c, 3f_c]$ and $f \in [-3f'_c, 3f'_c]$, respectively to minimize both memory requirements and processing time. The dynamic range D_R was calculated using (79).

For a given PN of length L, Figure 20 indicates an increase in D_R for increasing γ/L with local maxima occuring at integer multiples of γ/L. $\gamma/L = 2$ seems to be a particularly critical point for the dynamic range. For small L, increasing the slide factor beyond $2L$ provides only a small improvement in the dynamic range. However, for large L, the increase in dynamic range becomes more substantial for increased γ values.

This is made more evident by Figure 21, which plots dynamic range as a function of L for select γ/L values. The uppermost trace is $D_{R,ideal}$ as given by (80). For all PN lengths, there is a marked improvement in dynamic range when γ/L is increased from 1 to 2. For small L, this appears to bring the dynamic range fairly close to

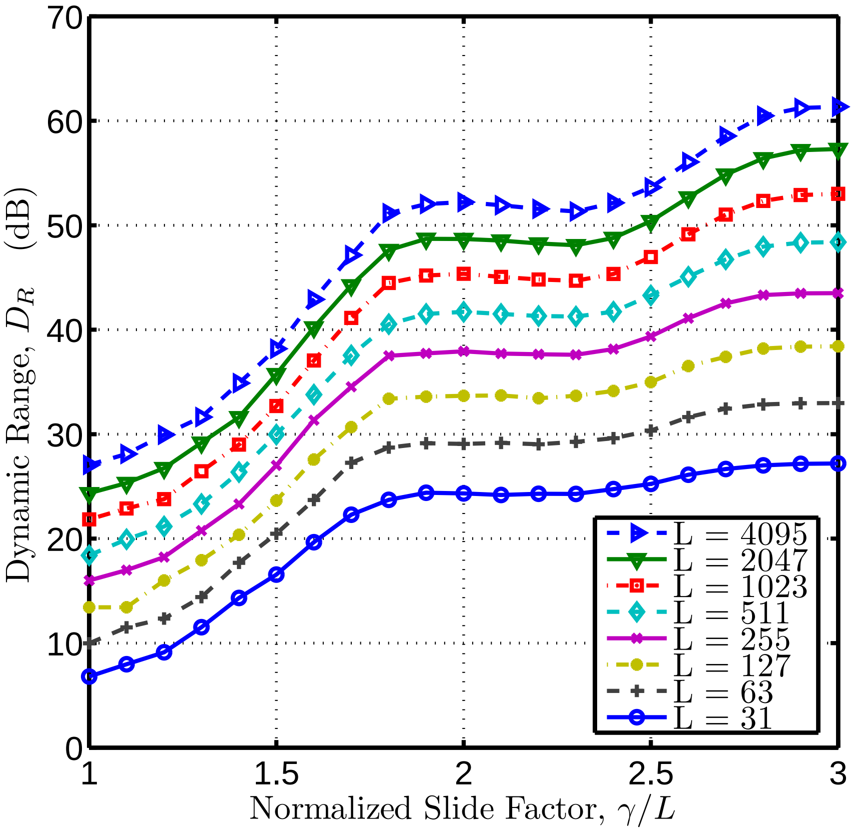

Figure 20: A comparison of the average D_R for sets of four PNs with $L = \{31, 63, 127, 511, 1023, 2047, 4095\}$.

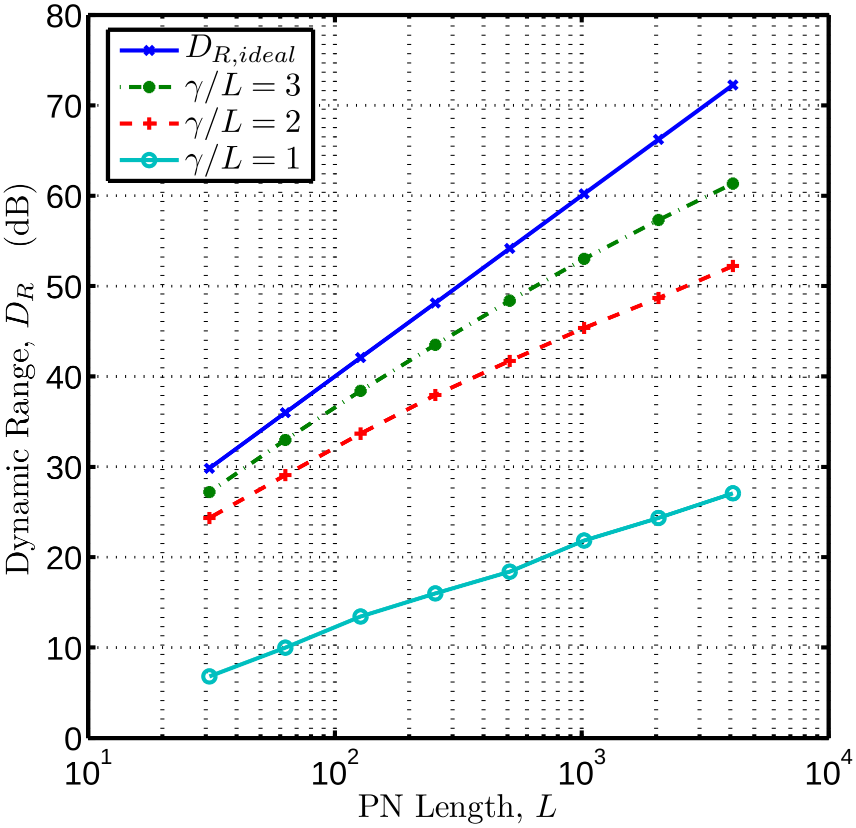

Figure 21: A comparison of $D_{R,ideal}$ to the dynamic range of PNs with $\gamma/L = \{1, 2, 3\}$ for a range of PN lengths L.

$D_{R,ideal}$. However, for large L, the dynamic range will fall well below ideal. Specifically, when $L \leq 63$, using the $\gamma/L = 2$ rule-of-thumb will yield a dynamic range that is approximately $0.8D_{R,ideal}$. However, for $L > 63$ and $\gamma/L = 2$, $D_{R,ideal}$ becomes an increasingly poor approximation for the sliding correlator's dynamic range. When $L = 4095$ and $\gamma/L = 2$, the $D_{R,ideal}$ approximation errs by over 27%.

Using the simulation results, an empirical formula was derived for γ_{min}, which is the minimum slide factor that provides a dynamic range within 20% of ideal. Figure 22 plots the slide factor associated with a particular PN length that produces a dynamic range $D_R = 0.8D_{R,ideal}$. Linear regression analysis on the log-log plot leads to the following empirical equation for γ_{min}.

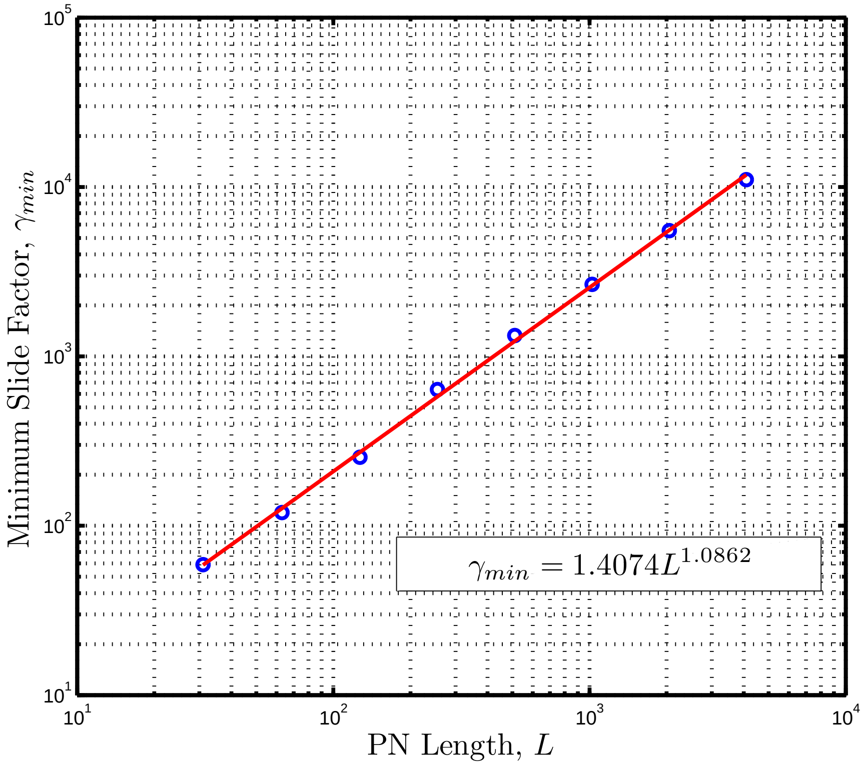

Figure 22: Linear regression performed on the points corresponding to the slide factor for a given PN length that achieves a dynamic range within 20% of ideal.

$$\gamma_{min} = 1.41L^{1.09} \tag{81}$$

For any $\gamma \geq \gamma_{min}$, the dynamic range of the sliding correlator will be in the range $0.8D_{R,ideal} \leq D_R < D_{R,ideal}$ (dB). Thus, we may safely approximate the dynamic range as being equal to the lower bound of $0.8D_{R,ideal}$.

$$D_R \approx 16\log_{10}(L) \text{ (dB) for } \gamma \geq \gamma_{min} \tag{82}$$

It is important to stress that γ_{min} is the minimum slide factor necessary for a given L in order to attain a dynamic range within 20% of ideal. Slide factors greater that γ_{min} will lead to further improvements in dynamic range as D_R asymptotically approaches $D_{R,ideal}$. With the slide factor itself having no hard limit on its maximum value, one might be compelled to set γ arbitrarily high so as to maximize D_R. However, as it shall be shown, the capabilities of a sliding correlator channel sounder depend on only a few key design parameters, one of which is γ. Therefore, while a large slide factor might maximize the channel sounder's dynamic range, it will have adverse effects on other system capabilities. Of course, whether or not this is an issue depends wholly on what one is attempting to measure.

3.3.5 Time-Dilated Autocorrelation Approximation

With careful selection of γ, the output of a sliding correlator will be a time-dilated approximation to the PN autocorrelation. The previous section focused on minimizing the distortion signal to maximize the dynamic range. This led to an empirical formula for the minimum slide factor γ_{min} that would achieve a dynamic range close to $D_{R,ideal}$ with the belief that, by maximizing the dynamic range, the sliding correlator's time-dilated autocorrelation would become a satisfying approximation to $C_x(\tau)$. Let us now assess the validity of our approximation.

Before filtering, the sliding correlator product $p(\tau)$ is the superposition of two signals: $q_c(\tau)$, which is the time-dilated PN autocorrelation, and $q_d(\tau)$, which is the unwanted distortion. Let us set $\gamma = \gamma_{min}$ and filter $p(\tau)$ with an ideal rectangular low-pass filter $H(\tau)$ that has a cut-off frequency $|f_c/\gamma|$. The filtered output of the sliding correlator should approximate a time-dilated PN autocorrelation.

$$C_{x,sc}(\tau) = p(\tau) \otimes H(\tau) \tag{83}$$

Substituting (75) and distributing the convolution operator, we find

$$C_{x,sc}(\tau) = q_c(\tau) \otimes H(\tau) + q_d(\tau) \otimes H(\tau) \tag{84}$$

Recall that $H(\tau)$ was constructed to pass the main lobe of the time-dilated autocorrelation. This main lobe contains 90% of the power in $q_c(\tau)$ [9]. Therefore, we may feel compelled to make the following approximation:

$$q_c(\tau) \otimes H(\tau) \approx q_c(\tau) \tag{85}$$

Additionally, we selected γ in concert with L to minimize the distortion signal and maximize the dynamic range. Thus, we may feel compelled to make one additional approximation:

$$q_d(\tau) \otimes H(\tau) \approx 0 \tag{86}$$

Using these approximations as well as the relationship defined in (77), we find that (83) simplifies to

$$C_{x,sc}(\tau) \approx C_x\left(\frac{\tau}{\gamma}\right) \tag{87}$$

Figure 23 examines the approximation made in (87). Excepting for a 10% decrease in peak amplitude, the traces are nearly identical, indicating that the approximation

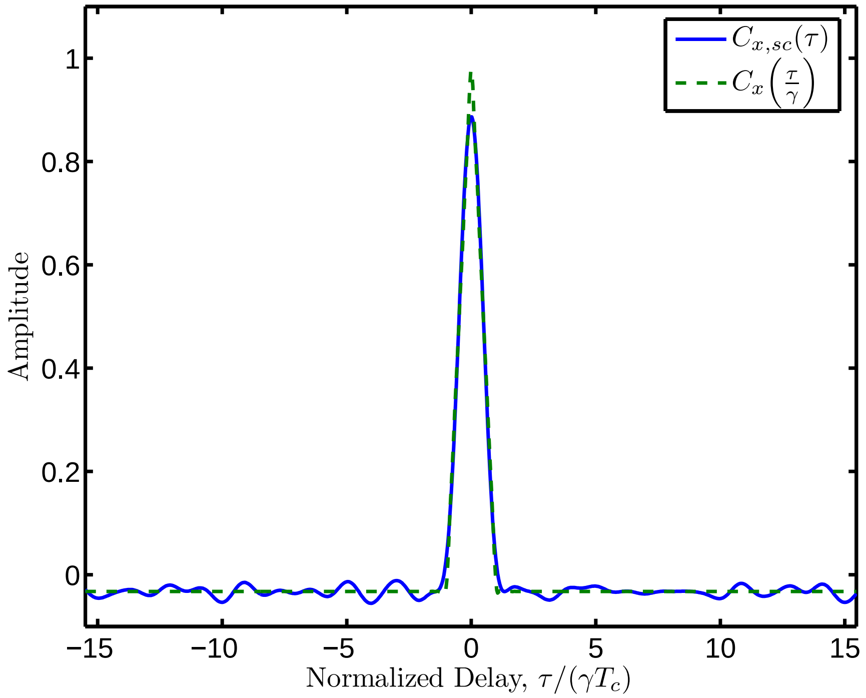

Figure 23: A comparison of the sliding correlator output, $C_{x,sc}(\tau)$, versus a time-dilated version of the PN autocorrelation given by $C_x\left(\frac{\tau}{\gamma}\right)$.

is valid. Therefore, with careful selection of γ relative to L, the output of a sliding correlator will approximate a time-dilated PN autocorrelation.

3.4 Swept Time-Delay Channel Sounding

Let us now consider the CIR of a fixed static wireless channel as measured by a sliding correlator channel sounder. We will assume the actual CIR, $\tilde{H}(\tau)$, fits the tapped-delay line model described by Equation (66). Suppose the transmitted signal $x(t)$ is a PN of length L with a chip rate f_c as described in (53). At the receiver, the received signal $\tilde{y}(t)$ is processed via sliding correlation; that is, it is multiplied by $x'(t)$, which is a PN derived from the same m-sequence as $x(t)$ but with a chip rate f'_c where $f'_c < f_c$. Let us choose f_c and f'_c such that $\gamma = \gamma_{min}$ and filter the output of the sliding correlator with the ideal low-pass filter $H(\tau)$ described by $\tilde{h}(f)$ in (78). Analagous to the sliding correlator's time-dilated autocorrelation described in (87), we expect that the filtered output of a sliding correlator channel sounder will approximate a time-dilated cross-correlation. Denoting the filtered output as $C_{x\tilde{y},sc}(\tau)$, we expect that

$$C_{x\tilde{y},sc}(\tau) \approx C_{x\tilde{y}}\left(\frac{\tau}{\gamma}\right) \tag{88}$$

Equation (88) implies that $C_{x\tilde{y},sc}(\tau)$ is the same band-limited CIR as described by $C_{x\tilde{y}}(\tau)$, albeit time-dilated. This is a powerful statement, so let us examine it more carefully. Substituting (68) for $C_{x\tilde{y}}(\tau)$, we have

$$C_{x\tilde{y},sc}(\tau) \approx \sum_{i=1}^{N} \tilde{\alpha}_i C_x\left(\frac{\tau}{\gamma} - \tau_i\right) \tag{89}$$

Rearranging terms and making use of (87) yields

$$C_{x\tilde{y},sc}(\tau) = \sum_{i=1}^{N} \tilde{\alpha}_i C_{x,sc}(\tau - \gamma\tau_i) \tag{90}$$

Note that although (88) was an approximation, (90) is exact. Substituting (83) for $C_{x,sc}(\tau)$, we arrive at an exact equation for $C_{x\tilde{y},sc}(\tau)$.

$$C_{x\tilde{y},sc}(\tau) = \sum_{i=1}^{N} \tilde{\alpha}_i [p(\tau - \gamma\tau_i) \otimes H(\tau)] \tag{91}$$

Figure 24 compares $C_{x\tilde{y},sc}(\tau)$ as approximated in Equation (88) with the exact formulation described by Equation (91). The nearly identical shape of the traces leads us to conclude that the approximation for $C_{x\tilde{y},sc}(\tau)$ made in (88) is valid. Therefore, by reversing the time-dilation and scaling the signal, we may "undo" the effects of the sliding correlator and obtain a close approximation to the $\tilde{H}_{BL}(\tau)$ described in Equation (69).

$$\tilde{H}_{BL}(\tau) \approx \frac{1}{V_0^2} C_{x\tilde{y},sc}(\gamma\tau) \tag{92}$$

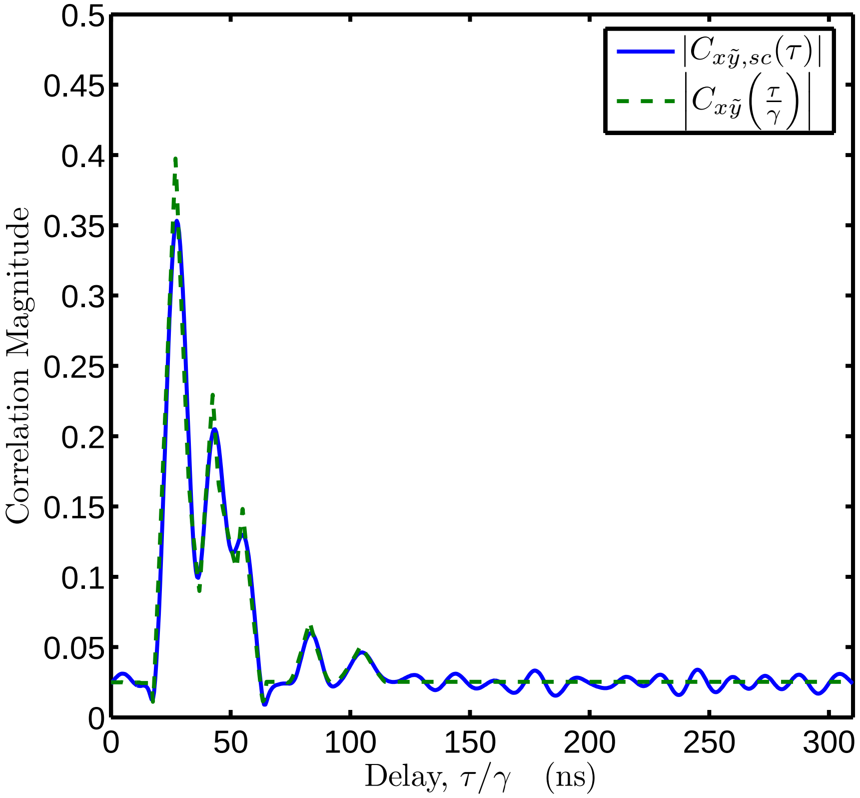

Figure 24: A comparison of the sliding correlator channel sounder's output, $C_{x\tilde{y},sc}(\tau)$, versus a time-dilated version of the wireless channel cross-correlation given by $C_{x\tilde{y}}\left(\frac{\tau}{\gamma}\right)$ for an arbitrary $\tilde{H}(\tau)$.

Table 1: Summary of Channel Sounder Design Equations

Capability	Equation	Dependencies
Max Doppler Resolution	$f_{D,max} = \frac{f_c}{2\gamma L}$	f_c, γ, L
Processing Gain	$G_p = 10\log_{10}(\gamma)$ (dB)	γ
Dynamic Range	$D_R \approx 16\log_{10}(L)$	$\gamma \geq 1.41L^{1.09}$, L
Temporal Resolution	$T_{res} = \frac{1}{f_c}$	f_c
Max Multipath Delay	$\tau_{max} = \frac{L}{f_c}$	f_c, L
Max Path Length	$d_{max} = c\frac{L}{f_c}$	f_c, L

Equation (92) is therefore the approximation to the band-limited CIR that one would obtain if measuring the wireless channel using a sliding correlator channel sounder.

3.5 Channel Sounder Capabilities

The fidelity of the band-limited CIR produced by the sliding correlator channel sounder is dependent on the system capabilities, which are themselves dependent on just three parameters: the transmitter PN chip rate f_c, the PN length L, and the slide factor γ. Table 1 summarizes the channel sounder's capabilities and the parameters that affect them.

3.5.1 Maximum Doppler Resolution

The maximum Doppler resolution is the largest Doppler frequency that can be measured with the sliding correlator channel sounder without aliasing. The channel sounder records a snapshot of the channel impulse response, effectively sampling the wireless channel in time. A snapshot of the CIR is recorded once every $T_{pn,sc}$ seconds, as defined by (93).

$$T_{pn,sc} = \gamma\frac{L}{f_c} \tag{93}$$

Therefore, the CIR sampling rate, $R_{pn,sc}$, is the reciprocal of $T_{pn,sc}$:

$$R_{pn,sc} = \frac{f_c}{\gamma L} \tag{94}$$

According to Shannon's sampling theorem, the maximum non-aliased frequency of the sampled time-varying channel will be one-half of the sampling rate, $R_{pn,sc}$ [47]. This maximum non-aliased frequency is the maximum Doppler resolution, $f_{D,max}$.

$$f_{D,max} = \frac{f_c}{2\gamma L} \tag{95}$$

3.5.2 Processing Gain

The processing gain is defined as the ratio of the SNR after a process to the SNR before the process [9]. Thus, in dB, proccessing gain, G_p, is

$$G_p = 10\log_{10}\left(\frac{SNR_{out}}{SNR_{in}}\right) \text{ (dB)} \tag{96}$$

Processing gain acts to spread the power spectrum of unwanted noise and interferents. Consider a DC offset that is the complex baseband equivalent of a continuous wave interferent at the system's RF carrier. Multiplication with the receiver PN, $x'(t)$, will spread the interferent's power spectral density across a complex baseband bandwidth of approximately f'_c. Filtering with the ideal low-pass filter will block the interferent's spread spectrum at frequencies above f_c/γ such that only $100 \times (f_c/\gamma)/f'_c\%$ of the interferent's power will remain. Assuming $f'_c \approx f_c$, the interferent's power will be reduced by a factor of γ. Thus, the linear processing gain for a sliding correlator is simply γ, which in dB is

$$G_p = 10\log_{10}(\gamma) \text{ (dB)} \tag{97}$$

Note that (97) differs from a DSSS system's processing gain, which may be approximated by $10\log_{10}(L)$ [9]. This is the result of using a sliding correlator receiver as opposed to a true correlator receiver.

3.5.3 Dynamic Range

The dynamic range of a sliding correlator was discussed in detail in Section 3.3.4. Here, we will simply summarize the conclusions. For a sliding correlator system, the ideal dynamic range, $D_{R,ideal}$, in dB is given by

$$D_{R,ideal} = 20\log_{10}(L) \text{ (dB)}$$

It was determined that the realized dynamic range was a function of both the slide factor γ and the PN length L. $D_{R,ideal}$ represents an upper bound on the dynamic range. A corresponding lower bound of $0.8D_{R,ideal}$ was established through an empirical formula for γ_{min}, which was the minimum slide factor for a PN of length L.

$$\gamma_{min} = 1.41L^{1.09}$$

By selecting $\gamma \geq \gamma_{min}$, the realized dynamic range is guaranteed to be in the range $0.8D_{R,ideal} \leq D_R < D_{R,ideal}$ (dB). Therefore, we can approximate the dynamic range according to this lower bound.

$$D_R \approx 16\log_{10}(L) \text{ dB for } \gamma \geq \gamma_{min}$$

3.5.4 Temporal Resolution

The temporal resolution defines how precisely one may resolve the delay of a given multipath component. The temporal resolution is inversely proportional to the bandwidth of the transmitted signal; the more impulse-like the the transmitted signal, the finer the resolution of the measured channel impulse response. For a sliding correlator channel sounder, the temporal resolution T_{res} is estimated as

$$T_{res} = \frac{1}{f_c} \tag{98}$$

Equation (98) represents an upper bound on the temporal resolution, as finer resolution may be acheived through careful post-processing of the measurements.

3.5.5 Maximum Resolvable Multipath Delay

The periodicity of the sliding correlator's time-dilated autocorrelation, $q_c(\tau)$, places an upper bound on the maximum resolvable delay, τ_{max}.

$$\tau_{max} = \frac{L}{f_c} \tag{99}$$

Note that τ_{max} is equal to one period of the transmitted PN. Mutiplying this maximum delay by the free-space propagation velocity, c, yields the maximum resolvable path length, d_{max}.

$$d_{max} = c\frac{L}{f_c} \tag{100}$$

3.6 Design Methodology

It should be stressed that the most important aspect of designing a sliding correlator channel sounder is knowing precisely what one desires to measure. Long-range outdoor measurements require a system with a large maximum resolvable multipath delay. Wideband channel measurements require an equally wideband transmit signal. Those interested in measuring the Doppler spectrum will want a rather large maximum Doppler resolution, whereas those performing static measurements will have little concern for this capability. Finally, one must decide the minimum processing gain and dynamic range that will yield acceptable performance. These last two system capabilities will be affected by the power output of the transmitter as well as the gain, dynamic range, and noise figure of the receiver.

Re-examining Table 1, we note that only $f_{D,max}$ is adversely affected by increasing γ. This indicates that measuring a time-varying wireless channel requires special consideration to balance the tradeoffs in system performance for the specific scenario. However, for static channels, a logical design process follows from the equations in Table 1. Figure 25 diagrams this design process. For specifying f_c, recall that the chip rate is approximately the baseband bandwidth of the transmit PN.

3.7 Practical Considerations

In Figure 25, the final decision block concerning the realizability of $f_c - f'_c$ represents but one of several practical considerations for system design. Depending on the quality factor of the reference oscillators and the specific choice of f_c and f'_c, minor phase variations between transmitter and receiver can cause major fluctuations in $f_c - f'_c$. This causes deviations in the slide factor that degrade the system's performance. Phase instability poses additional challenges for those seeking absolute delay and phase measurements. The preferred solution for achieving phase stability in channel measurements is to use rubidium or cesium-basd atomic master oscillators, which offer extremely high phase stability but can be prohibitively expensive [2]. A more economical solution is to phase-lock the reference oscillators via a cable, but this hampers the mobility and utility of the system.

The channel sounder's performance will also be affected by the limitations and non-idealities of hardware. Amplifier bandwidth, noise figure, 1 dB compression point, mixer port isolation, and conversion losses will all degrade the theoretical system performance. Of the aforementioned design specifications, the most critical for the sliding correlator channel sounder is high mixer LO-RF isolation. Poor isolation allows a portion of the LO power to leak into the RF port of the mixer, as depicted in Figure 26. This acts as narrowband interference at the carrier frequency that essentially raises the receiver noise floor and degrades the dynamic range. The effects of LO leakage may be mitigated by increasing the slide factor to increase G_p, but this will adversely affect other aspects of the system as evidenced by Table 1.

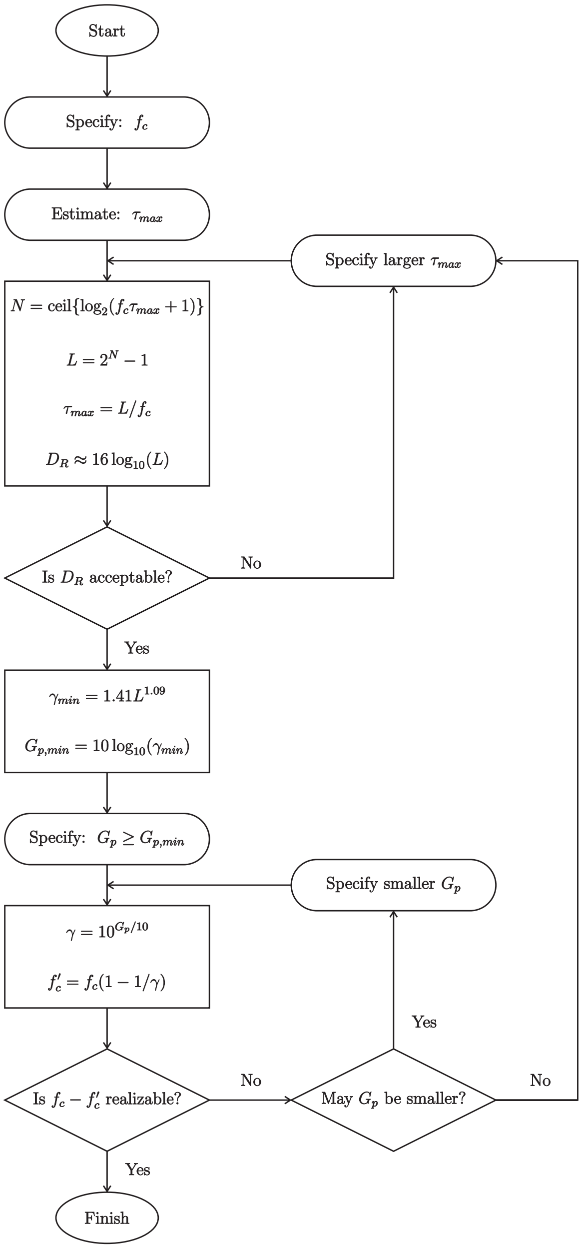

Figure 25: Flowchart describing the design methodology for a sliding correlator channel sounder.

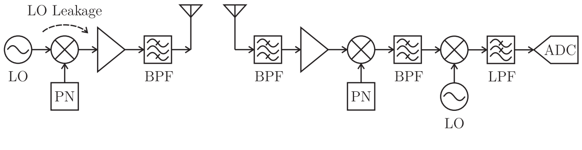

Figure 26: A simplified diagram of the sliding correlator channel sounder. Poor LO-RF isolation allows a portion of the LO power to leak through to the RF port. This acts as a narrowband interferent at the receiver.

.

From a measurement standpoint, it is important to realize that the sliding correlator channel sounder does not take an actual "snapshot" of the wireless channel. Rather, due to its inherent bandwidth compression via temporal dilation, CIRs recorded using the sliding correlator technique are in fact time-averaged measurements. The implications of this time-averaging depend on the rate of temporal variations in the channel. For static and quasi-static channels, it is arguable that, due to the system's inherent robustness to temporal variations, it is redundant to record multiple CIRs in a single location for the purpose of subsequently time-averaging the data. This can significantly reduce the time required for large measurement campaigns. As for time-varying channels, the inherent time-averaging places a restriction on the rate of temporal variations in the channel, such that it must be slowly time-varying relative to the measurement period. Unfortunately, no precise definition can exist for the duration of the measurement period, as it is approximately equal to the time-dilated delay of the last arriving multipath component. However, assuming appropriate selection of τ_{max} according to (99), a prudent restriction for time-varying channel measurements is that the channel must be quasi-static relative to the time-dilated autocorrelation period, $T_{pn,sc}$, as defined in Equation (93). This guideline will also reduce the likelihood of aliasing for Doppler measurements.

CHAPTER IV

SLIDING CORRELATOR CHANNEL SOUNDER: IMPLEMENTATION

An ultra-wideband sliding correlator channel sounder was constructed for performing static UWB channel measurements at 4.1 GHz. The system featured a 17-bit LFSR with a maximum chip rate of 600 MHz. This provided the channel sounder with 34 dB of dynamic range and a temporal resolution of 1.66 ns.

4.1 System Overview

Figure 27 presents a system diagram for the sliding correlator channel sounder. At the transmitter, a 600 MHz oscillator clocks a 17-bit LFSR that produces a PN of $L = 131,071$ chips. The PN is low-pass filtered and modulated up to 4.1 GHz. The RF signal is then band-pass filtered and radiated via an omnidirectional antenna. After propagation through the channel, the received signal is band-pass filtered and amplified by a low-noise amplifier (LNA). The signal is then mixed with a "slow" receiver PN, which has a chip rate of 599.99 MHz. Like the transmitter PN, the receiver PN is also low-pass filtered. With $f_c = 600$ MHz and $f_c' = 599.99$ MHz, the system's slide factor is $\gamma = 60 \times 10^3$.

A spectrum analyzer serves as narrowband receiver for converting the sliding correlator product to an intermediate frequency (IF) of 21.4 MHz. The spectrum analyzer also provides initial filtering and amplification. The IF signal is then sampled by an oscilloscope and stored on a computer for post-processing. Off-line digital signal processing (DSP) is used to downconvert the waveform to baseband and low-pass filter the complex baseband sliding correlator product.

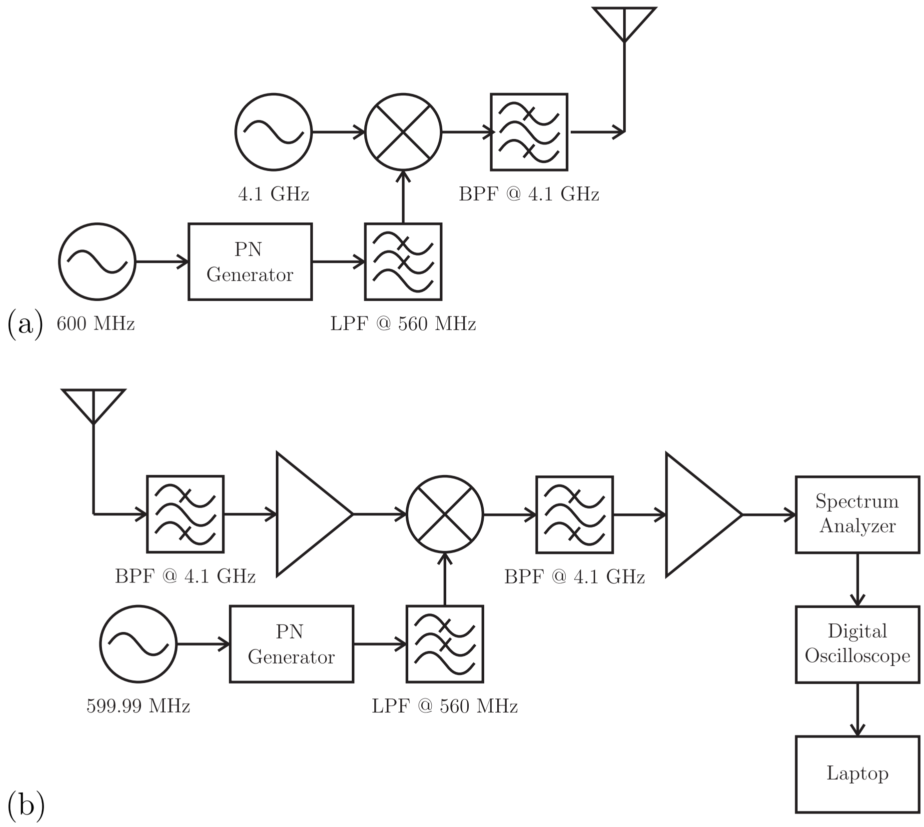

Figure 27: Diagram of the spread spectrum sliding correlator channel sounder: (a) transmiter and (b) receiver.

The following sections examine each of the system blocks in detail.

4.2 PN Generator

The heart of the sliding correlator channel sounder is the PN generator, which is realized as a 17-bit LFSR. To attain a sufficiently fast chip rate for sounding the UWB channel, the propagation delays along the feedback loop of the LFSR are minimized through the use of high-speed Emitter-Coupled Logic (ECL) integrated circuits.

4.2.1 Emitter-Coupled Logic

ECL is generally considered the best choice for high-speed digital design and offers propagation delays on the order of picoseconds [40]. This large bandwidth requires special design consideration so as to minimize reflections caused by improper impedance matching. Other design constraints are imposed by the very nature of ECL, which achieves its short propagation delays by biasing transistors in the forward active region [42]. Because outputs are always sourcing current, power consumption can be rather high. Further, ECL requires all outputs be terminated through a resistance, R_{TT}, to a voltage, $V_{TT} = V_{cc} - 2$, so as to remain in the forward active region during both high and low outputs [43]. Ideally, R_{TT} should match the trace and ouput impedance of the device, both of which are typically 50 Ω. The termination voltage, V_{TT}, acts as a current sink for the ECL outputs. For $V_{cc} = 5$ V, a 3 V current sink may be designed using an op-amp and a PNP transistor, as seen in Figure 28. The op-amp, configured as a voltage follower, applies 2.27 V to the base of the transistors. Current flowing from the ECL outputs into the emitter will forward bias the transistor, thereby setting V_{BE} to approximately 0.7 V and V_{TT} to approximately 3 V.

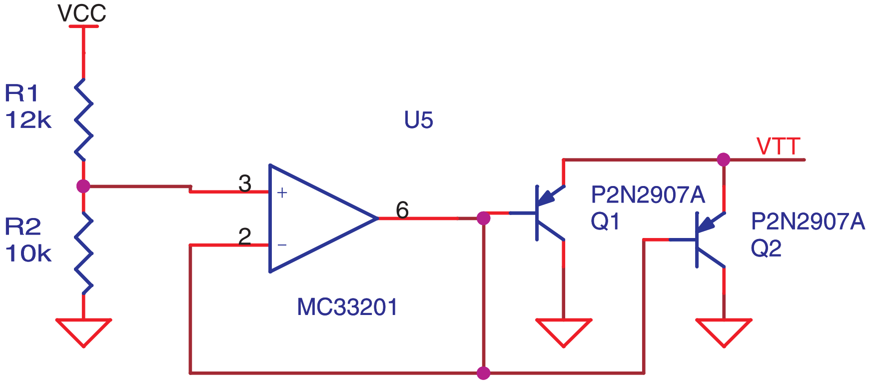

Figure 28: A schematic of the 3 V current sink used for V_{TT}.

4.2.2 Linear Feedback Shift Register

A 17-bit LFSR is implemented using the simple shift register generator (SSRG) architecture and ECL integrated circuits as shown in Figure 29(a). A cascade of two *MC10EP142* 9-bit shift registers provide the backbone for the LFSR [45]. This forms an 18-bit shift register, but, to simplify the design, only 17 of the registers are used for the LFSR. Using the feedback registers, $F_s = \{17, 14\}$, the LFSR produces an m-sequence of $L = 2^{17} - 1 = 131,071$ chips. Modulus 2 addition is perfomed using an *MC10EP08 XOR* gate, whose sum is fed into one of the inputs of an *MC10EP01 OR* gate [41, 44]. The other input of the *OR* gate is tied to a single-pull single-throw (SPST) switch connected to V_{HI}, and the *OR* gate's output is fed to the shift register's input. When the SPST switch is closed, the *OR* gate outputs V_{HI}, effectively filling the shift register with '1's. When the switch is opened, the floating *OR* gate input defaults to V_{LO} and the output of the *OR* gate follows the output of the *XOR* gate. Thus, closing and subsequently opening the switch causes the LFSR to begin generating its m-sequence. Figure 29(b) shows a circuit schematic of the LFSR. Note that for simplicity, the schematic does not include V_{cc}, GND, V_{TT}, or the terminating resistors. For a full schematic, see Appendix A.

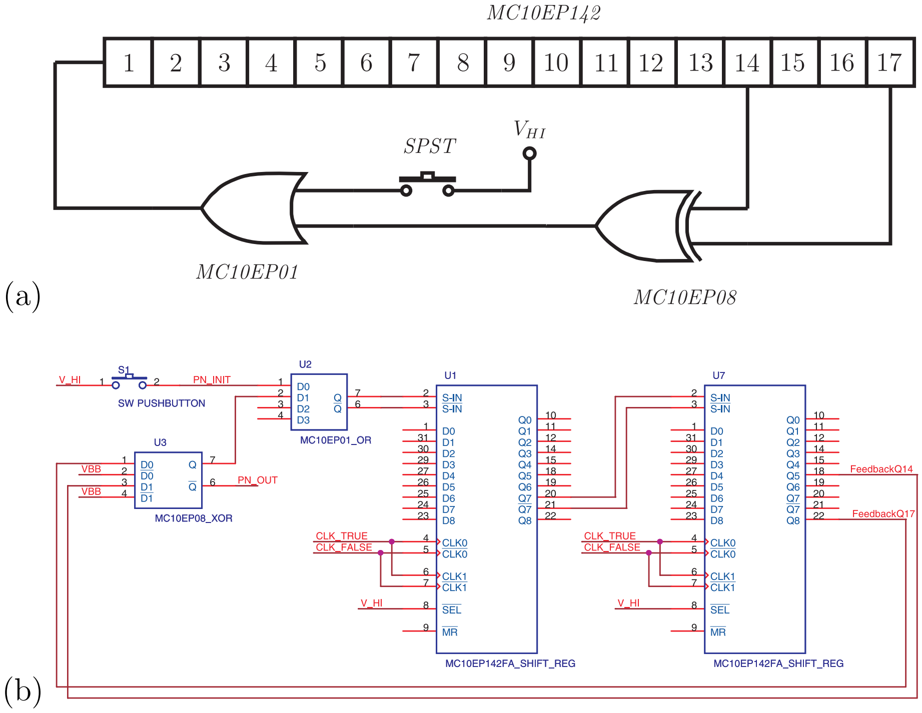

Figure 29: The 17-bit linear feedback shift register that will produce a sequence of lenght $L = 131,071$ chips: (a) diagram of the circuit and (b) a schematic.

4.2.3 PN Generator Clock Converter

To allow for flexibility in selecting a high-speed clock source, the PN generator was designed to accept both square and sinusoidal clocks. The clock inputs are AC-coupled and include a 50 Ω termination for use with typical RF signal sources. The applied clock signal is DC-biased to V_{BB} using a resistive voltage divider. V_{BB} is the typical biasing voltage for ECL and is approximately the mean of V_{LO} and V_{HI} [42]. The biased clock serves as one of the inputs to an *MC10EP16* differential receiver chip [46]. The other input is biased to V_{BB} using an identical resistive voltage divider. This converts the single-ended AC-coupled clock to a differential ECL clock. The *MC10EP16* buffers this differential clock for distribution to the two *MC10EP142* shift registers. Figure 30 shows a schematic of this arrangement. Again, power rails, the terminating voltage, and terminating resistors are ignored to simplify the schematic. The *MC10EP16* differential receiver allows for a maximum input voltage of 2 V_{pp}.

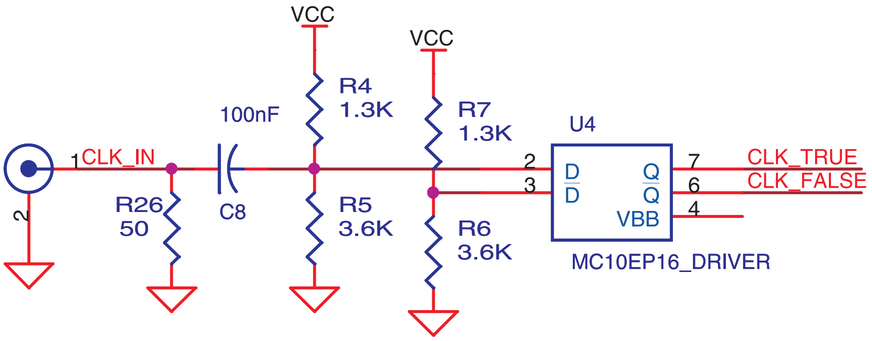

Figure 30: A schematic of the shift register clock converter based around the *MC10EP16* differentical receiver chip. The circuit allows the PN generator to accept sinusoidal clocks from high frequency signal generators.

For a sinusoidal clock source, this corresponds to a maximum input power of 10 dBm. The miminum input power for a sinusoidal clock was experimentally determined to be -10 dBm, which correponds to 1.414 mV$_{pp}$.

4.2.4 PN Output Termination

The ECL-based LFSR requires a 50 Ω termination to $V_{TT} = Vcc - 2$ to maintain proper biasing. However, most RF devices such as amplifiers, mixers, and filters are designed for 50 Ω terminations to GND. Resolving this disparity required a DC path to ground for biasing the ECL's emitter-follower output while also allowing for a 50 Ω AC termination to GND as provided by a typical RF device. When terminated through 50 Ω to V_{TT}, the emitter-follower sources 21.1 mA for V_{HI} and 5.1 mA for V_{LO}. When the ECL output is connected to the parallel combination of a 274 Ω resistor to GND and a large capacitor to a 50 Ω device, the emitter-follower sources 22.8 mA for V_{HI} and 3.8 mA for V_{LO} [24]. These currents are sufficiently similar to the currents sourced by an ECL output terminated through 50 Ω to V_{TT} and, more importantly, they maintain the forward active biasing of the ECL ouput. Figure 31 provides a schematic of the circuit used to connect the PN generator's ECL output to a typical RF device represented by a 50 Ω load to ground.

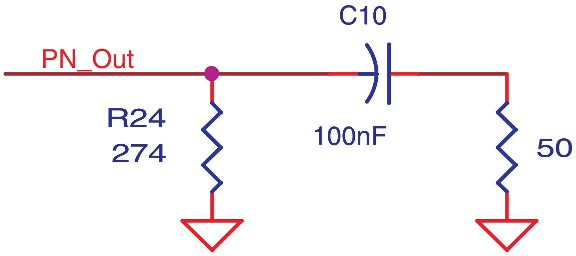

Figure 31: A schematic of the PN output circuit for connecting the ECL's emitter-follower to a 50 Ω RF termination.

4.2.5 Verification of the PN

Figure 32 examines the power spectral density of the output signal with the LFSR clocked at 600 MHz. The characteristic sinc-shaped envelope is visible with nulls occurring at multiples of 600 MHz. Spikes at these nulls indicate clock feed-through. Figure 33 takes a closer look at this power spectral density and reveals the individual spectral components that define the spectrum's envelope. The spectral components have a spacing of approximately 4.583 kHz. This is in good agreement with the theoretical spacing of $f_c/L = 4.578$ kHz for $L = 131,071$ and $f_c = 600$ MHz as given by Equation (63), providing a good indication that the LFSR is operating corrctly and generating the expected PN. Figure 34 shows a photograph of the constructed PN generator.

4.2.6 Low-Pass Filter

A low-pass filter follows the output of the PN generator to suppress the PN's spectral side lobes and clock feed-through, as well as to meet the FCC emissions mask for UWB. The majority of the PN's power is contained within the main spectral lobe, which has a baseband -3 dB bandwidth of $0.88f_c$ [9]. For $f_c = 600$ MHz, the PN's -3 dB bandwidth is 528 MHz. Accordingly, a MiniCircuits *LFCN-400* low-pass filter was selected. The filter has a -3 dB cutoff frequency of 560 MHz and a 30 dB of insertion loss at 650 MHz [28].

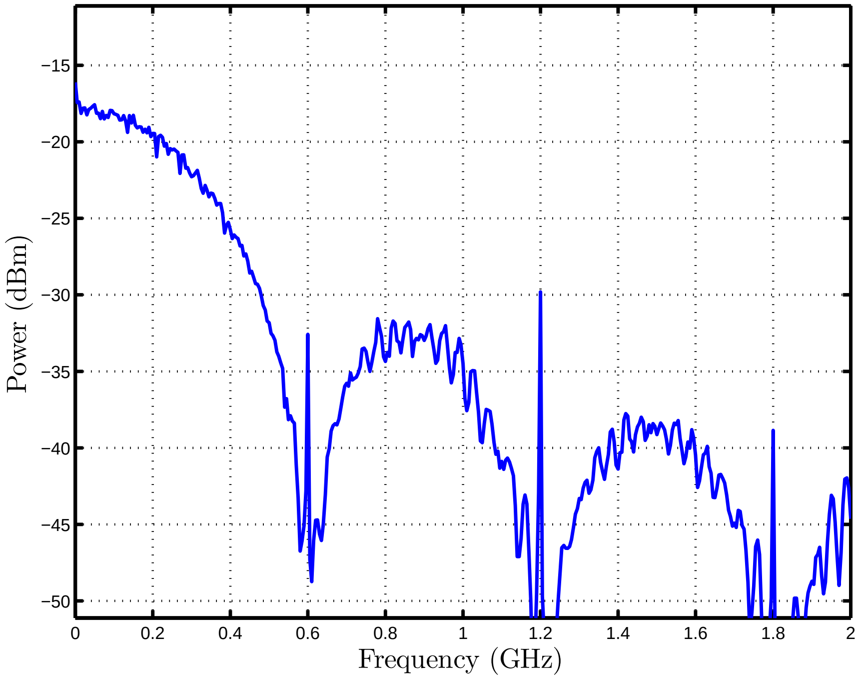

Figure 32: The spectrum of the PN produced by the 17-bit LFSR with a chip rate of $f_c = 600$ MHz. The spectrum had the characteristic sinc-shaped envelope.

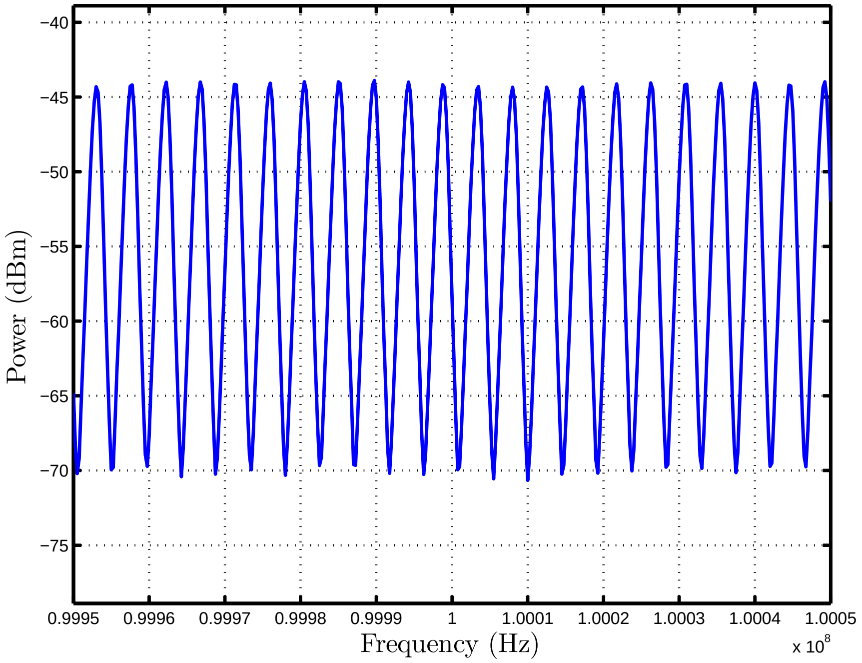

Figure 33: A closer look at the spectrum produced by the 17-bit LFSR with a chip rate of $f_c = 600$ MHz revealed the spectral components that make up the sinc-shaped envelope. The interval between components was 4.583 kHz.

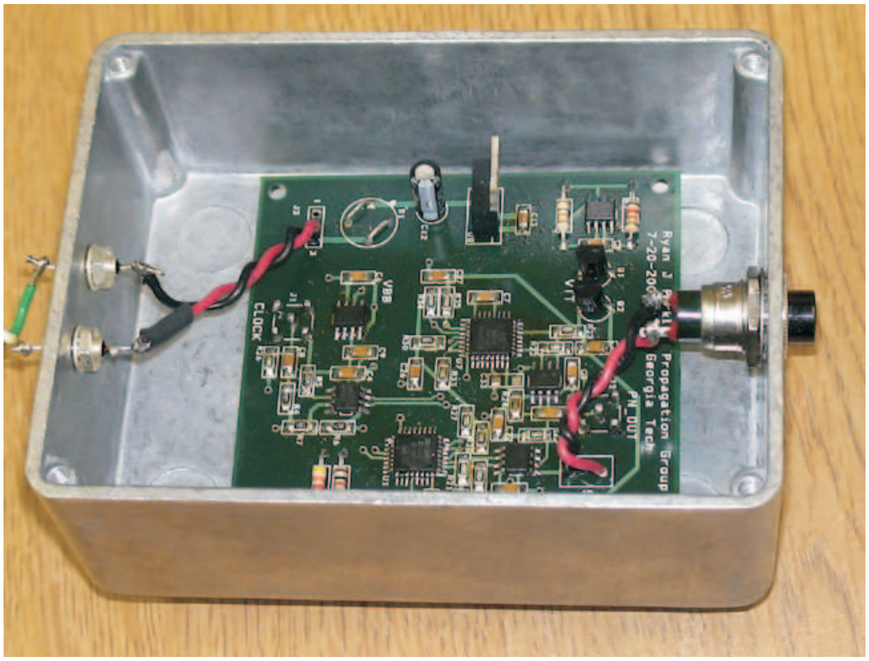

Figure 34: A photo of the 17-bit LFSR-based PN generator designed with ECL. The PN generator produced a sequence length of $L = 131,071$ chips at a maximum chip rate of approximately 600 MHz.

4.3 Antennas

An omnidirectional antenna is used at the transmitter while the receiver uses either an omnidirectional or directional antenna depending on the type of measurement. Two 12 foot cables connect the transmitter and receiver to their respective antennas. For calibration and system validation, these cables are considered as part of the transmitter and receiver.

4.3.1 Omnidirectional Antenna

The ideal omnidirectional antenna for wideband channel sounding is a biconical antenna, which is characterized by a flat frequency response and constant radiation pattern over a wide bandwidth [39]. Unfortunately, neither a biconical antenna nor its monopole equivalent disk-cone were available. Therefore, a wideband omnidirectional antenna was constructed based upon the planar disk monopole as used by Honda et al. to cover the Japanese television band from 90 to 770 MHz [22]. Liang et

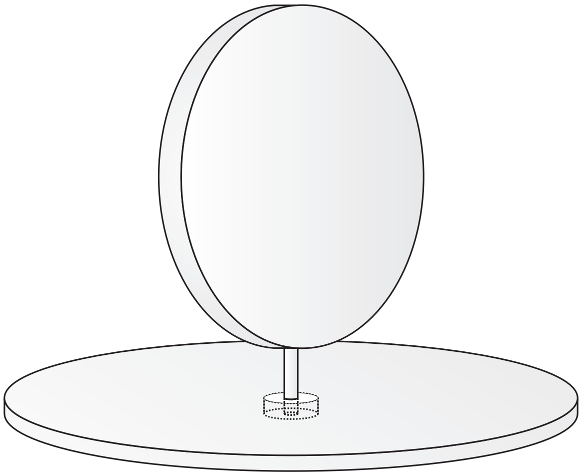

Figure 35: The planar disk monopole antenna features a disk-shaped radiating element above a circular ground plane.

al. constructed a similar planar disk monopole that attained an $|S_{11}| \leq -10$ dB from 2.16 to over 15 GHz with an omnidirectional radiation pattern [25, 26]. Additionally, the phase between two such antennas was found to be linear, indicating a common phase center for all radiating frequencies. Figure 35 depicts the basic structure of the planar disk monopole.

For the constructed antenna, the radiating element was a 30.5 mm diameter, 2 mm thick nickel-clad copper disk. The disc was placed atop a 1.2 mm wire that positioned the radiating element 4.6 mm above a circular ground plane. The ground plane had a diameter of 51 mm and a thickness of 1.4 mm. Figure 36(a) shows the measured $|S_{11}|$ of the antenna. The -10 dB bandwidth of the antenna ranges from 3.15 GHz to over 5.1 GHz. Figure 36(b) shows the measured gain pattern of the antenna, which indicates that at 3.1 GHz, the antenna behaves quite similar to a monopole. As the operating frequency increases, the pattern becomes more oblong due to the rotational asymmetry of the antenna. Between 3.5 GHz and 4.7 GHz, the maximum variation in the antenna pattern across both angles and frequencies is 5 dB. Thus, for the channel sounder's operating band, the constructed antenna is quasi-omnidirectional, and thereby an acceptable approximation to an omnidirectional antenna. Figure 37 shows a picture of the constructed planar disk monopole antenna.

4.3.2 Directional Antenna

A double-ridged horn is used for the wideband directional antenna. Figure 38(a) shows the measured $|S_{11}|$ of the antenna, which indicates an $|S_{11}| \leq -10$ dB from 3.32 GHz to 4.1 GHz. Figure 38(b) shows the measured gain pattern of the antenna. Although the measured return loss is less than ideal, the antenna's gain pattern indicates adequate performance within the band of interest. Between 3.1 GHz and 5.1 GHz, the antenna has a maximum -3 dB beamwidth of approximately 40°. The gain along the main beam ranges from 11.4 dBi at 3.83 GHz to 7.4 dBi at 4.85 GHz. Figure 39 shows a picture of the double-ridged horn.

4.4 RF Components

The most constraining design specification for RF component selection was the large bandwidth of the channel sounder. Components were required to have a flat frequency response from 3.5 to 4.7 GHz with as linear a phase response as possible to minimize pulse distortion.

4.4.1 Mixer

The mixer was required to have a large operating bandwidth to handle the UWB signal as well as high LO-RF isolation to minimize LO leakage. A Mini-Circuits *MCA1-60* wide-band mixer was selected for both the transmitter's and receiver's mixer [27]. The *MCA1-60*'s LO and RF ports have a frequency range of 1.6 to 6 GHz with 2 GHz of bandwidth at the IF port. LO-RF isolation and conversion loss at 4.1 GHz are approximately 33 dB and 6 dB respectively provided an LO power of 7 dBm. As indicated in Figure 27, a 3 dB attenuator between the transmitter's PN generator and its low-pass filter prevent the PN waveform from over-driving the IF port of the transmitter's mixer. No attenuation was necessary at the receiver's IF

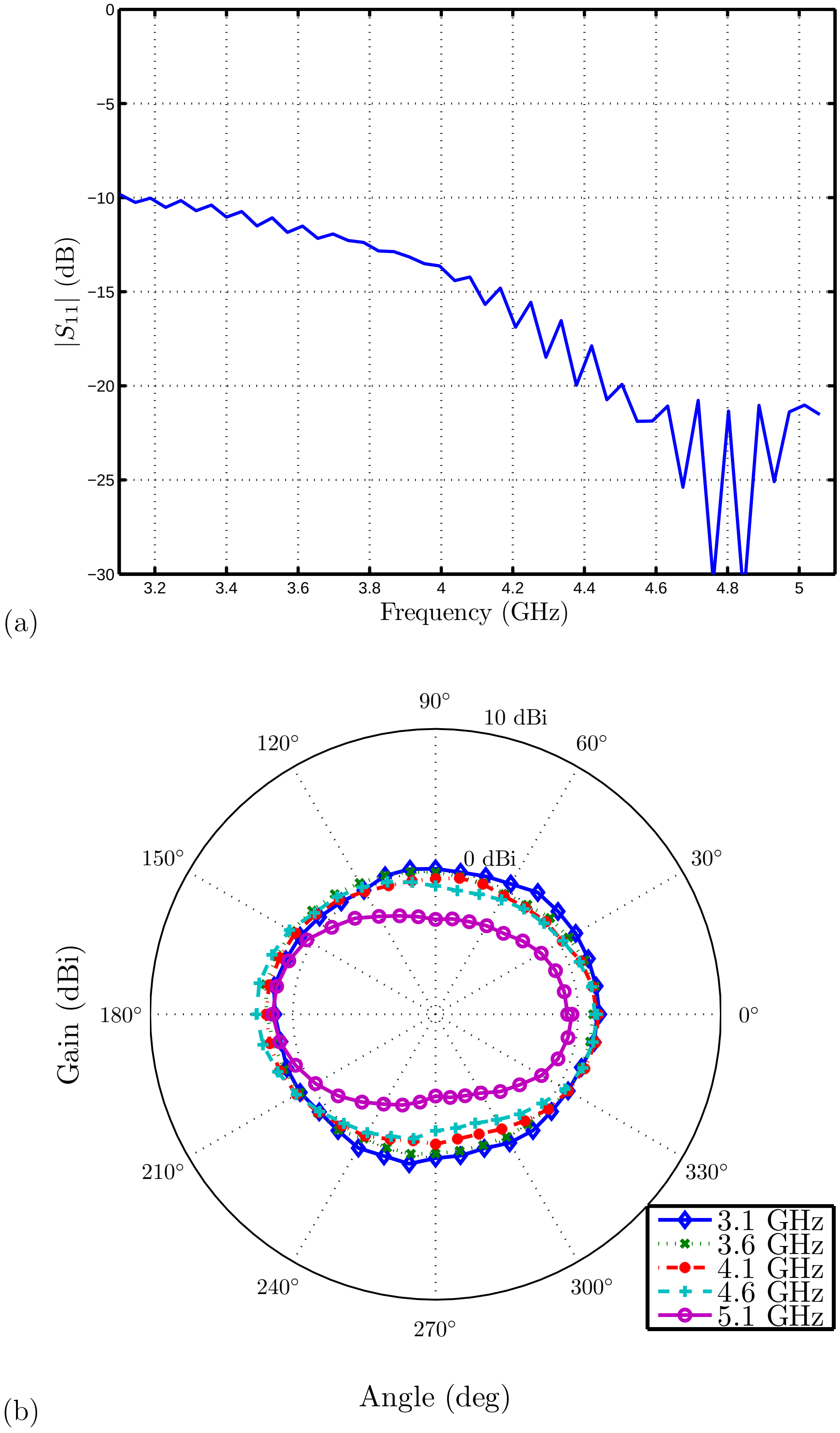

Figure 36: Performance characteristics of the planar disk monopole antenna: (a) $|S_{11}|$ and (b) gain pattern.

Figure 37: A photograph of the planar disk monopole antenna used for omnidirectional measurements.

port.

4.4.2 Band-Pass Filter

Three identical 4.1 GHz band-pass filters are used in the sliding correlator channel sounder. One is located before the transmit antenna; another is located after the receive antenna; the third is placed after the sliding correlator mixer. Each band-pass filter consists of a Mini-Circuits *VLP-54* low-pass filter and *VHP-26* high-pass filter. Cascading these two filters produces a band-pass filter with upper and lower −3 dB cut-off frequencies of 2.6 GHz and 5.4 GHz, respectively [31, 30].

4.4.3 Amplifier

Two Mini-Circuits *ZVE-8G* amplifiers are used in the receiver chain following the two RF band-pass filters. The first amplifier in the chain acts as the receiver's low-noise amplifier (LNA). The second provides additional gain before downconversion to IF. The *ZVE-8G* features 35 dB of gain from 2 to 8 GHz, a P_{1dB} of approximately 31 dBm, and a noise figure of 4 dB [29].

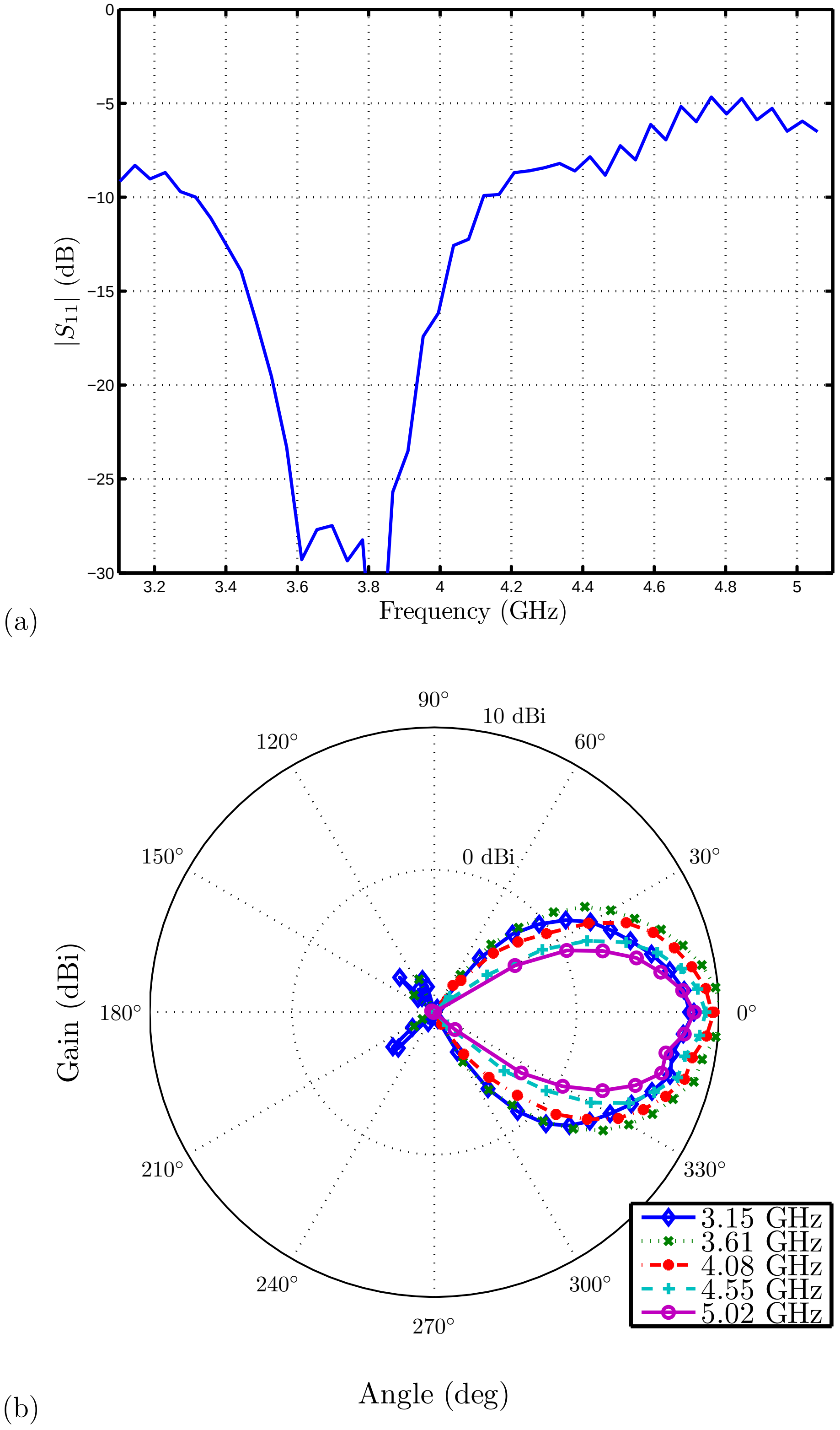

Figure 38: Performance characteristics of the doubled-ridged horn antenna: (a) $|S_{11}|$ and (b) gain pattern.

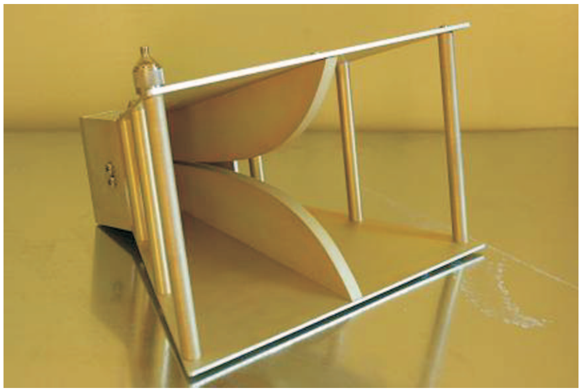

Figure 39: A photograph of the double-ridged horn antenna used for directional measurements.

4.5 IF Sampling

Following the second amplifier in the receiver chain, the signal is fed to an Agilent *E4407B* spectrum analyzer. The spectrum analyzer serves as both a narrowband RF filter and a mixer for converting the RF signal to IF. The spectrum analyzer features a tunable 4-pole Gaussian filter that determines the RF resolution bandwidth and thereby, the bandwidth of the IF signal [1]. The -3 dB bandwidth of this filter was set to 30 kHz, which is 1.5 times the null-to-null RF bandwidth of the time-dilated autocorrelation. After filtering, the spectrum analyzer mixes the RF signal to an IF of 21.4 MHz [1]. The spectrum analyzer's internal variable-gain amplifier is used to amplify the received signal to approximately 40 mV_{pp} prior to digitization by an Agilent *DSC-6000* oscilloscope. The oscilloscope captures 20 ms of the IF waveform at a sampling rate of 50 MS/s. The digitized IF signal is then downloaded onto a laptop for post-processing.

4.6 Post-Processing

Digital signal processing is performed in Mathworks *MATLAB*. The digitized signal is shifted to baseband and iteratively downsampled and low-pass filtered. The final low-pass filter is an approximation to the ideal rectangular filter described in (78) for removing the distortion signal. This last filter is realized by a 500^{th} order low-pass

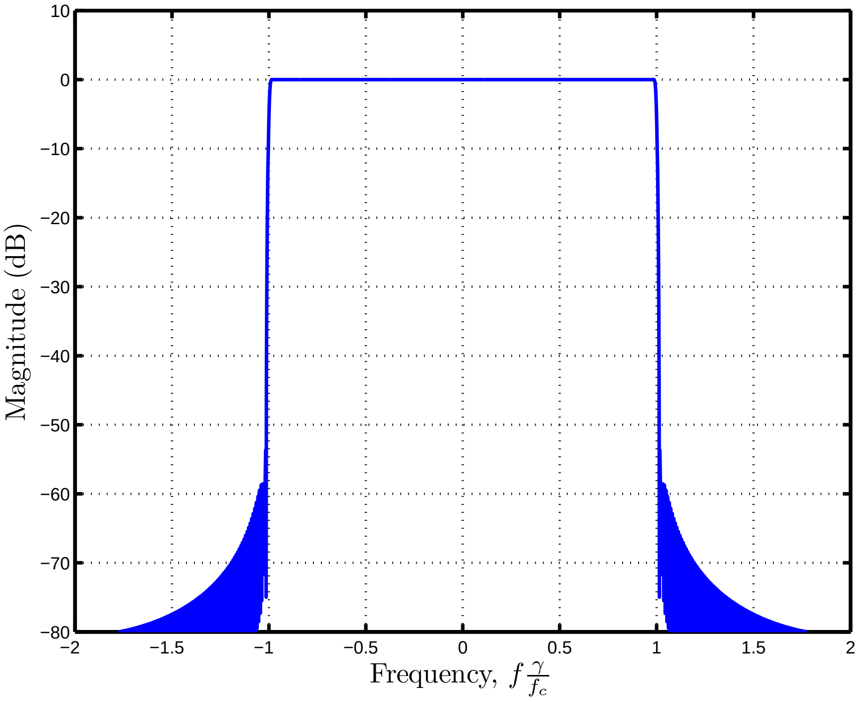

Figure 40: The frequency response of the 500^{th} order low-pass filter used for removing the sliding correlator's distortion signal.

filter generated using *MATLAB*'s *fir1* function. The cut-off frequency corresponds to $f_c - f_c'$, which is 10 kHz. Figure 40 shows the frequency response of the sliding correlator's low-pass filter.

4.7 System Verification

According to the theory developed in Chapter 3, the time-dilated autocorrelation will have a base width of $2\gamma/f_c$ seconds and a period of $L\gamma/f_c$ seconds. For the realized channel sounder with $\gamma = 60 \times 10^3$, $f_c = 600$ MHz, and $L = 131,071$ chips, the time-dilated base width and period should be 2 μs and 13.1 s, respectively. To validate the channel sounder's operation, two sets of measurements were made.

4.7.1 Direct Connection Measurements

For the first set of validation measurements, the antennas were removed from both the transmitter and receiver. The tramitter's output power spectral density was recorded

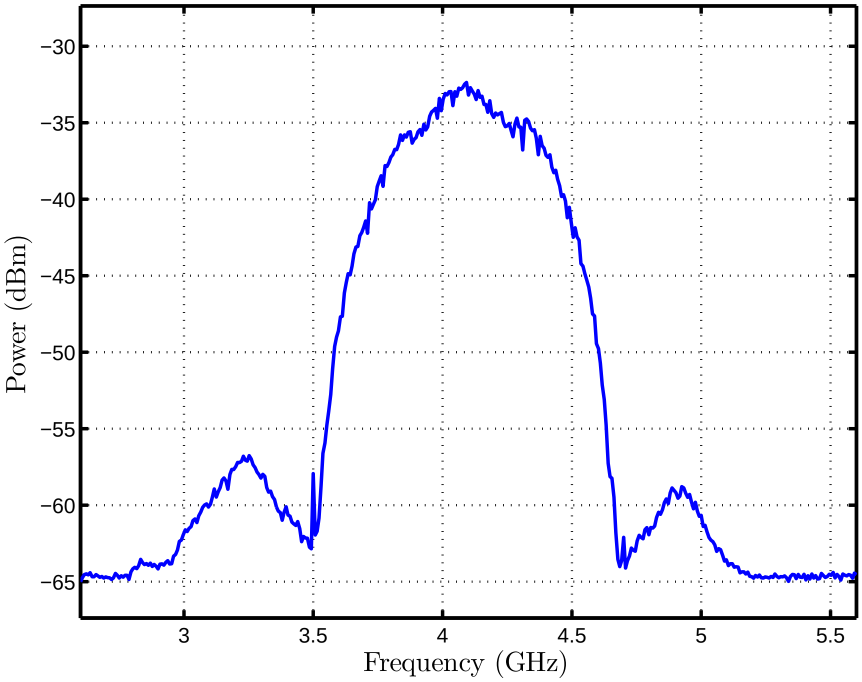

Figure 41: The transmitted signal's power spectral density with a null-to-null bandwidth of 1.2 GHz and a total power of −10.9 dBm.

using a spectrum anaylzer. As shown in Figure 41, the signal had a null-to-null bandwidth of 1.2 GHz and a total power of −10.9 dBm.

Next, the transmitter was connected through a 50 dB attenuator to the receiver. Figure 42 shows several periods of the time-dilated autocorrelation with a period of 13.13 seconds, which agrees well with the expected period of $L\gamma/f_c = 13.11$ seconds. The periodic waveform resembles the PN autocorrelation in Figure 15, excepting for the smaller spikes on either side of the main peak. These spikes are spaced at multiples of 938 ms, which, after temporal compression, corresponds to 15.6 μs of delay or 4.69 km of excess path length for the free-space velocity of propagation. Thus, even if accounting for the slower propagation velocity in the cables, the excess delay implied by the spikes is unreasonable. This indicated that these small spikes were not a result of impedance mismatches within the channel sounder. Regardless, due to the large difference in magnitude between the main peak and smaller spikes, the channel sounder could still be triggered off the main peak. Furthermore, with

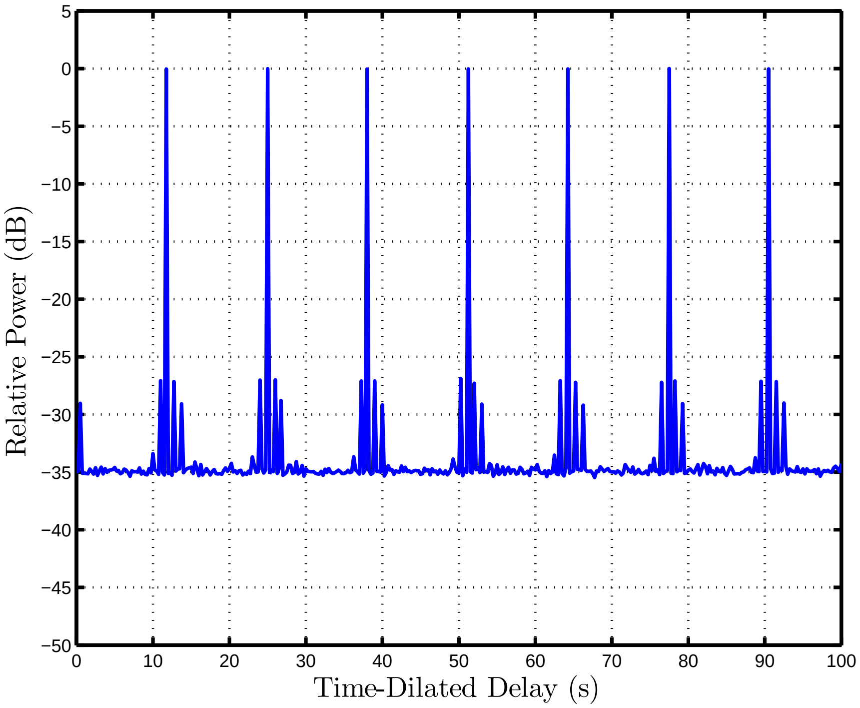

Figure 42: The channel sounder's time-dilated autocorrelation has a period of 13.13 seconds.

their excess delay at multiples of 15.6 μs, these spikes would have no impact on indoor UWB channel measurements, where delay spreads are on the order of tens of nanoseconds [11].

Figure 43 takes a closer look at one of the main peaks in the time-dilated autocorrelation. The -10 dB width of the triangular waveform is 150 μs, which, after temporal compression, corresponds to a width of 2.5 ns. This is in good agreement with the theoretical -10 dB width of 2.27 ns. The peak located -18 dB below and 182 μs after the main peak is attributed to impedance mismatches within the channel sounder.

From these measurements, it was concluded that the channel sounder was correctly time-dilating the autocorrelation by a factor of $\gamma = 60 \times 10^3$. The next set of measurements assessed any potential antenna effects.

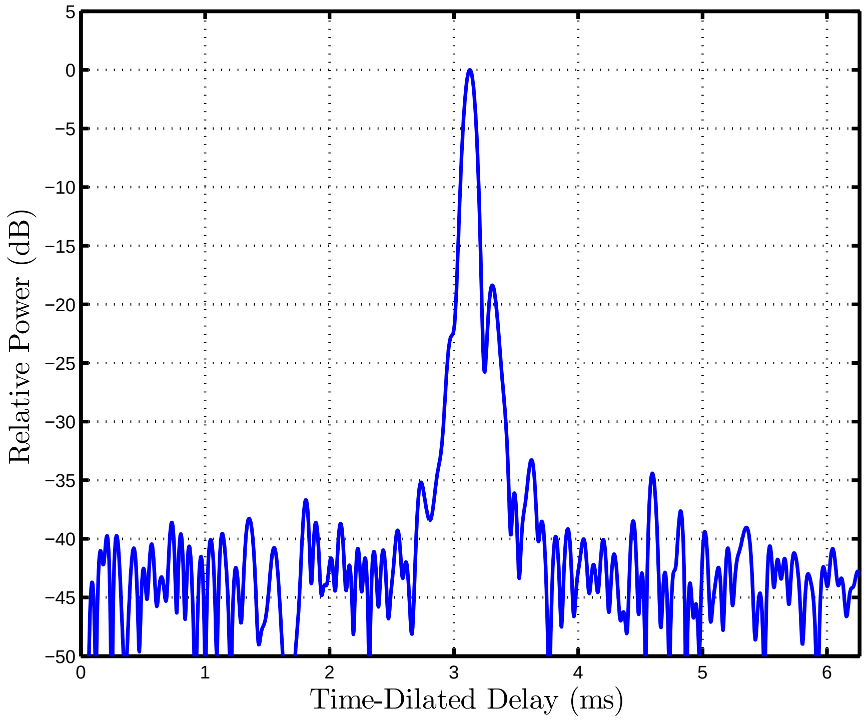

Figure 43: The triangular time-dilated autocorrelation has a -10 dB width of 150 μs.

4.7.2 One Meter Antenna Measurements

The system was moved to an open area far from scatterers. An omnidirectional antenna was used at the transmitter, and the time-dilated autocorrelation was measured at a distance of one meter using both the directional and omnidirectional antenna. Figure 44 compares the two measurements. Both measurements show the same -10 dB base width of approximately 150 μs. Note that the directional antenna exhibited approximately 8 dB of gain compared to the omnidirectional antenna. This is in good agreement with the measured antenna gains. The peak occurring 3.54 ms after the main peak was attributed to a multipath component whose angle-of-arrival was beyond the directional antenna's main beam. The geometry of the measurement environment confirmed this hypothesis. Thus, this multipath component appeared in the omnidirectional measurement but not the directional measurement. Excepting for this disparity, the similarity of the traces in Figure 43 and Figure 44 lent confidence

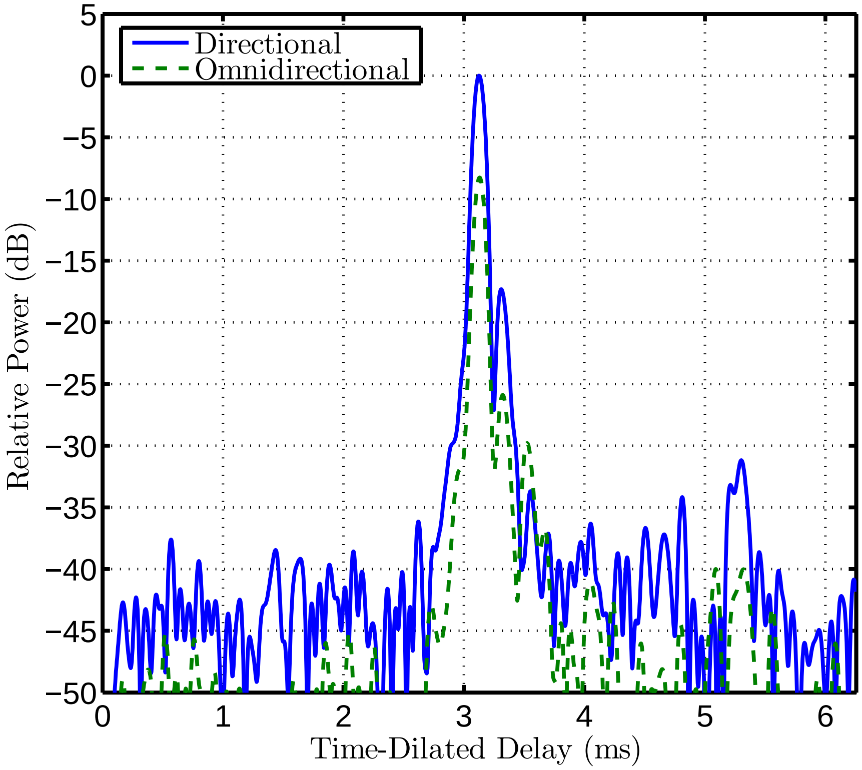

Figure 44: A comparison of the CIR measured one meter from the transmitter as recorded using a directional and omnidirectional antenna.

to the assumption that neither antenna was distorting the transmit or receive signals.

4.8 Calibration

System calibration provides information on the linear operating range of the receiver as well as the necessary scaling factor for relating received voltage to the CIR. Calibration was carried out as follows:

1. The transmit and receive antennas were disconnected and replaced by a 20 dB fixed attenuator connected to a 70 dB step attenatuator.

2. The step attenuator was adjusted to provide between 30 to 90 dB of total attenuation in 10 dB steps. A time-dilated autocorrelation measurement was performed at each attenuation level.

3. A plot of maximum measured power versus received power showed a linear relationship with a constant offset.

4. A scalar voltage correction factor was calculated as the mean of the square root of maximum measured power divided by received power. Thereby, maximum measured power would correspond to received power.

Maximum measured power was the peak power in the time-dilated autocorrelation measurement. Received power was calculated as the transmitter output power normalized by the total attenuation. Figure 45 shows a plot of maximum measured power versus received power after applying the scalar voltage correction factor to the time-dilated autocorrelation. The one-to-one linearity of the trace indicated that the system was operating in the linear regime for received power in the range of -100.9 dBm to -40.9 dBm. Thus, normalization of the calibrated time-dilated autocorrelation by the transmitter's output power would yield the CIR.

System calibration was performed before and after each measurement session. Comparison of pre-measurement and post-measurement correction factors ensured that the system was stable during the entire measurement session. The arithmetic mean of the pre- and post-measurement correction factors was used as the entire session's voltage correction factor, which was applied to the measurement during post-processing.

4.9 Summary of System Capabilities

With a chip rate of 600 MHz, the channel sounder attained a temporal resolution of 1.66 ns and a null-to-null bandwidth of 1.2 GHz. The UWB -10 dB bandwidth was 800 MHz, and the transmitter's total output power was -10.9 dBm. The channel sounder's 17-bit LFSR produced an m-sequence of 131,017 chips, leading to a maximum measurable multipath delay of 218 μs. However, the signal spikes observed in the sliding correlator's time-dilated autocorrelation as well as the finite capture window

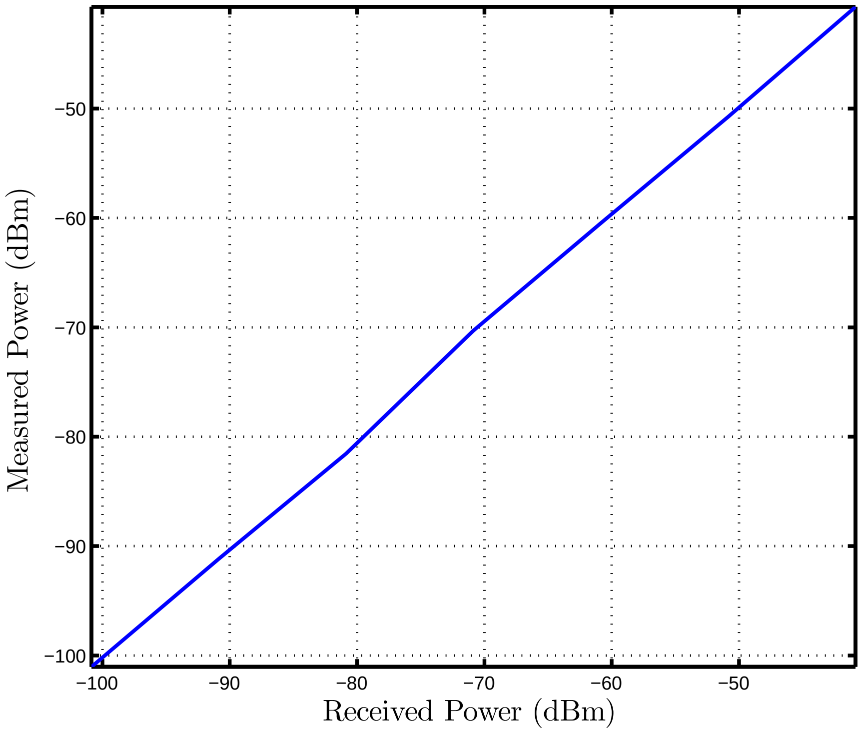

Figure 45: After calibration, the measured power shows a one-to-one relationship with received power.

of the digital oscilloscope restricted the maximum multipath delay to approximately 333 ns, which corresponds to a maximum excess path length of 100 meters.

The system achieved a dynamic range of 34 dB, and it was concluded that the dynamic range was limited by the LO-RF isolation at both the transmitter's and receiver's mixers as well as conversion loss during the sliding correlation operation. The mixer had 33 dB of LO-RF isolation and 6 dB of conversion loss. For an LO power of 7 dBm and an IF power of 2 dBm (5 dBm produced by the PN generator minus 3 dB of attenuation to prevent overdriving the mixer), the leaked LO power at the transmitter's mixer would lead to a signal-to-interference ratio of 21 dB. At the receiver, this narrowband interference would be spread in frequency due to multiplication with the receiver's PN. However, the processing gain inherent to the sliding correlation was offset by significant signal conversion loss. The signal power after multiplication was found to be 20 dB below the signal's power prior to multiplication. Accounting

Table 2: UWB Channel Sounder Capabilities

System Capability	Realized Performance
Max Doppler Resolution $f_{D,max}$	38 mHz
Processing Gain G_p	13 dB
Dynamic Range D_R	34 dB
Temporal Resolution T_{res}	1.66 ns
Max Multipath Delay τ_{max}	333 ns
Max Path Length d_{max}	100 m

for the 33 dB of LO-RF isolation at the receiver's mixer, the net improvement in signal-to-interference-ratio following the mixer would be 13 dB. Thus, the channel sounder had 13 dB of processing gain and a maximum attainable dynamic range of 34 dB regardless of its slide factor.

Due to the degraded dynamic range resulting from the mixers' LO-RF isolation and conversion losses, it was concluded that γ could be set to a value less than γ_{min} if it did not further degrade the system's dynamic range. As evidenced by Figures 43 and 44, a slide factor of $\gamma = 60 \times 10^3$ provided acceptable levels of performance and approximately 34 dB of dynamic range. This smaller slide factor also significantly reduced the time-dilated autocorrelation period. For $\gamma = \gamma_{min}$, the period was 116 seconds; for $\gamma = 60 \times 10^3$, it was 13 seconds, leading to a maximum Doppler resolution of 38 mHz. This is extremely small, but it must be remembered that the system was designed for static measurements. Thus, little emphasis was placed upon Doppler resolution. Table 2 summarizes the realized channel sounder's capabilities.

Finally, it is important to recognize the limitations of the constructed channel sounder. The system was incapable of measuring *absolute* delay, as there was no synchronization between transmitter and receiver PN generators. Therefore, CIR measurements present *excess* delay, which is the delay relative to the first arriving multipath component. It should also be noted that the measured phase represents a relative and, unfortunately, time-varying phase. During system calibration before and after each day's measurements, phase variations were observed on the order of ±30°. This was later attributed to the excessive length of the synchronization cable, which imposed a finite but significant delay on the time-varying phase between transmitter and receiver.

CHAPTER V

MEASUREMENTS

A measurement campaign was devised to investigate the delay and angular spreads of the UWB wireless channel. Delay spreads were calculated from delay spectra, whereas angular spreads were calculated from both azimuthal angle spectra and spatial fading rates along two orthogonal tracks. A dual approach was taken for angular spread to check for consistency between approaches, as it was expected that the gain pattern of the directional horn used for measuring the angle spectrum would slightly distort the measured angle spectrum.

5.1 Setup

The channel sounder described in Chapter 4 was used for measuring the CIR of a static indoor UWB channel. The transmitter consisted of a 17-bit LFSR-based PN generator with a chip rate of 600 MHz that modulated a 4.1 GHz RF carrier. This produced a -10.9 dBm signal with 1.2 GHz for sounding a portion of the indoor UWB spectrum ranging from 3.5 to 4.7 GHz. The DSSS waveform was radiated by an omnidirectional antenna that was mounted atop a 180 centimeter pole made of polyvinyl chloride (PVC). The antenna was positioned approximately 1.5 meters from the nearest wall and 1 meter above the adjacent desks bearing papers, computers, and other common office materials. The transmit antenna was fixed for the entire measurement campaign. Figure 46 shows a photo of the transmitter location.

Depending on the measurement, a directional or omnidirectional antenna was used at the receiver. Like the transmit antenna, the receive antenna was mounted atop a 180 centimeter pole made of PVC. The received signal was processed via sliding correlation using a PN identical to the transmitter's but with a chip rate

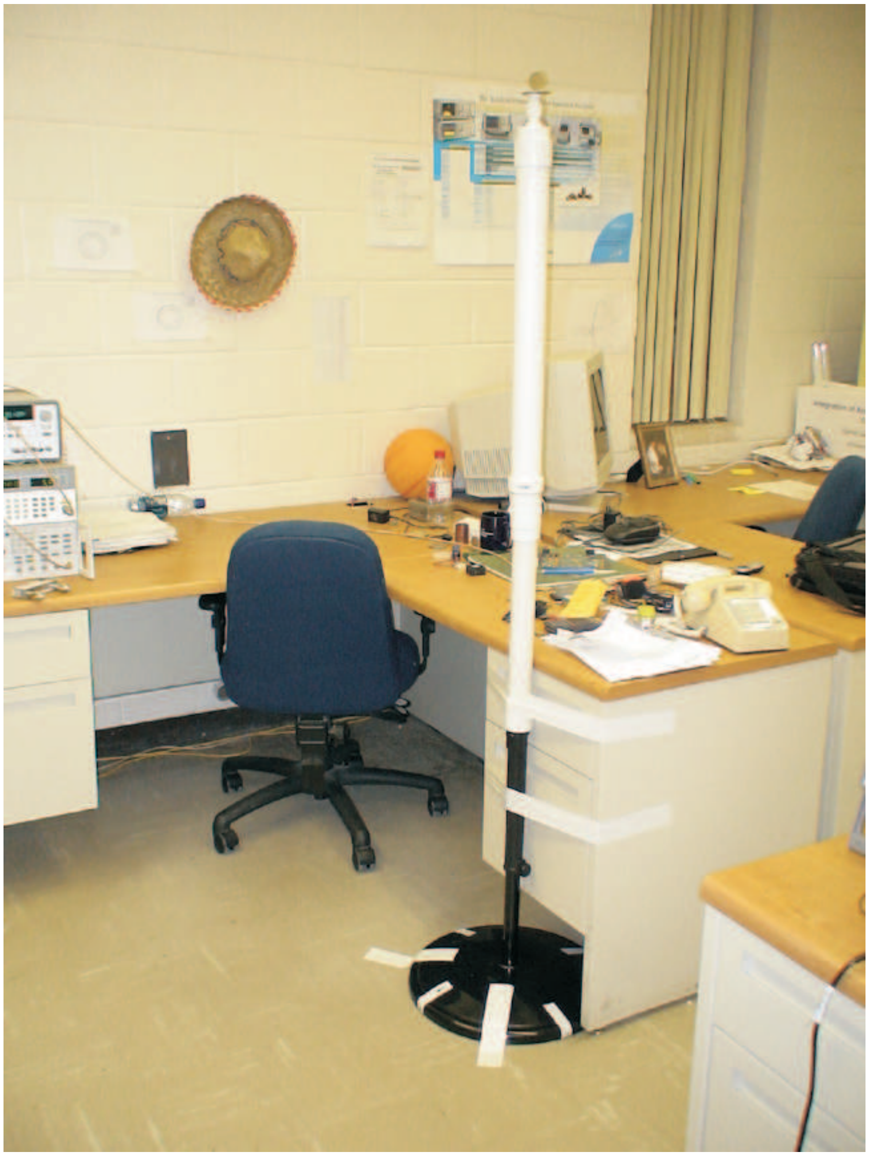

Figure 46: The transmitter was located in a typical office environment with the antenna mounted atop a 180 cm pole.

of 599.99 MHz. A spectrum analyzer mixed the RF waveform down to 21.4 MHz whereupon it was sampled by a digital oscilloscope. Post-processing converted the IF waveform to a complex baseband signal and provided additional filtering.

5.2 Procedure

According to Equation (18), for a complex baseband bandwidth of 600 MHz, the local area distance is 1/2 meter. Thus, at each receiver location, measurements were confined to a circular region with a diameter of 1/2 meter. Two types of measurements were performed within each local area: omnidirectional and directional.

5.2.1 Omnidirectional Measurements

An omnidirectional antenna was used at the receiver to measure the CIR along two orthogonal and intersecting 50 cm tracks. For a 4.1 GHz RF carrier and a 600 MHz chip rate, the highest radiated frequency was approximately 4.7 GHz. At this frequency, the 6.4 cm wavelength requires a spatial sampling period no greater than 3.2 cm ($\lambda/2$) for coherent measurements and 1.6 cm ($\lambda/4$) for incoherent measurements. This measurement campaign was originally undertaken under the assumption that the channel sounder's phase stability produced coherent measurements; thus a uniform spatial sampling period of 2 cm was chosen. Analysis of the calibration data during post-processing led to the realization that the channel sounder lacked phase stability, as was reported in Chapter 4. Therefore, the smaller spatial sampling rate would lead to a slight aliasing of the spatial frequencies and thereby, an underestimation of the spatial power fading rate. The effects of this smaller spatial samping rate for incoherent measurements will be discussed in more detail in Section 5.5.2.

With a uniform spatial sampling period of 2 cm for the 1/2 meter diameter local area, a total of 25 measurements were taken along each of the orthogonal tracks. By design of the track layout, two CIRs were recorded at the tracks' intersection. Comparison of these two CIRs during post-processing lent confidence to the static

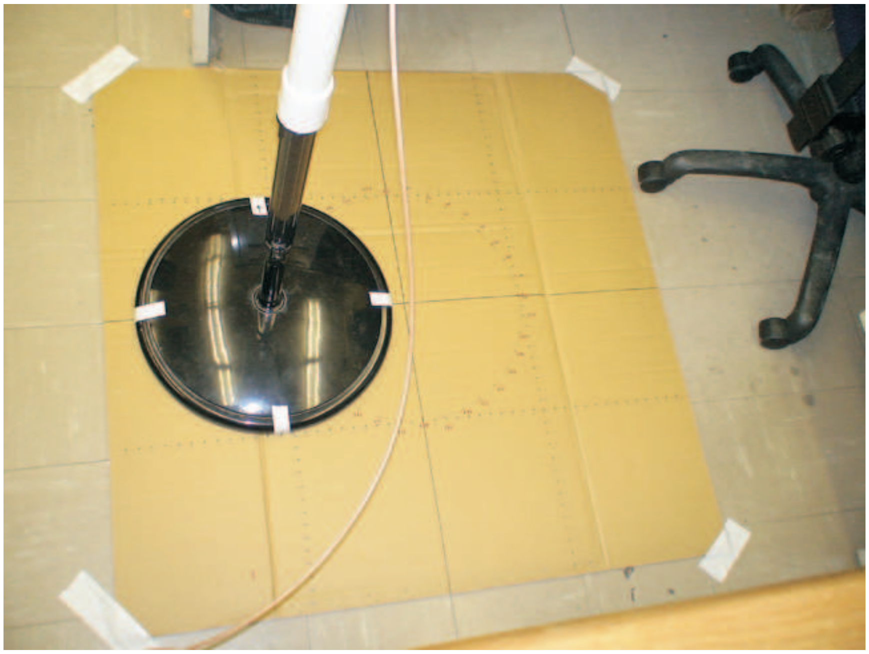

Figure 47: Omnidirectional measurements were made at 2 cm intervals along two orthogonal tracks within the local area. Directional measurements were made at the tracks' intersection at 10° intervals.

channel assumption. Figure 47 shows the grid used to position the receive antenna for both directional and omnidirectional measurements. The grid overlayed a Cartesian and polar coordinate system to allow for both translation along the orthogonal axes as well as rotation at the intersection of the axes.

5.2.2 Directional Measuremeents

A directional antenna was used at the receiver to measure the CIR along the azimuth at the center of the local area (i.e., at the intersection of the omnidirectional tracks.) The main beam of the directional antenna was swept from 0° to 360° at 10° intervals using the grid shown in Figure 47. This produced a pair of mesurements at 0/360°. Comparison of these two CIRs during post-processing again lent confidence to the static channel assumption.

Note that most angle spectrum measurements involve multiple sets of narrowband directional power measurements at different points within the local area [12]. These measurements are later spatially averaged to produce the angle spectrum. Here, the large bandwidth of the sliding correlator channel sounder greatly simplifies the problem. As indicated by Equation (20), frequency averaging of wideband measurements is analagous to spatially averaging narrowband measurements. Thereby, the angle spectrum may be derived from the frequency average of just one set of wideband rotational measurements.

5.3 Measurement Sites

Omnidirectional and directional CIR measurements were performed at 7 sites on the 5th floor of the Van Leer building at the Georgia Institute of Technology. Figure 48 indicates the measurement sites (denoted *A*-*G*) as well as the transmitter site (denoted *Tx*). The 5th floor is the top floor of this academic building, which consists mainly of offices and laboratories. The measurement environment contained common office furniture such as desks, chairs, and computers as well as academic and laboratory items such as chalkboards and measurement equipment. All measurements were performed late at night in evacuated areas to minimize the channel's temporal variations. Descriptions and photos of the individual measurement sites may be found in Appendix B.

5.4 Results

The following sections discuss the information obtained from the channel measurements. Where applicable, example curves are provided from measurement data recorded at site C. A summary of the measurement results is presented in Table 3. Plots of each site's delay and azimuthal angle spectrum may be found in Appendix B. Site measurement data was packaged into individual *MATLAB* structs for general use and distribution. Information about the data format is discussed in Appendix C.

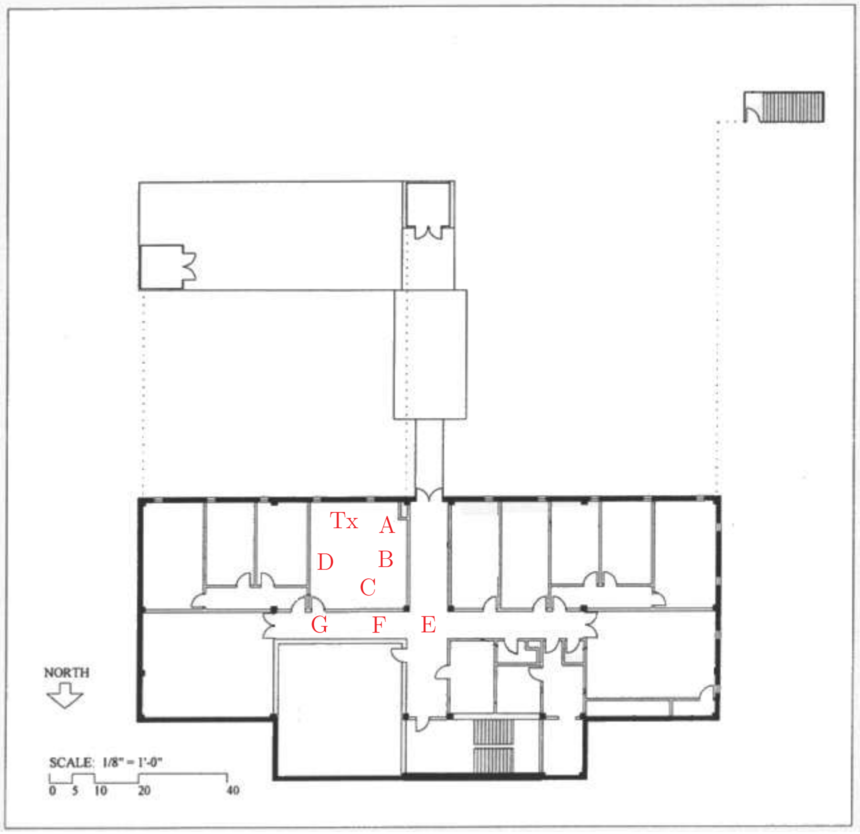

Figure 48: Measurements were performed on the 5th floor of Van Leer, a typical academic building at the Georgia Institute of Technology. The 7 receiver locations are marked *A*-*G*; the transmiter location is marked *Tx*.

Table 3: Summary of Measurement Results

Site	**Type**	**Distance**	$\sigma_{\tau,-10dB}$	$\sigma_{\tau,-20dB}$	$\sigma_{\tau,6dB}$	Λ **from** $p(\theta)$	Λ **from** $\sigma^2_{\hat{r}}$
A	LOS	2.7 m	0.91 ns	9.3 ns	14.6 ns	0.62	0.57
B	LOS	4.0 m	3.2 ns	10.5 ns	16.1 ns	0.71	0.56
C	LOS	4.8 m	5.2 ns	11.0 ns	14.7 ns	0.82	0.70
D	LOS	2.5 m	0.54 ns	10.2 ns	15.0 ns	0.74	0.55
E	NLOS	9.1 m	4.9 ns	14.0 ns	19.3 ns	0.68	0.51
F	NLOS	6.9 m	5.7 ns	12.7 ns	16.1 ns	0.92	0.59
G	NLOS	6.9 m	9.8 ns	16.5 ns	18.8 ns	0.89	0.66

5.4.1 Channel Impulse Response

The CIR is the direct result of the sliding correlator channel sounder and is proportional to received voltage as a function of excess delay. CIRs were obtained using an omnidirectional and directional antenna, and it is important to distinguish between the two types of CIRs. Therefore, the following notation will be used: CIRs recorded with the omnidirectional antenna will be denoted $\tilde{H}(\tau;\vec{r})$ where $\vec{r}$ represents the position of the antenna relative to the center of the local area; CIRs recorded with the directional antenna will be denoted $\tilde{H}(\tau;\theta)$ where θ is the azimuthul direction of the antenna's main beam. Figures 49(a) and 49(b) present a measured omnidirectional and directional CIR, respectively.

5.4.2 Power-Delay Profile

The power-delay profile (PDP) is proportional to the received power as a function of excess delay. It is defined as the magnitude-squared of the CIR:

$$P(\tau;\vec{r}) = \left|\tilde{H}(\tau;\vec{r})\right|^2 \tag{101}$$

The PDP represents the path gain in the wireless channel at a given location and excess delay. Figure 50 shows an example PDP. Figure 51 presents a space-time PDP comparing the individual PDPs measured along one of the orthogonal tracks.

5.4.3 Delay Spectrum

The delay spectrum was described in detail in Section 2.5.1. It represents a power density as a function of excess delay for the local area. If the channel may be assumed a random process that is ergodic with respect to space, then the delay spectrum may be derived from a set of spatially distributed omnidirectional channel measurements according to

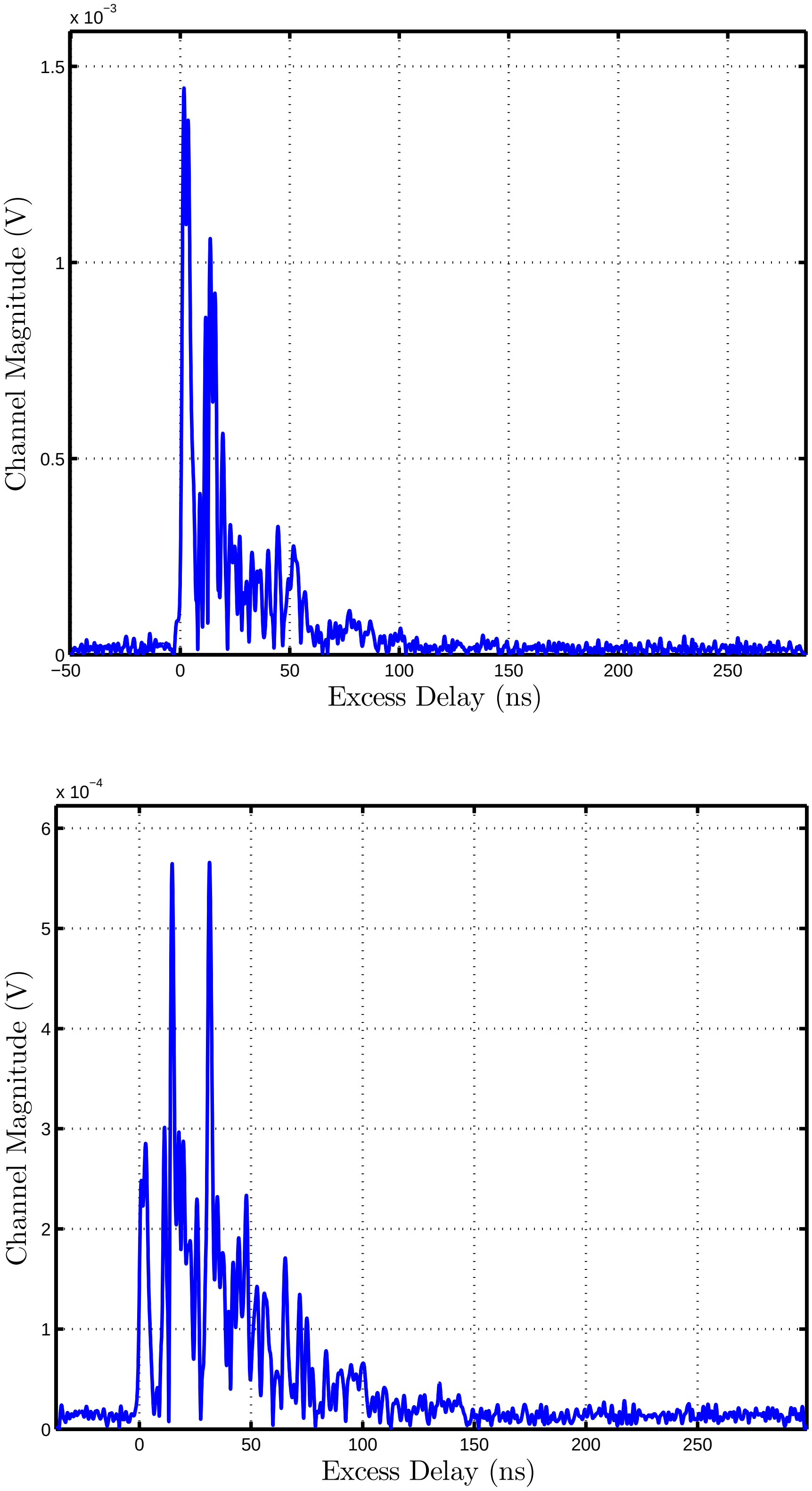

(a)

(b)

Figure 49: Two CIRs obtained from site C: (a) omnidirectional and (b) directional.

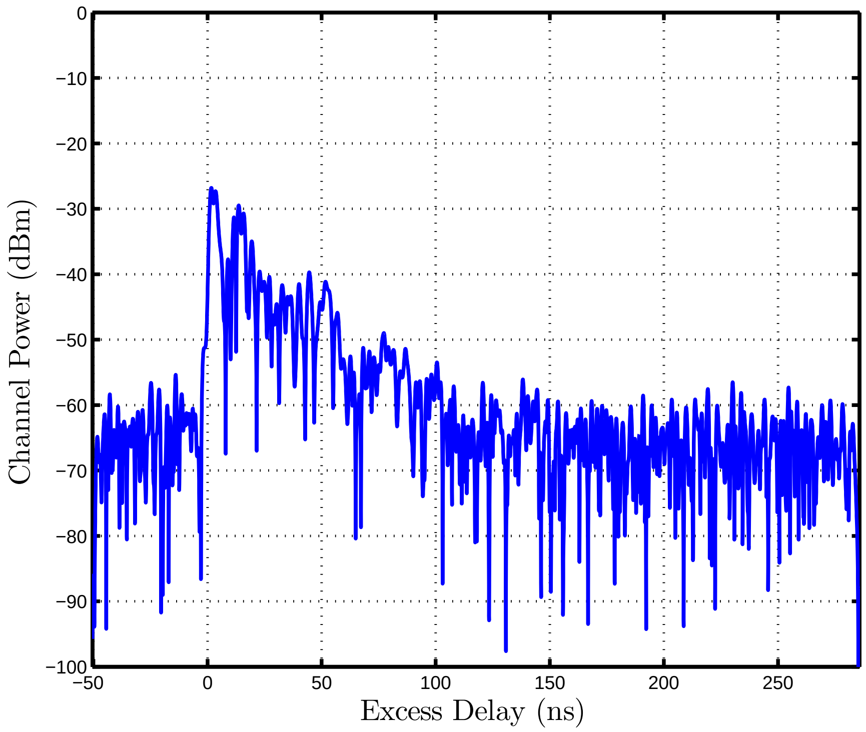

Figure 50: A PDP measured at site C.

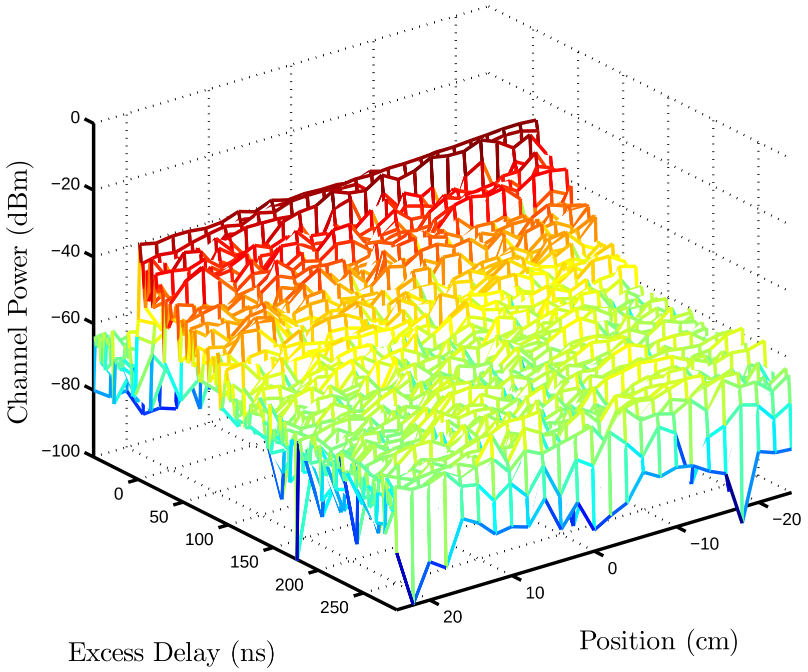

Figure 51: A space-time PDP measured at site C along one of the orthogonal tracks.

$$S_{\tilde{h}}(\tau) = \left\langle \left| \tilde{h}(\tau, \vec{r}) \right|^2 \right\rangle_{\vec{r}} \tag{102}$$

Using the delay spectrum, one may also calculate the RMS delay spread, σ_τ, for the local area using (26). Although the RMS delay spread may be calculated directly from the delay spectrum, it is common practice to impose a threshold on the delay spectrum lest the system noise floor be included in the calculation [20]. Threshold values may be specified relative to the largest received multipath component, the noise floor of the receiver, or the dynamic range of the system. Only parts of the delay spectrum above the threshold are included in the calculation. Here, RMS delay spreads will be calculated in three ways: 1) with a -10 dB threshold relative to the largest multipath component ($\sigma_{\tau,-10dB}$), 2) with a -20 dB threshold relative to the largest multipath component ($\sigma_{\tau,-20dB}$), and 3) with a 6 dB threshold relative to the measurement noise floor ($\sigma_{\tau,6dB}$). Figure 52 shows the measured delay spectrum for a set of omnidirectional measurements from one local area, along with each of the threshold levels. The three different thresholds for RMS delay spread yield $\sigma_{\tau,-10dB} =$ 5.2 ns, $\sigma_{\tau,-20dB} = 11.0$ ns, and $\sigma_{\tau,6dB} = 14.7$ ns.

5.4.4 Azimuth Spectrum

The azimuth spectrum was discussed in Section 2.6. It represents a power density as a function of azimuth angle for the local area. If the channel may be assumed ergodic with respect to frequency and multipath restricted to from-the-horizon propagation, then the azimuth spectrum may be derived from a set of directional broadband channel measurements according to

$$p(\theta) = \left\langle \left| \tilde{h}(f, \theta) \right|^2 \right\rangle_f \tag{103}$$

where $\tilde{h}(f, \theta)$ is the Fourier transform of the directional CIR as given by

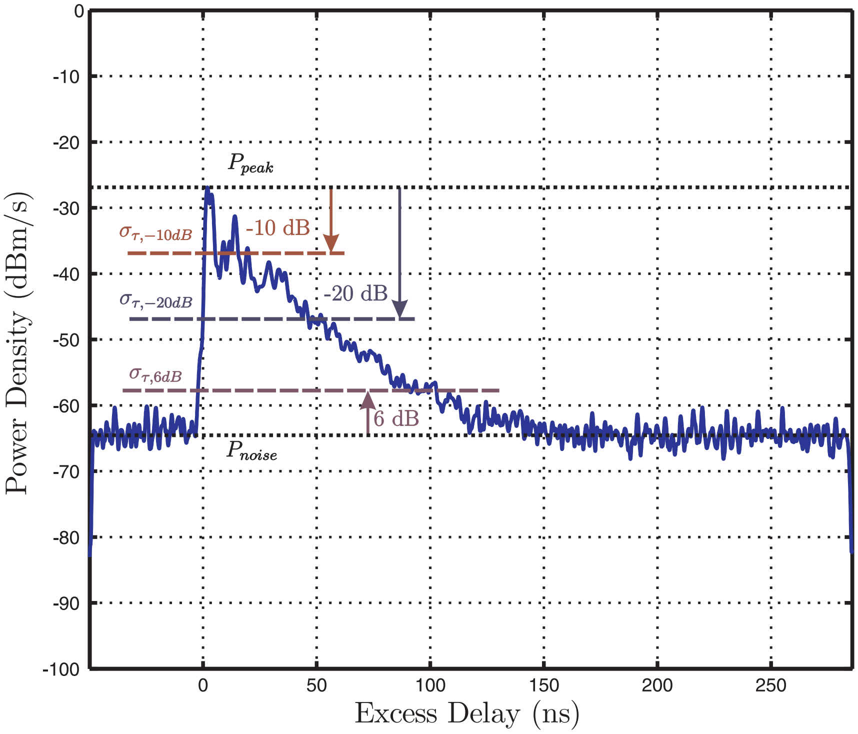

Figure 52: The delay spectrum measured at site C with threshold values for corresponding RMS delay spread calculations. Note that this is actually a plot of $10\log_{10}(|S_{\tilde{h}}(\tau)|/10^{-3})$, where $S_{\tilde{h}}(\tau)$ has linear units of Watts/second. The specified units of (dBm/s) are meant to indicate power density on a log scale. The -20 dB RMS delay spread was calculated to be $\sigma_{\tau,-20dB} = 11.0$ ns.

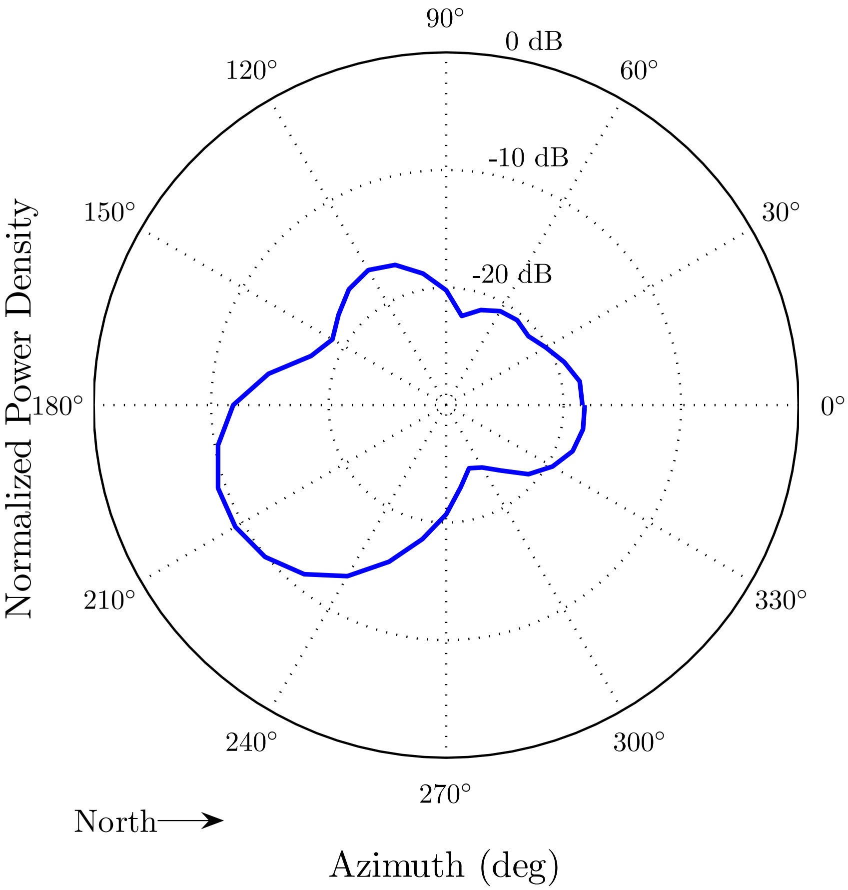

Figure 53: The normalized angle spectrum measured at site C. The angular spread, Λ, was determined to be 0.82.

$$\tilde{h}(f, \theta) = \int_{-\infty}^{\infty} \tilde{H}(\tau; \theta) e^{-j2\pi\tau f} d\tau \tag{104}$$

Using the azimuth spectrum, one may determine the angular spread, Λ, according to Equation (38). Figure 53 shows an example measured azimuth spectrum that has been normalized by the total received power. Note that this normalization has no effect on the calculation of the angular spread, which was $\Lambda = 0.82$ at site C.

5.4.5 Angular Spread from Fading Rate Variance

The angular spread may also be calculated from a pair of power spatial fading rate variances corresponding to two orthogonal tracks within the local area as discussed in Section 2.6.3. This approach assumes the channel can be modeled by a space ergodic SLAC with independent phases and heterogeneous scattering. Provided this assumption, the power spatial fading rate variance along each track may be calculated according to Equation (42) wherein $\tilde{h}(\vec{r})$ is

$$\tilde{h}(\vec{r}) = \int_{-\infty}^{\infty} \tilde{H}(\tau;\vec{r})d\tau \tag{105}$$

Given two such variances, $\sigma_{\hat{x}}^2$ and $\sigma_{\hat{y}}^2$, obtained from two orthogonal track measurements along $\hat{x}$ and $\hat{y}$ respectively, the angular spread may be calculated using Equation (43), wherein P_R may be calculated from the a set of spatially distributed channel measurements according to Equation (20). For site C, whose measured azimuth spectrum was presented in Figure 53, the angular spread calculated using this approach was 0.70.

5.5 Analysis

The following sections provide an analysis of the measured RMS delay spreads and angular spreads and, where possible, provides a comparison to values found in literature.

5.5.1 RMS Delay Spread

The delay spreads measured here compared well with indoor UWB delay spreads reported in the literature. For these measurements, the average LOS delay spread calculated for a -20 dB threshold was 10.2 ns; the average NLOS, 14.4 ns. UWB measurements in houses indicated an average LOS and NLOS delay spread of 4.7 and 8.2 ns, respectively [17]. Average UWB delay spreads in a factory environment ranged from 28 to 31 ns in LOS and 34 to 40 ns in NLOS [23]. These significantly larger delay spreads are ascribed to the large dimensions of the factory building as well as its abundance of metallic walls, pipes, scaffoldings, etc. In [16], researchers reported indoor UWB NLOS delay spreads of 12.8 ns and 13.7 ns in a room and corridor respectively. A UWB measurement campaign conducted in a university office environment resulted in average delay spreads of 5.41 and 13.7 for LOS and NLOS, respectively [10].

5.5.2 Angular Spread

While there have been several investigations of the angle-of-arrival of UWB channels [8, 7, 5], there have been to-date no reports of UWB angular spreads. Thus, the angular spreads presented here provide preliminary values for future comparisons.

It was expected that angular spread values calculated from the azimuth spectrum might be overestimates due to the beamwidth of the directional antenna. More precisely, it was expected that the directional antenna's radiation pattern would impose a lower bound of approximately 0.37 on the angular spread. This value corresponds to the angular spread of the radiation pattern at the carrier frequency of 4.1 GHz. Examining Table 3, it may be seen that the smallest Λ calculated from $p(\theta)$ was 0.62 at site A, which was a LOS measurement 2.7 meters from the transmitter. This would indicate that the indoor UWB channel has an angular spread that is insensitive to the beamwidth of the directional antenna used here and thereby lends confidence to the validity of the angular spreads calculated from the azimuth spectrum.

For comparison, angular spreads were also calculated from the power spatial fading rate variances, $\sigma_{\hat{x}}^2$ and $\sigma_{\hat{y}}^2$. Figure 54 compares the angular spread pairs. Linear regression analysis on this scatter plot indicated a positive correlation between the two angular spreads. This in itself is encouraging, as it indicates that both approaches are measuring the same phenomenon, albeit with different scales. The power spatial fading rate variance approach led to consistently smaller angular spreads as compared to those calculated directly from the azimuth spectrum. This is likely due to the inadequate spatial sampling rate used for the omnidirectional track measurements.

Incoherent measurements require a spatial sampling rate of $\lambda/4$ to accurately capture the spatial power variations of the channel. However, due to the initial assumption that the channel sounder made coherent measurements, a spatial sampling rate of $\lambda/3.2$ was used. This slower sampling rate would lead to aliasing of higher spatial frequencies and result in a slight underestimation of $\sigma^2_{\hat{r}}$, which would in turn lead to smaller angular spreads.

Provided this knowledge, the angular spread measurements from the azimuth spectrum are deemed most reliable, although these values may be slightly inflated due to the directional antenna's radiation pattern. It is expected that more accurate angular spread values might be attained by deconvolving the directional antenna's radiation pattern from the measured azimuth spectrum as done in [15]. However, this approach requires both phase stable measurements and the antenna's complex radiation pattern. As an alternative, one might use the approach discussed in [38], wherein an iterative constrained deconvolution is used to improve the resolution of incoherent radar measurements.

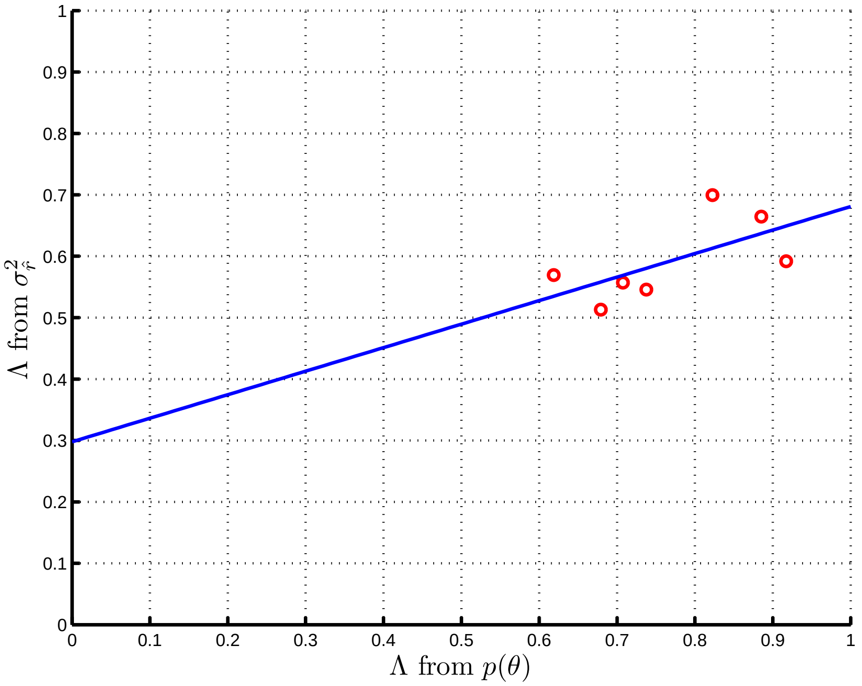

Figure 54: Linear regression performed on a plot of angular spread from $\sigma^2_{\hat{r}}$ versus angular spread from $p(\theta)$ indicates a positive correlation between the two methods.

CHAPTER VI

CONCLUSIONS

This document provides a practical and detailed guide for anyone interested in performing broadband wireless channel measurements. Although this work focused on the development of a UWB channel sounder, the fundamental concepts discussed herein are equally applicable to channel sounding at any frequency-bandwidth combination. Discussions of stochastic channel modeling and channel sounder design provided the framework for understanding the underlying principles of channel sounding. Implementation of the channel sounder design brought to light the challenges and practical considerations for system realization. Finally, the measurement campaign outlined a procedure for investigating the spatio-temporal characteristics of wireless channels.

6.1 Future Work

Future work will focus on improving the performance and utility of the realized channel sounder. The following sections highlight specific areas warranting improvements.

6.1.1 Dynamic Range

As was noted in Chapter 4, the system's dynamic range was hampered by two aspects: 1) the LO-RF isolation of both the transmitter's and receiver's mixer, and 2) the conversion loss at the receiver mixer during the sliding correlation with the receiver's PN. The poor dynamic range could be improved by using a mixer with better isolation. Alternatively, the conversion loss might be improved by using a shorter PN, which would allocate more of the sliding correlator product's power to the time-dilated autocorrelation signal. However, as discussed in Chapter 3, a shorter PN would also decrease the system's maximum attainable dynamic range.

6.1.2 PN Generator

The length of the PN was much longer than necessary for measuring the indoor UWB channel. At a chip rate of 600 MHz, the sequence length of 131,071 chips allowed for measuring excess path lengths of up to 65 kilometers! An improved PN generator would have a chip length of 1024 bits, which, at an idealized chip rate of 1 GHz, would allow for measurements of excess path lengths up to 153 meters. This would be more than ample for indoor measurements while still offering the capability to measure many outdoor channels. Furthermore, a shorter PN would improve the CIR sampling rate and, thereby, the maximum Doppler resolution of the channel sounder. In addition, a shorter PN allows for a reduction in the propagation delays along the LFSR's feedback loop, which would lead to improvements in the LFSR's maximum chip rate.

6.1.3 Miniaturization

The channel sounder system used the following lab equipment: three bench power supplies, three signal generators, a spectrum analyzer, and a digital oscilloscope. These instruments contributed mass, bulk, and cost to the system, all of which could be significantly reduced with careful redesign. The three bench power supplies could be replaced with a pair of multiple-output linear power supplies: one for the transmitter and one for the receiver. The three signal generators could be replaced with three phase-locked loop-based frequency synthesizers. The spectrum analyzer, which provided gain control and downconversion to IF, could be replaced with a custom RF front-end complete with automatic gain control and inphase and quadrature outputs. The digital oscilloscope could be replaced by an ADC and data buffer for temporary storage of the measurement data until it can be downloaded by a computer. Further miniaturization could be achieved through surface mount RF mixers, amplifiers, and filters, which would allow the entire RF front-end to be realized on a single printed circuit board.

6.2 Toward SIMO and MIMO Channel Sounding

The previous section pointed out system modifications for the single-input single-output (SISO) channel sounder that was discussed in this work. Although a prevalent system architecture for curent wireless communication systems, the trend toward multiple antennas at both the transmitter and receiver cannot be ignored. Thankfully, the simplicity of the the sliding correlator chanel sounder architecture allows it to be easily modified for broadband multi-antenna channel sounding. For single-input multiple-output (SIMO) channel sounding, which is characterized by a single transmit antenna and multiple receive antennas, one can simply add another receiver chain to the system. This simple design modification would allow phase stable spatial channel measurements without the need for oscillator synchronization via restrictive cables or expensive atomic master oscillators.

To investigate multiple-input multiple-output (MIMO) channels, one would replace the m-sequences discussed in Chapter 3 with Gold codes [18]. The well-characterized cross-correlation of Gold code sets makes them the ideal choice for measuring the complex channel matrix of MIMO systems. Unfortunately, with this approach, the receiver's complexity would scale with the number of elements in the channel matrix, because the cross-correlation must be implemented in hardware for each of the transmit-receive antenna pairs. Thus, for narrowband MIMO channel investigations, an adaptation of the spread spectrum channel sounding technique may prove a more cost-effective approach. However, for wideband and ultra-wideband MIMO channel sounding, the bandwidth compression afforded by the sliding correlator might easily tip the scales in its favor.

APPENDIX A

PN SCHEMATIC

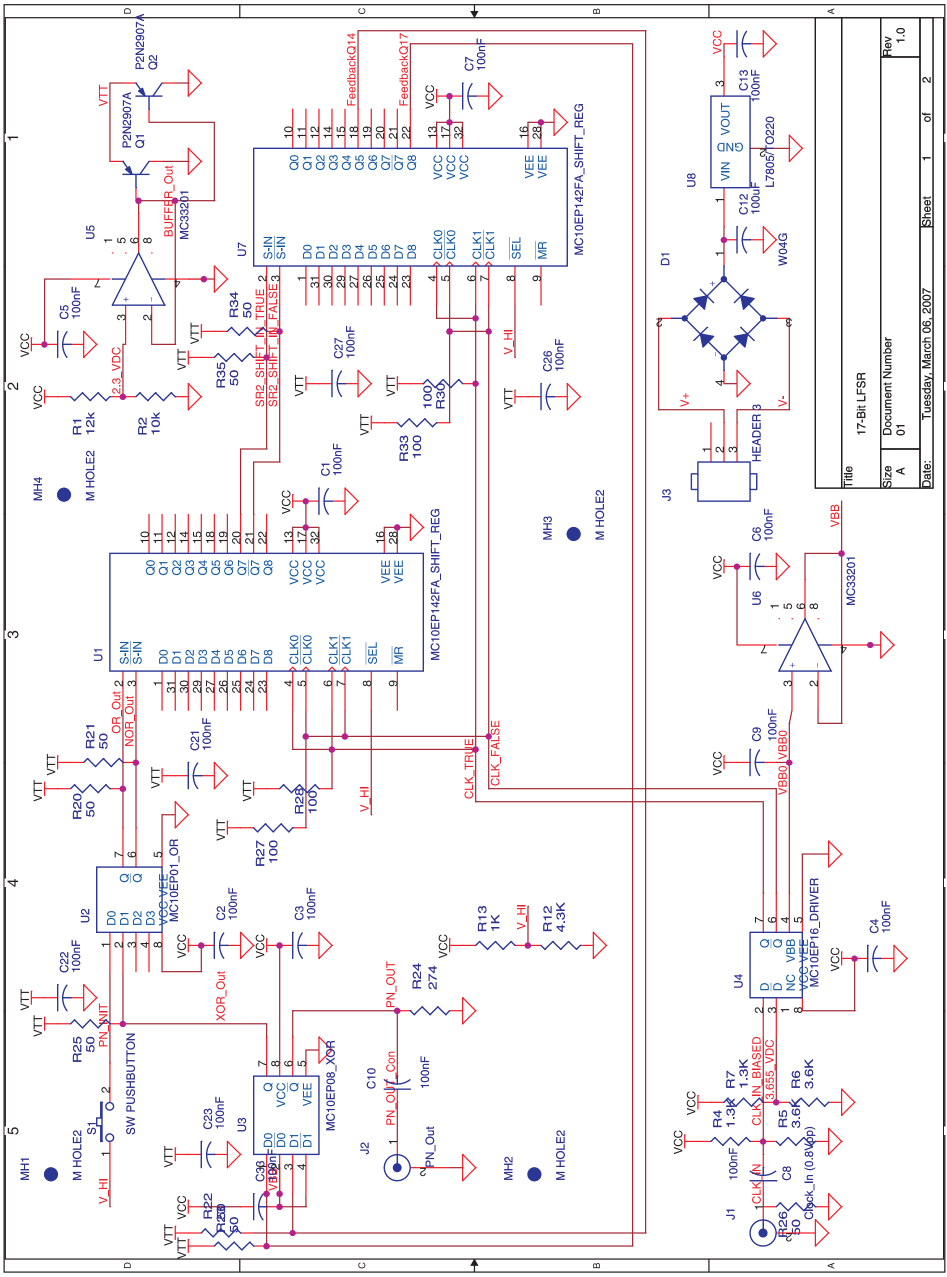

Figure 55: Schematic of the PN generator based upon a 17-bit LFSR.

APPENDIX B

MEASUREMENTS

B.1 Site A

Site A was located in the same room as the transmitter at a distance of approximately 2.7 meters. A LOS path existed between the transmitter and receiver.

Figure 56: Site A was a LOS measurement approximately 2.7 meters from the transmitter.

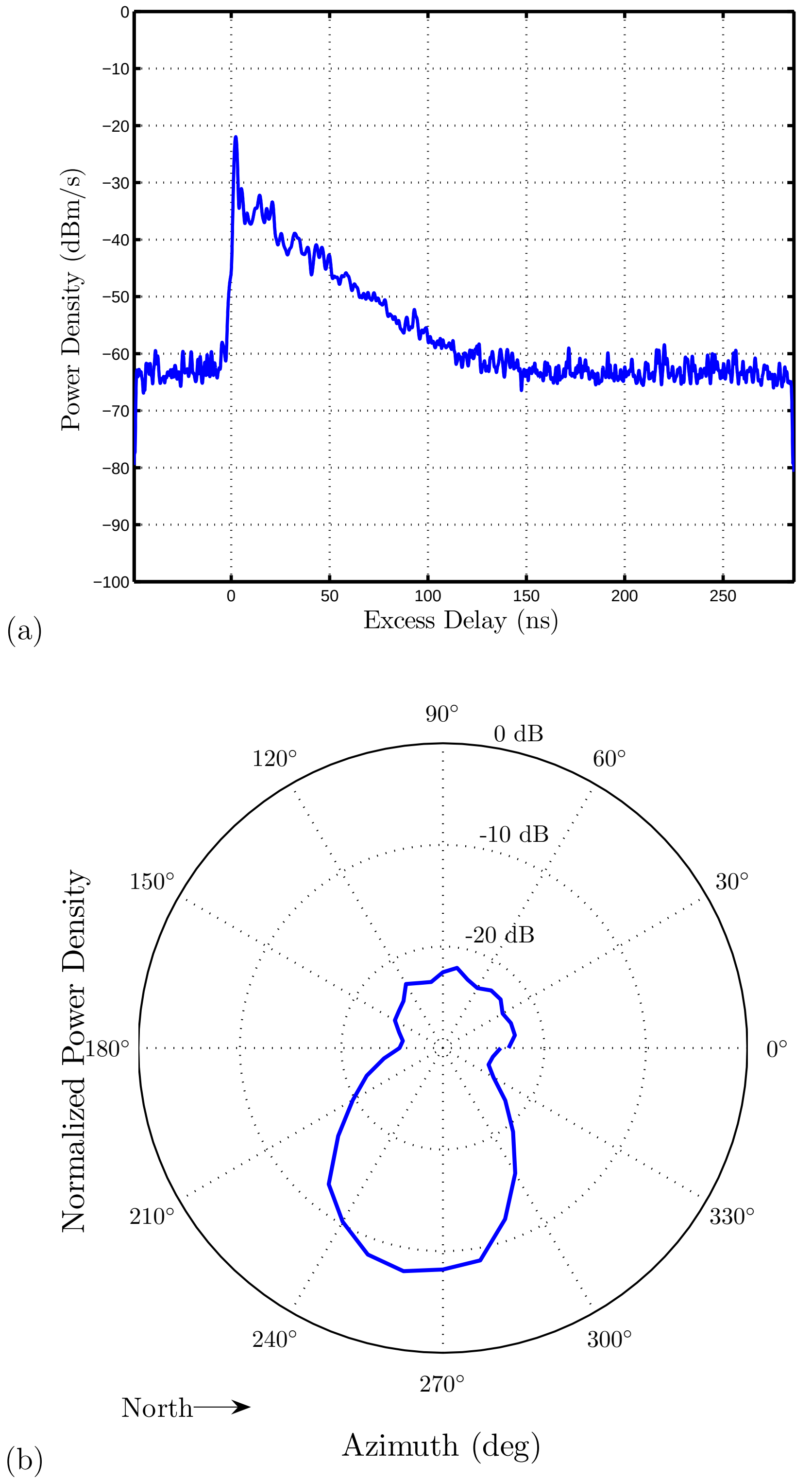

Figure 57: The (a) delay spectrum and (b) azimuth spectrum for site A.

B.2 Site B

Site B was located in the same room as the transmitter at a distance of approximately 4 meters. A LOS path existed between the transmitter and receiver.

Figure 58: Site B was a LOS measurement approximately 4 meters from the transmitter.

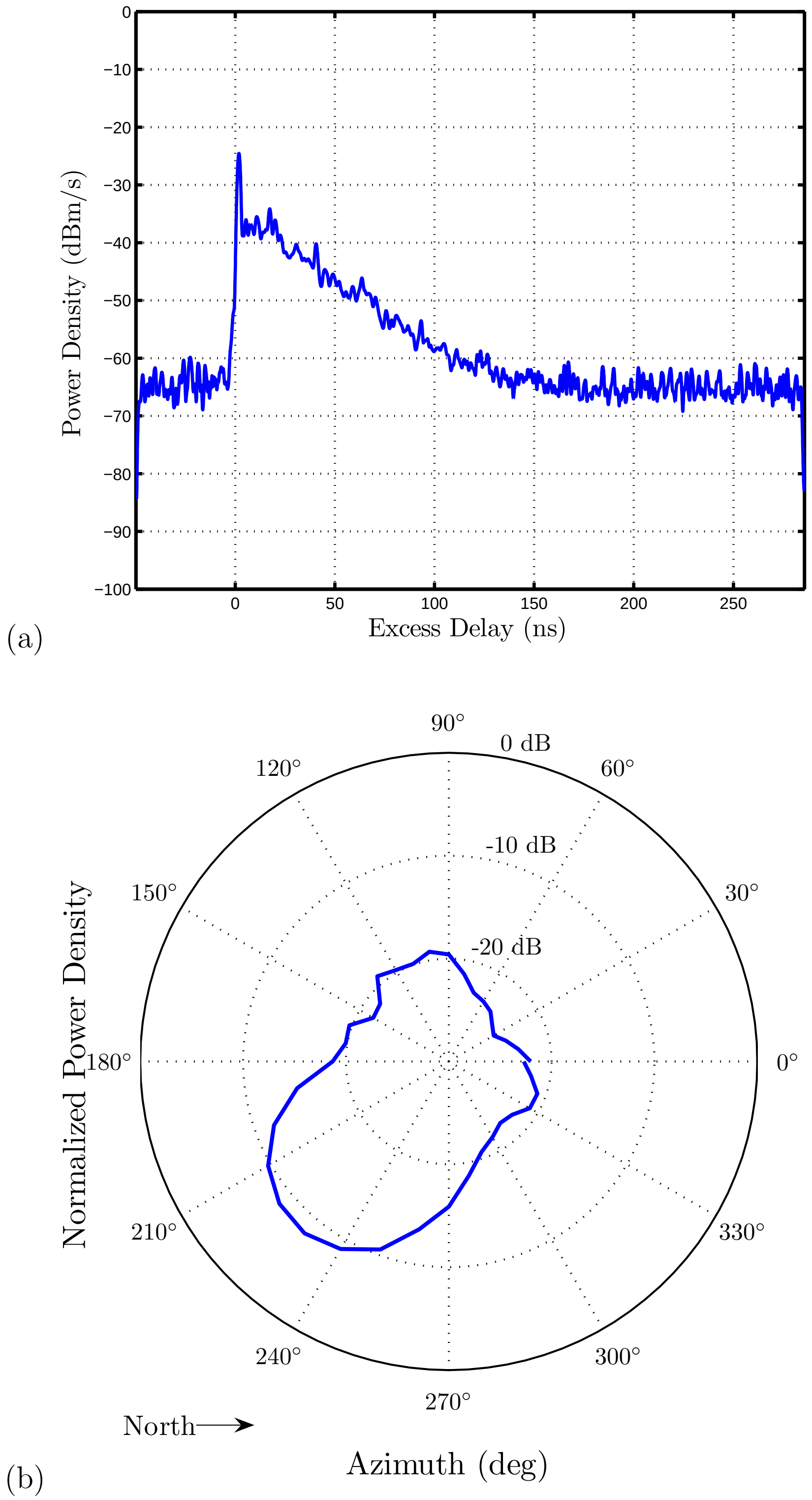

Figure 59: The (a) delay spectrum and (b) azimuth spectrum for site B.

B.3 Site C

Site C was located in the same room as the transmitter at a distance of approximately 4.8 meters. A LOS path existed between the transmitter and receiver.

Figure 60: Site C was a LOS measurement approximately 4.8 meters from the transmitter.

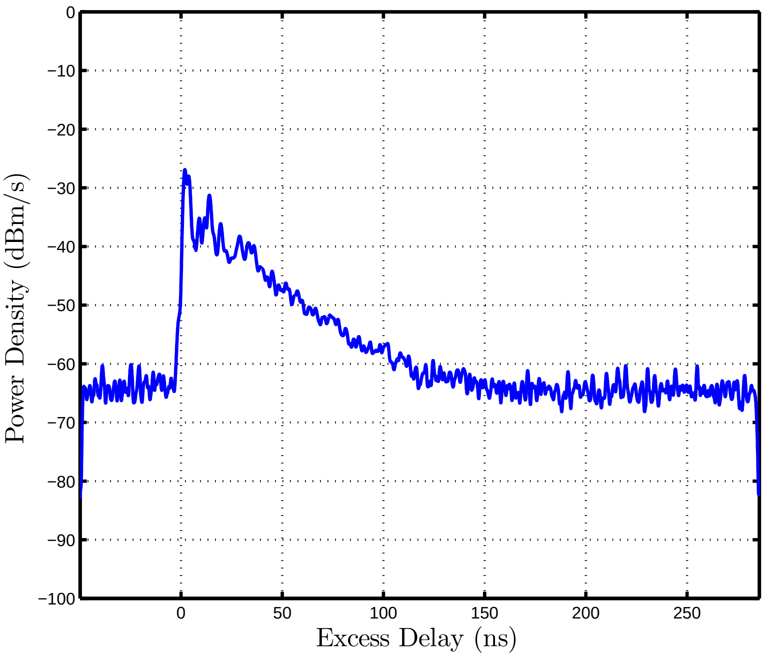

(a)

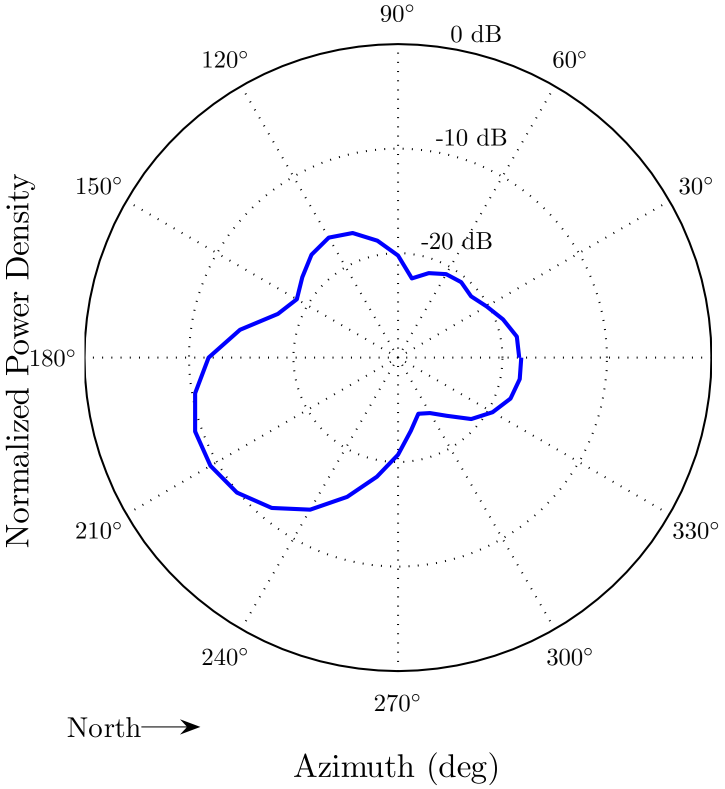

(b)

Figure 61: The (a) delay spectrum and (b) azimuth spectrum for site C.

B.4 Site D

Site D was located in the same room as the transmitter at a distance of approximately 2.5 meters. A LOS path existed between the transmitter and receiver.

Figure 62: Site D was a LOS measurement approximately 2.5 meters from the transmitter.

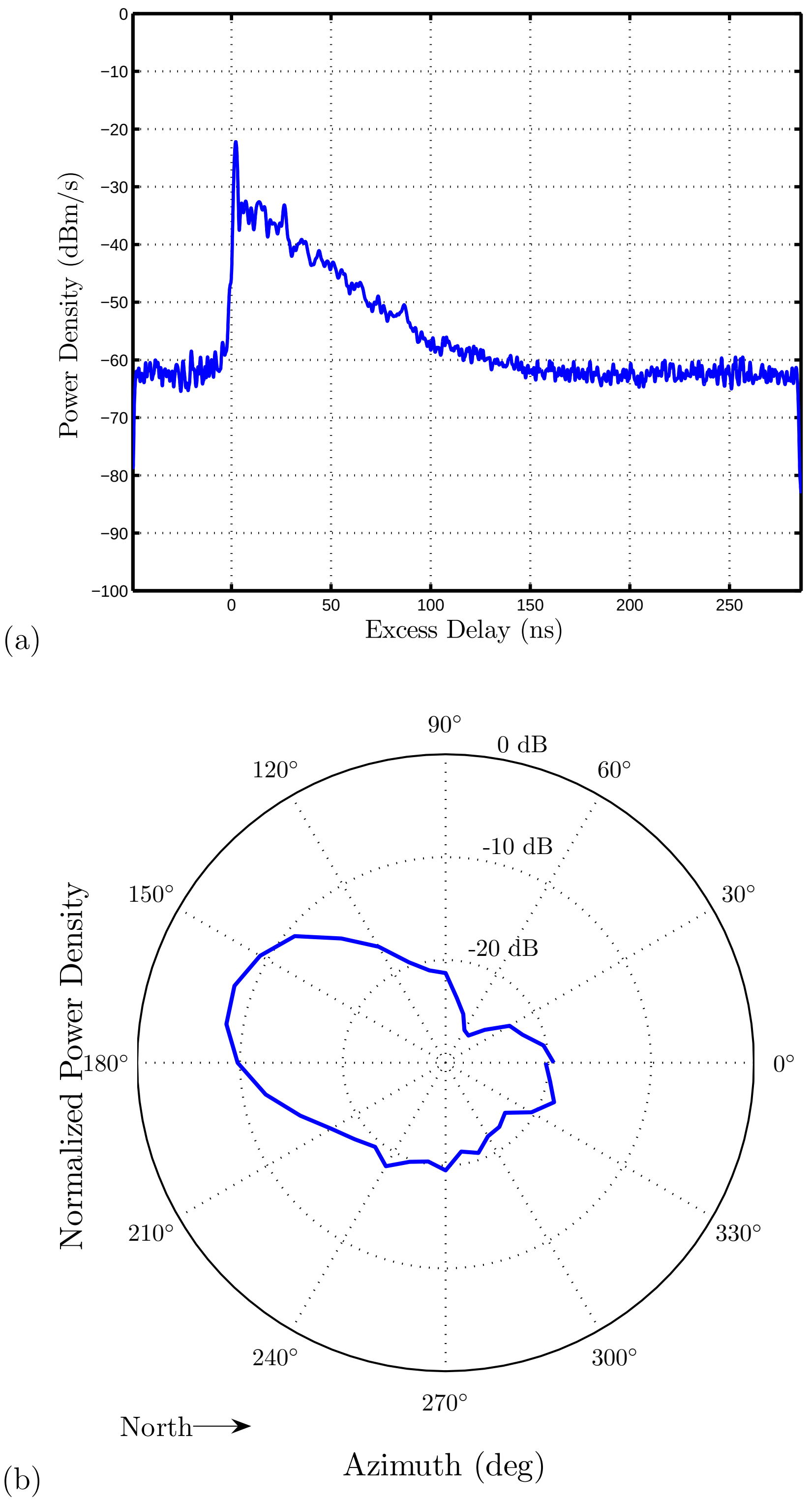

Figure 63: The (a) delay spectrum and (b) azimuth spectrum for site D.

B.4.1 Site E

Site E was located at the intersection of a hallway adjacent to the room with the transmitter. The separation distance was approximately 9.1 meters.

Figure 64: Site E was a NLOS measurement approximately 9.1 meters from the transmitter.

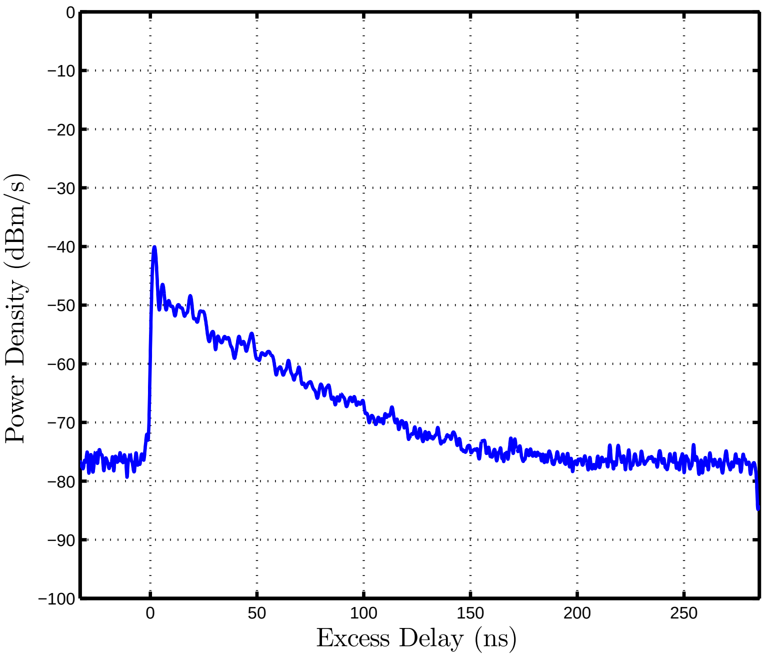

(a)

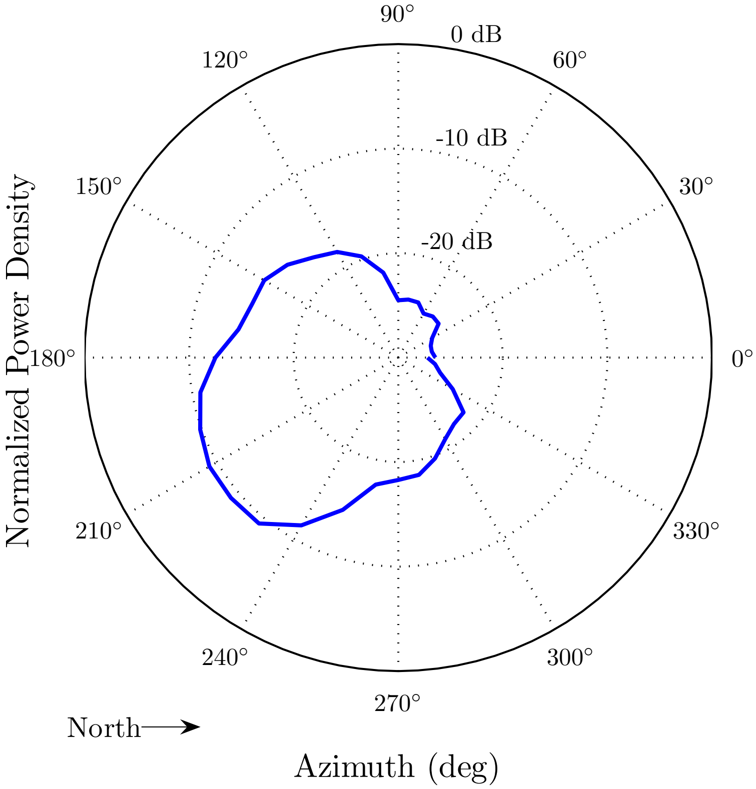

(b)

Figure 65: The (a) delay spectrum and (b) azimuth spectrum for site E.

B.5 Site F

Site F was located in the hallway adjacent to the room with the transmitter. The separation distance was approximately 6.9 meters.

Figure 66: Site F was a NLOS measurement approximately 6.9 meters from the transmitter.

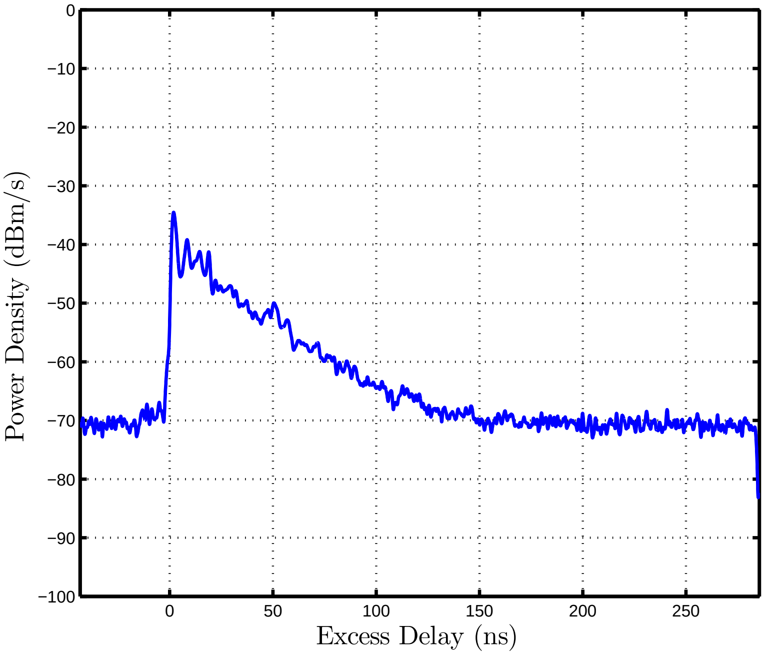

(a)

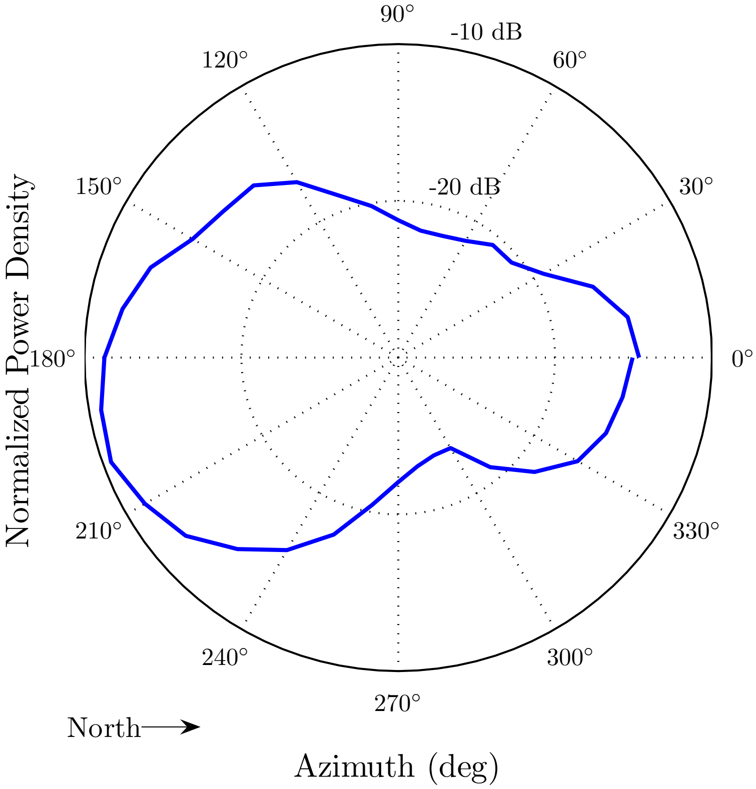

(b)

Figure 67: The (a) delay spectrum and (b) azimuth spectrum for site F.

B.6 Site G

Site G was located in the hallway in front of the doorway to the room with the transmitter. The separation distance was approximately 6.9 meters.

Figure 68: Site G was a NLOS measurement approximately 6.9 meters from the transmitter.

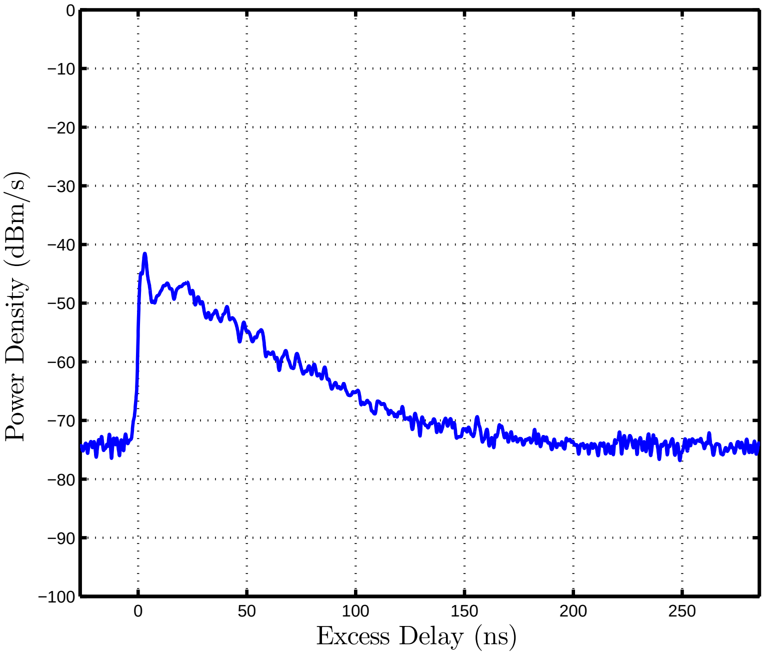

(a)

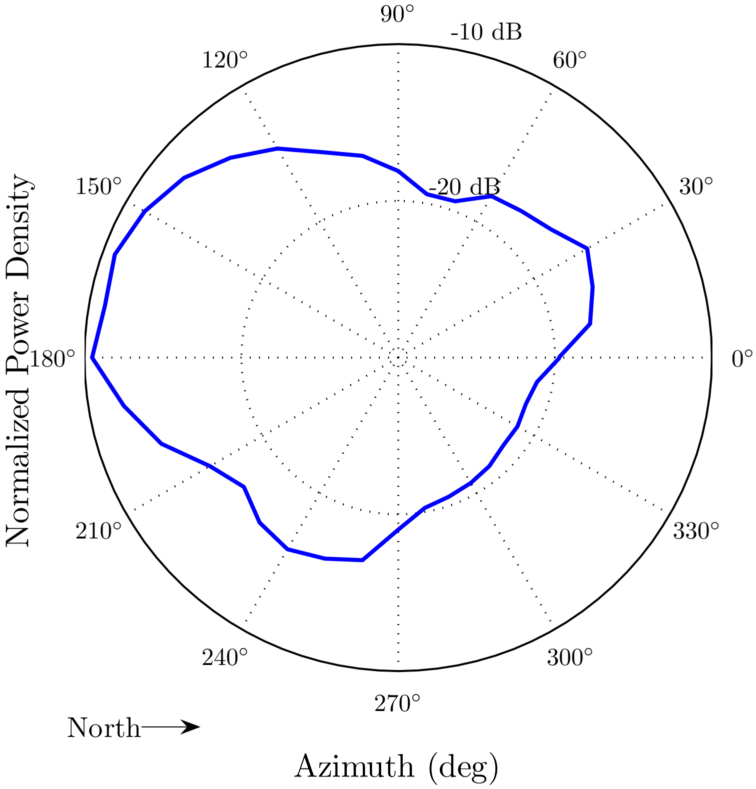

(b)

Figure 69: The (a) delay spectrum and (b) azimuth spectrum for site G.

APPENDIX C

MEASUREMENT DATA FORMAT

Data from each measurement site was compiled into individual *MATLAB MAT* files. The naming convention for each site's file was *SiteXData.mat* where X is an alphanumeric character or string that uniquely identifies the measurement location. Within this file is a struct *site*, which contains all of the data gathered from each site. The fields of the *site* struct are as follows:

site.name *String*, site identification

site.date *String*, measurement date

site.f0 *double*, carrier frequency

site.distance *double*, distance from transmitter to receiver

site.type *String*, idicates a LOS or NLOS measurement

site.description *String*, brief description of the measurement location

site.data *struct*, 1 x M array of structs containing M CIRs and accompanying information

Each element of the *site.data* array contains information specific to a single CIR measurement. The fields of the kth element of the *site.data* struct array are as follows:

site.data(k).cir *complex double*, n x 1 array of samples corresponding to the discretized complex CIR measurement

site.data(k).fs *double*, sampling frequency

site.data(k).type *String*, identifies measurement type; *angle*: directional, *x,y*: omnidirectional along orthogonal track

site.data(k).pos *double*, position or angle of omnidirectional or directional measurement, respectively; track measurement positions are in meters, rotational measurement angles are in degrees

REFERENCES

[1] Agilent Technologies, *Agilent ESA-E Series Spectrum Analyzer Specifications Guide*, 2003.

[2] Anderson, C., "Design and implementation of an ultrabroadband millimeter-wavelength vector sliding correlator channel sounder and in-building multipath measurements at 2.5 & 60 GHz," master's thesis, Virginia Tech, May 2002. Online: http://scholar.lib.vt.edu/theses/available/etd-05092002-101656/unrestricted/AndersonThesisETD.pdf.

[3] Benvenuto, N., "Distortion analysis on measuring the impulse response of a system using a crosscorrelation method," *AT&T Bell Laboratories Technical Journal*, vol. 63, pp. 2171–2192, December 1984.

[4] Bryant, J. H., *Heinrich Hertz: The Beginning of Microwaves.* New York, NY: IEEE, Inc., 1988.

[5] Buehrer, R. M., Davis, W. A., Safaai-Jazi, A., and Sweeney, D., "Ultra-wideband propagation measurements and modeling," tech. rep., Va Tech, http://www.mprg.org/people/buehrer/ultra/darpa_netex.shtml, 31 Jan 2004.

[6] Cox, D. C., "Delay Doppler characteristics of multipath propagation at 910 MHz in a suburban mobile radio environment," *IEEE Transactions on Antennas and Propagation*, vol. 20, pp. 625–635, September 1972.

[7] Cramer, R. J.-M., Scholtz, R. A., and Win, M. Z., "Spatio-temporal diversity in ultra-wideband radio," in *1999 IEEE Wireless Communications and Networking Conference*, vol. 2, pp. 888–892, 21-24 Sep 1999.

[8] Cramer, R. J.-M., Scholtz, R. A., and Win, M. Z., "Eavulation of an ultra-wide-band propagation channel," *IEEE Transactions on Antennas and Propagation*, vol. 50, pp. 561–570, May 2002.

[9] Dixon, R. C., *Spread Spectrum Systems with Commerical Applications.* John Wiley and Sons, Inc., 1994.

[10] Donlan, B. M., Venkatesh, S., Bharadwaj, V., Buehrer, R. M., and Tsai, J.-A., "The ultra-wideband indoor channel," in *IEEE Vehicular Technology Conference 2004*, vol. 1, pp. 208–212, 17-19 May 2004.

[11] Durantini, A. and Cassioli, D., "A multi-wall path loss model for indoor UWB propagation," in *IEEE Vehicular Technology Conference*, vol. 1, pp. 30–34, 2005.

[12] Durgin, G. D., Kukshya, V., and Rappaport, T. S., "Wideband measurements of angle and delay dispersion for outdoor and indoor peer-to-peer radio channels at 1920 MHz," *IEEE Transactions on Antennas and Propagation*, vol. 51, pp. 936–944, May 2003.

[13] Durgin, G. D. and Rappaport, T. S., "A basic relationship between multipath angular spread and narrowband fading in wireless channels," *Electronic Letters*, vol. 34, pp. 2431–2432, Dec. 1998.

[14] Durgin, G., *Space-Time Wireless Channels.* Upper Saddle River, NJ: Prentice Hall Inc., 2003.

[15] Gans, M. J., Valenzuela, R. A., Yeh, Y.-S., and Amitay, N., "Antenna pattern deconvolution for precise incident power density pattern measurement," in *Vehicular Technology Conference Proceedings, 2000*, vol. 3, pp. 2532–2535, 2000.

[16] Geng, S., Ranvier, S., Zhao, X., Kivinen, J., and Vainikainen, P., "Multipath propagation characterization of ultra-wide band indoor radio channels," in *2005 IEEE Int. Conf. on Ultra-Wideband*, pp. 11–15, 5-8 Sept 2005.

[17] Ghassemzadeh, S. S., Jana, R., Rice, C. W., Turin, W., and Tarokh, V., "Measurement and modeling of an ultra-wide bandwidth indoor channel," *IEEE Transactions on Communications*, vol. 52, pp. 1786–1796, Oct. 2004.

[18] Gold, R., "Optimal binary sequences for spread spectrum multiplexing," *IEEE Transactions on Information Theory*, vol. 13, pp. 619–621, Oct. 1967.

[19] Golomb, S. W., *Shift Register Sequences.* Laguna Hills, CA: Agean Park Press, revised ed., 1982.

[20] Hashemi, H. and Tholl, D., "Delay spread of indoor radio propagation channels," *IEEE Transactions on Vehicular Technology*, vol. 43, pp. 110–120, Feb. 1994.

[21] Haykin, S., *Communication Systems.* John Wiley & Sons, Inc., 4th ed., 2001.

[22] Honda, S., Ito, M., Seki, H., and Jinbo, Y., "A disk monopole antenna with 1:8 impedance bandwidth and omnidirectional radiation pattern," in *Proceedings of the International Symposium on Antennas and Propagation*, vol. 4, p. 1145, Institute of Electronics, Informatio, and Communication Engineers, 1992.

[23] Karedal, J., Wyne, S., Almers, P., Tufvesson, F., and Molisch, A. F., "UWB channel measurements in an industrial environment," in *Global Telecommunications Conference, 2004*, vol. 6, pp. 3511–3516, 29 Nov - 3 Dec 2004.

[24] Labs, P. R., "Prl faqs: Ecl and pecl: Answers 9-12." Online: http://www.pulseresearchlab.com/faqs/ecl_ques/ecl_Q9-Q12.htm.

[25] Liang, J., Chiau, C. C., Chen, X., and Parini, C. G., "Analysis and design of UWB disc monopole antennas," in *IEE Seminar on UWB Communications Technologies and System Design*, pp. 103–106, July 2004.

[26] Liang, J., Guo, L., Chiau, C. C., and Chen, X., "Time domain characteristics of UWB disc monopole antennas," in *The European Conference on Wireless Technology, 2005*, pp. 289–292, October 2005.

[27] Mini-Circuits, "Ceramic frequency mixer wide band MCA1-60+." Online: http://www.minicircuits.com/pdfs/MCA1-60+.pdf.

[28] Mini-Circuits, "Ceramic low pass filter LFCN-400." Online: http://www.minicircuits.com/pdfs/LFCN-400.pdf.

[29] Mini-Circuits, "Coaxial amplifier ZVE-8G." Online: http://www.minicircuits.com/pdfs/ZVE-8G.pdf.

[30] Mini-Circuits, "Ultra-Reliable High Pass Filter VHP-26." Online: http://www.minicircuits.com/pdfs/VHP-26.pdf.

[31] Mini-Circuits, "Ultra-Reliable Low Pass Filter VLP-54." Online: http://www.minicircuits.com/pdfs/VLP-54.pdf.

[32] Molisch, A. F., "Ultrawideband propagation channels-theory, measurement, and modeling," *IEEE Transactions on Vehicular Technology*, vol. 54, pp. 1528–1545, September 2005.

[33] Newhall, W. G., Saldanha, K., and Rappaport, T. S., "Using RF channel sounding measurements to determine delay spread and path loss," *RF Design*, pp. 82–88, January 1996.

[34] Papoulis, A., *Probability, Random Variables, and Stochastic Processes.* McGraw-Hill, Inc, 1965.

[35] Parsons, J. D., *The Mobile Radio Propagation Channel.* John Wiley & Sons LTD, 2nd ed., 2000.

[36] Rappaport, T. S., "Characterization of UHF multipath radio channels in factory\buildings," *IEEE Transactions on Antennas and Propagation*, vol. 37, pp. 1058–1069, August 1989.

[37] Reed, J. H., ed., *An Introduction to Ultra Wideband Communication Systems.* Upper Saddle River, NJ: Pearson Education, Inc., 2005.

[38] Richards, M., Morris, C., and Hayes, M., "Iterative enhancement of non-coherent radar data," in *IEEE Int. Conf. on Acoustics, Speech, and Signal Processing*, vol. 11, pp. 1929–1932, Apr. 1986.

[39] Schantz, H. G., "A brief history of UWB antennas," in *2003 IEEE Conf. on UWB Systems and Technologies*, pp. 209–213, Nov. 2003.

[40] Semiconductor, O., "Designing with PECL (ECL at +5.0 V)." Application Note AND8090/D, Online: http://www.onsemi.com/pub/Collateral/AN1406-D.PDF, Sept. 1999.

[41] Semiconductor, O., "MC10EP08, MC100EP08 3.3V / 5V Differential 2-Input XOR/XNOR," 2001. Online: http://www.onsemi.com/pub/Collateral/MC10EP08-D.pdf.

[42] Semiconductor, O., "Interfacing with ECLinPS." Application Note AND8066/D, Online: http://www.onsemi.com/pub/Collateral/AND8066-D.PDF, May 2002.

[43] Semiconductor, O., "Termination of ECL logic devices." Application Note AND8020/D, Online: http://www.onsemi.com/pub/Collateral/AND8020-D.PDF, Aug. 2002.

[44] Semiconductor, O., "MC10EP01, MC100EP01 3.3V / 5V ECL 4-Input OR/NOR," 2006. Online: http://www.onsemi.com/pub/Collateral/MC10EP01-D.pdf.

[45] Semiconductor, O., "MC10EP142, MC100EP142 3.3 V / 5 V ECL 9-Bit Shift Register," Nov. 2006. Online: http://www.onsemi.com/pub/Collateral/MC10EP142-D.pdf.

[46] Semiconductor, O., "MC10EP16, MC100EP16 3.3V / 5V ECL Differential Receiver/Driver," Dec. 2006. Online: http://www.onsemi.com/pub/Collateral/MC10EP16-D.pdf.

[47] Shannon, C. E., "Communication in the presence of noise," in *Proceedings of the IRE*, vol. 37, pp. 10–21, 1949.

[48] Siwiak, K. and McKeown, D., *Ultra-Wideband Radio Technology.* John Willey & Sons, Inc., 2004.

[49] Standage, T., *The Victorian Internet.* Walker Publishing Co., 1998.

[50] Still, A., *Communication Through the Ages.* Ferris Printing Company, 1946.

[51] Takeuchi, T. and Tamura, M., "An ultra-wide band channel sounder for mobile communication systems," in *12th IEEE International Symposium on Personal, Indoor and Mobile Radio Communcations, 2001*, vol. 2, pp. E111–E115, 2001.

[52] Turin, G. L., "Communication through noisy, random multipath channels," in *IRE Convention Record, 1956*, pp. 154–166, 1956.